

Compact laser-assisted tools for high-resolution additive manufacturing

THÈSE N° 8704 (2018)

PRÉSENTÉE LE 13 JUILLET 2018

À LA FACULTÉ DES SCIENCES ET TECHNIQUES DE L'INGÉNIEUR
LABORATOIRE DE DISPOSITIFS PHOTONIQUES APPLIQUÉS
PROGRAMME DOCTORAL EN PHOTONIQUE

ÉCOLE POLYTECHNIQUE FÉDÉRALE DE LAUSANNE

POUR L'OBTENTION DU GRADE DE DOCTEUR ÈS SCIENCES

PAR

Paul DELROT

acceptée sur proposition du jury:

Prof. D. Psaltis, président du jury
Prof. C. Moser, directeur de thèse
Prof. W. Husinsky, rapporteur
Dr M. Duocastella, rapporteur
Prof. Y. Bellouard, rapporteur



ÉCOLE POLYTECHNIQUE
FÉDÉRALE DE LAUSANNE

Suisse
2018

Avant donc que d'écrire, apprenez à penser. [...]
Ce que l'on conçoit bien s'énonce clairement,
Et les mots pour le dire arrivent aisément.[...]
Hâtez-vous lentement, et, sans perdre courage,
Vingt fois sur le métier remettez votre ouvrage :
Polissez-le sans cesse et le repolissez ;
Ajoutez quelquefois, et souvent effacez. [...]
— Nicolas Boileau, *L'art poétique*

Acknowledgements

Writing this thesis completes a journey of almost four years.

At the end of this amazing and intense journey, I would like to first thank my thesis advisor, Professor Christophe Moser, for trusting me and giving me the opportunity to work at the Laboratory of Applied Photonics Devices in École Polytechnique Fédérale de Lausanne. I am very grateful for his support and the fantastic atmosphere he built in the lab, which really empowered me to complete this PhD.

I want to deeply thank my friend and colleague Damien Loterie, for all the fruitful discussions we had and for the time he dedicated to the success of my PhD.

I would like to also thank my other office mates Dino and Manon for bringing so much fun to this PhD. Thanks as well to Timothé, Mathieu, Seb, Jan and Enrico for their friendship and incitations to both practice more sport and drink responsibly... Thanks also to the students I had the opportunity to supervise: Sylvain, Loïc and Nathanaël. I want to specifically thank Sabrina for all the organization and administrative support, she made this PhD very smooth in terms of paperwork. Thanks as well to all the past and present colleagues I've had in the lab, I had a great time working and spending time with everyone: Miguel, Gaël, David, Frédéric, Volker, Zahra, Andreas, Laurent, Eric, Mickaël, Maya, Sunan, Ronald, Babak and Chiara.

I also take the opportunity to thank Professor Demetri Psaltis for his valuable inputs over these years and for being the president of my thesis jury.

I am very grateful to the other members of my thesis committee, Prof. Bellouard, Prof. Husinsky and Dr. Duocastella for dedicating time to review and improve this manuscript. Thanks also to Chris, Damien and Serge for proofreading my thesis.

Finally, I want to thank everyone who has supported me during these years.

Lausanne, 17 mai 2018

Paul

Résumé

La micro-fabrication additive ouvre de nouvelles perspectives pour la recherche biomédicale. Les nouveaux outils offerts par la micro-impression 3D permettent en effet de créer des microstructures fonctionnelles ou encore d'étudier les interactions à l'échelle de la cellule. Parmi les différents outils d'impression, les lasers présentent un large panel d'utilisation pour la micro-fabrication, que ce soit pour produire des gouttes ou jets de liquides ou induire la solidification de photopolymères pour former des microstructures.

Dans cette thèse, le potentiel d'utilisation d'actionneurs lasers pour l'impression 3D suspendue est étudié. Dans les systèmes actuels d'impression 3D suspendue, des microstructures molles sont construites en déposant des filaments d'encre par micro-extrusion dans un support à base de gel. La micro-extrusion produisant des filaments d'encre en continu, elle ne permet pas de reproduire de manière fine la micro-architecture tri-dimensionnelle des tissus. Ainsi, pour améliorer la résolution des impressions 3D suspendues, le transfert de liquide par impulsion laser, une technique de production de jets haute-vitesses, est utilisée pour injecter des liquides à des profondeurs arbitraires dans un gel support. Le contrôle de la profondeur d'injection de gouttes offre un degré de liberté supplémentaire à la technique de transfert de liquide par impulsion laser, ce qui transforme cette méthode conventionnelle d'impression 2D en une technique directe d'impression 3D.

Dans la seconde partie de cette thèse, le potentiel d'utilisation d'actionneurs lasers pour le développement d'outils d'impression 3D à haute résolution est aussi étudié. La fabrication de pièces comprenant des fonctions avancées, avec de multiples matériaux imprimés à différents niveaux de résolution, reste difficile. Les techniques existantes de micro-fabrication nécessitent en effet l'utilisation d'appareils encombrants et complexes, ce qui restreint l'utilisation de ces différents outils sur une même pièce. Ainsi, pour permettre la fabrication additive de pièces suivant plusieurs procédés, des outils miniatures de production de gouttes et de stéréolithographie directe ont été développés dans cette thèse avec des actionneurs lasers.

Pour la conception du premier outil, un phénomène de convergence hydrodynamique induit par laser a été étudié pour permettre la génération de micro-gouttes visqueuses à travers un micro-capillaire de 300 μm de diamètre. Ce système ouvre la voie au développement d'un appareil de production de gouttes à la demande offrant une plus large gamme d'encres imprimables que les imprimantes jet d'encre conventionnelles.

Résumé

Le second outil miniature est basé sur la photopolymérisation à un photon inhibée par l'oxygène dissous. Ce procédé de photopolymérisation non-linéaire est étudié et implémenté à travers une fibre de 70 μm de diamètre pour faire la démonstration de micro-fabrication 3D à travers un endoscope. Cette sonde aux capacités d'impression 3D offre une alternative compacte et bon marché aux outils conventionnels de stéréolithographie directe qui reposent sur l'absorption à deux-photons, un phénomène d'absorption non-linéaire nécessitant l'utilisation de lasers femtosecondes.

De tels outils miniatures de fabrication additive ouvrent de nouveaux horizons pour la fabrication de microstructures dans des endroits difficiles d'accès, tels que pour des applications *in vivo*.

Mots-clés: fabrication additive, photopolymérisation, microfabrication 3D, fibre optique, impression par laser, LIFT, impression 3D suspendue, appareils compacts d'impression 3D, impression à jet d'encre.

Abstract

Micro-additive manufacturing has become an enabling technology in biomedical research as it allows for instance creating functional microstructures or studying cellular interactions at the microscale. Among the various manufacturing techniques laser-actuation offers a versatile control means for microprinting applications since it both enables jetting liquids and curing photoresists to form three-dimensional microstructures.

In the first part of this thesis, the potential of laser-actuation for embedded three-dimensional printing was studied. In conventional embedded three-dimensional printing, soft microstructures are built by directly depositing ink filaments with a microextruder into a gel-like support material. As microextruders produce continuous ink filaments, they do not allow optimally mimicking the complex three-dimensional micro-architectures of tissues. Thus, to improve the resolution of three-dimensional embedded printing, laser-induced forward transfer, a high-velocity liquid jetting technique, was employed to achieve depth-controlled liquid delivery within a gel-like support substrate. Interestingly, controlling the deposition depth of liquid droplets adds a degree of freedom to laser-induced forward transfer, turning this conventional two-dimensional patterning technique into a direct three-dimensional printing technique.

In the second part of this thesis, the potential of laser-actuation to build a compact laser-assisted toolkit for high-resolution manufacturing was further studied. The fabrication of advanced functional parts with multi-material and multi-resolution features stills remains challenging. Existing microfabrication techniques rely on complex and bulky devices, which prevent processing parts with several manufacturing tools on a single platform due to space constraints. Hence, to enable multiprocess additive manufacturing, miniaturized laser-assisted drop-on-demand and direct writing tools were developed in this thesis.

In the first component of this compact toolkit, a laser-induced flow focusing phenomenon was studied to generate viscous micro-droplets through a 300- μm glass microcapillary, thus paving the way for a compact drop-on-demand device operating on a wider range of printable liquids than standard inkjet printers.

The second component of the miniaturized toolkit is based on oxygen-inhibited single-photon photopolymerization. This non-linear photopolymerization process was investigated and then implemented through a 70- μm multimode fiber to demonstrate three-dimensional

Abstract

microfabrication through an endoscope-like tool. This curing probe provides a compact and affordable alternative to conventional direct laser writing devices, which rely on two-photon absorption, a non-linear absorption phenomenon that entails using femtosecond lasers.

Such a miniature additive manufacturing toolkit could also open up possibilities for the fabrication of microstructures in areas otherwise inaccessible, for instance in *in vivo* applications.

Keywords: additive manufacturing, photopolymerization, three-dimensional microfabrication, fiber optics, laser-induced forward transfer, LIFT, embedded 3D printing, compact 3D printing devices, inkjet printing.

Contents

Acknowledgements	v
Abstract (Français/English)	vii
List of figures	xiii
List of tables	xvi
Introduction	1
1 Introduction	1
1.1 Micro-additive manufacturing techniques	2
1.1.1 Assembly methods for soft three-dimensional microfabrication	2
1.1.2 Ink- and light-based micro-additive manufacturing techniques	3
1.1.3 Discussion	5
1.2 Motivation	7
1.2.1 Compact toolkit for high-resolution additive manufacturing	7
1.2.2 Embedded printing through laser-induced forward transfer	9
2 Dimensionless analysis for optofluidics	11
2.1 Rheology of Newtonian, non-Newtonian liquids and Bingham plastics	11
2.1.1 Viscosity, shear rate and shear force	11
2.1.2 Flow curves	13
2.2 Dimensionless analysis of inkjet printing	16
2.2.1 Dimensionless numbers	16
2.2.2 Printability map of inkjet printing	17
2.3 Dimensionless analysis of laser-induced forward transfer	18
2.3.1 Dimensionless numbers	18
2.3.2 Printability map of laser-induced forward transfer	20
2.4 Conclusion	22
3 Laser-induced direct three-dimensional liquid delivery	23
3.1 Introduction and motivation	23
3.1.1 Microextrusion embedded printing	23
3.1.2 Drop-on-demand embedded printing	24

Contents

3.2	Generation of high-velocity jets by laser-induced forward transfer	25
3.2.1	Methods	26
3.2.2	Control of the jetting velocity with the laser fluence	28
3.3	Depth-controlled injection for direct three-dimensional liquid delivery	30
3.3.1	Depth-controlled injection	30
3.3.2	Morphology of injection	31
3.3.3	Application to particle delivery	32
3.3.4	Dimensionless analysis for the generation of high-velocity single-droplet	34
3.4	Conclusion	37
4	Compact laser-assisted inkjet printing of highly viscous fluids	39
4.1	Introduction	39
4.2	Generation of viscous monodisperse droplets by laser-induced flow-focusing	41
4.2.1	Experimental setup	41
4.2.2	Dynamics of flow-focused jetting	43
4.2.3	Jetting regimes for Newtonian and non-Newtonian inks	44
4.3	Printing performances	46
4.3.1	Range of printable liquids	46
4.3.2	Printing resolution	47
4.4	Biocompatibility of the laser-actuation	49
4.5	Compact fiber-based drop-on-demand system	50
4.6	Conclusion	51
5	Single-photon non-linear photopolymerization	53
5.1	Introduction and motivation	53
5.1.1	Free-radical chain photopolymerization	53
5.1.2	Optimal three-dimensional microfabrication	55
5.1.3	Two-photon photopolymerization	57
5.1.4	Alternative non-linear photopolymerization processes	58
5.2	Photopolymerization kinetics	60
5.2.1	Calibration methods	60
5.2.2	Single-photon non-linear photopolymerization	62
5.2.3	Time-resolved measurement of photopolymerization kinetics	63
5.3	Conclusion	66
6	Three-dimensional microfabrication through a multimode fiber	67
6.1	Digital light scanning through a multimode fiber	67
6.1.1	Image transmission through multimode fibers	67
6.1.2	Calibration of the multimode fiber for the distal generation of focused laser spots	68
6.1.3	Experimental setup for single-photon microfabrication	70
6.2	Curing method for optimal single-photon three-dimensional fabrication	71
6.2.1	Generation of high-contrast laser focal spots through the multimode fiber	71

6.2.2	Sampling parameters	71
6.2.3	Optimal curing strategy	72
6.3	Limitations of the current device	74
6.3.1	Hardware limitations	74
6.3.2	Lateral printing resolution	74
6.3.3	Axial printing resolution	75
6.4	Exposure correction algorithms	76
6.4.1	Proximity exposure correction	76
6.4.2	Volumetric phase optimization	78
6.5	Conclusion	80
7	Conclusion	83
7.1	Summary of results	83
7.1.1	Laser-induced direct three-dimensional liquid delivery	83
7.1.2	Compact toolkit for high-resolution additive manufacturing	83
7.2	Future work	84
7.2.1	Laser-induced direct three-dimensional liquid delivery	84
7.2.2	Compact toolkit for high-resolution additive manufacturing	85
7.3	End word	85
A	Modelization of oxygen-inhibited single-photon photopolymerization	87
A.1	Photopolymerization model	87
A.1.1	Initiation and propagation	87
A.1.2	Termination	88
A.1.3	Oxygen inhibition	88
A.2	Photo-initiation	89
A.2.1	Initiating gaussian beam	89
A.2.2	Light absorption	91
A.3	Photopolymerization rate equations	93
A.3.1	Single-photon photopolymerization without oxygen inhibition	93
A.3.2	Oxygen-inhibited single-photon photopolymerization	94
A.3.3	Rate constants	94
A.3.4	Initial conditions	95
A.4	Simulation results	95
A.4.1	Case study	95
A.4.2	Results	97
	Bibliography	113
	Curriculum Vitae	115

List of Figures

1.1	Assembly strategies for additive manufacturing	2
1.2	Ink-based micro-additive manufacturing techniques	4
1.3	Light-based micro-additive manufacturing techniques	5
1.4	Resolution, throughput and range of printable materials of micro-additive manufacturing techniques	6
1.5	Scale of our compact toolkit for micro-additive manufacturing	7
1.6	Compact toolkit for micro-additive manufacturing	8
1.7	Nozzle and laser-based embedded printing	10
2.1	Shear flow	12
2.2	Ideal flow curves of Newtonian, non-Newtonian liquids and Bingham plastics .	15
2.3	Parameters for droplet generation through a nozzle	16
2.4	Printability map for conventional inkjet printers	18
2.5	Parameters for droplet generation via laser-induced forward transfer	20
2.6	Jetting map for laser-induced forward transfer	21
3.1	Direct three-dimensional embedded printing	25
3.2	Concept and experimental setup for direct three-dimensional liquid delivery by laser-induced forward transfer	27
3.3	Jet velocity as a function of the laser fluence	29
3.4	Control of the injection depth by the jetting velocity	31
3.5	Injection efficiency for the plain ink	32
3.6	Injection performances with a particle-seeded ink	33
3.7	Statistics of injection of cell-like particles	34
3.8	Dimensionless analysis of the laser-induced jetting process	36
4.1	Principle and performances of ink delivery systems	40
4.2	Experimental setup for laser-induced drop-on-demand generation	42
4.3	Time-resolved jet dynamics	43
4.4	Jetting regimes of Newtonian and non-Newtonian inks	45
4.5	Printability map	47
4.6	Printing resolution	48
4.7	Immunoassay for assessing the biocompatibility of the laser-actuation	49
4.8	Envisioned fiber-based compact drop-on-demand device	50

List of Figures

5.1	Polymer gelation	55
5.2	(a) Micro-stereolithography and (b) direct laser writing	55
5.3	Cumulative curing when scanning two lines deep into a photoresist with a linear photopolymerization process.	56
5.4	Reactive pathways for polymerization photo-initiation, photo-inhibition and oxygen inhibition.	57
5.5	Simulation of the effect of oxygen inhibition on the photopolymerization extent of a voxel produced 50- μm deep into our photoresist	59
5.6	Experimental procedure for the measurement of the photopolymerization non-linearity.	61
5.7	Experimental determination of the non-linearity of our single-photon photopolymerization process	62
5.8	Scattering detection of the photopolymerization onset	64
5.9	Holographic detection of the photopolymerization onset	66
6.1	Image transmission through a multimode fiber	68
6.2	Experimental setup for 3D microfabrication through a multimode fiber	69
6.3	Experimental setup for single-photon 3D microfabrication through a multimode fiber	70
6.4	Curing method and printing results	72
6.5	Experimental printing range for three-dimensional microfabrication	73
6.6	Lateral printing resolution	75
6.7	Axial printing resolution	76
6.8	Proximity exposure correction algorithm	77
6.9	Proximity exposure correction algorithm applied to the microtube model	78
6.10	Multi-plane Gerchberg-Saxton algorithm	79
6.11	Volumetric printing through phase optimization	80
A.1	Description of the orientation of simulation	89
A.2	Simulations of absorbed light density	93
A.3	Simulation settings	96
A.4	Non-linear inhibition of polymer growth	97
A.5	Comparison of simulation results with and without oxygen inhibition for an optical power $P_{fiber} = 100 \text{ nW}$	98
A.6	Comparison of simulation results with and without oxygen inhibition for an optical power $P_{fiber} = 200 \text{ nW}$	99
A.7	Comparison of simulation results with and without oxygen inhibition for an optical power $P_{fiber} = 400 \text{ nW}$	100

List of Tables

3.1	Parameters for the dimensionless analysis of the laser-induced jetting regimes	36
A.1	Rate constants for simulations of acrylate photopolymerization	95

1 Introduction

Additive manufacturing, also commonly called 3D printing, consists in designing a three-dimensional digital model, and then directly making the physical three-dimensional part by joining layers of material [1].

Though the development of modern additive manufacturing techniques started in the early 1980s [2–4], only recent technological improvements made this technology suitable for the fabrication of advanced and functional parts [5], either for research purposes or industrial end-part production [6]. Innovative and creative applications that would otherwise not be possible with other present technologies, are developed at an increasing rate with additive manufacturing, which makes it a true enabling technology.

Nowadays, additive manufacturing allows designing complex three-dimensional parts with a wide range of materials from the metric size to the micro- and nano-meter scale.

In this thesis, I focus on microscale printing and investigate alternative laser-based microfabrication techniques that address the integration, affordability and throughput limitations of current printing methods. With this aim in mind, I first use laser-induced forward transfer as an alternative to micro-extrusion printers for direct three-dimensional liquid delivery into a soft substrate (chapter 3). I then study how to integrate several manufacturing techniques on a single platform by developing a compact microprinting toolkit (chapters 4 to 6). In the first component of this toolkit, I use laser-induced flow-focusing in a glass micro-capillary to generate micro-droplets, thus creating a laser-assisted drop-on-demand device (chapter 4). The second component of this toolkit, a compact curing probe, exploits a non-linear photopolymerization phenomenon (chapter 5) to build three-dimensional microstructures through an ultra-thin multimode fiber (chapter 6).

This introductory chapter reviews the existing micro-additive manufacturing techniques relevant to this thesis, and presents the current challenges of microfabrication to motivate my work on compact laser-assisted tools for high-resolution additive manufacturing.

1.1 Micro-additive manufacturing techniques

Three-dimensional soft microstructures are typically built using light- or ink-based techniques by either layer-by-layer patterning (*bottom-up* approach), material seeding of a scaffold (*top-down* approach) or direct three-dimensional writing into a soft substrate (*embedded printing* approach).

1.1.1 Assembly methods for soft three-dimensional microfabrication

Most micro-additive manufacturing techniques currently follow a bottom-up printing approach [7], in which a three-dimensional model is decomposed into slices and the associated part is built by sequentially joining layers or voxels of material (see Fig. 1.1(a)). Using this printing strategy, the amount and type of material transferred to the part is precisely controlled, thus allowing to form spatial patterns and three-dimensional micro-architectures. The achieved micro-organization brings in turn functional features to the assembly, for instance to promote cell differentiation into skin layers [8,9] or to manipulate light [10–12].

In a scaffold-based approach (or top-down printing), the material is not patterned but rather seeded in a support scaffold (see Fig. 1.1(b)). This approach requires prior fabrication of the support scaffold using a bottom-up approach. Top-down printing is mainly used for biological applications such as skin, cartilage or bone growth [7, 13]. Though this printing strategy allows for instance regenerating thin tissues and studying cell interactions with different microstructures [14], the lack of control over the diffusion of the seeded material into the scaffold prevents its use for printing organised and functional parts [7].

Finally, in the embedded printing approach, an ink is directly written into a soft support material (see Fig. 1.1(c)). This support material has Bingham plastic properties, it flows under the high shear stress induced by the motion of the nozzle printer but acts as a solid under low shear stress, and thus can support the deposited ink (see section 2.1.2 for further details). This printing strategy offers a large design freedom [15–18] and is mostly used to print soft matter that would collapse without a support material [19].

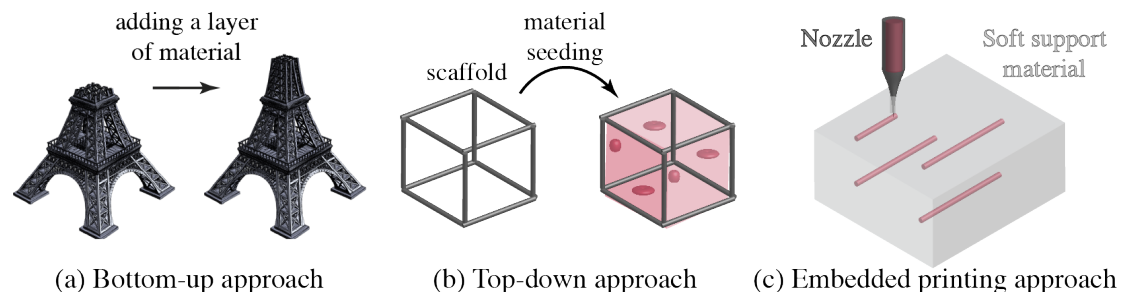


Figure 1.1 – Assembly strategies for additive manufacturing

In this thesis, I use bottom-up and embedded printing strategies combined with direct laser writing, inkjet printing and laser-induced forward transfer, which are introduced in the next section.

1.1.2 Ink- and light-based micro-additive manufacturing techniques

The numerous fabrication methods in additive manufacturing can roughly be classified as ink- and light-based techniques. In this section, we review the most used methods for microscale and mesoscale additive manufacturing.

Ink-based techniques

Fused deposition modeling is one of the most affordable and therefore most widespread printing techniques [5]. In this process, a solid thermoplastic filament is simultaneously extruded and melted to flow through a nozzle (see Fig. 1.2(a)). Three-dimensional solid parts are then produced layer-by-layer through raster-scanning of the fused filament that eventually cools down under its glass-transition temperature and thus solidifies [5, 19]. Because of the melting step, this printing technique cannot be directly used with biological samples and is rather employed to build scaffolds for cell seeding [20] following the top-down approach (see section 1.1.1).

The unheated counterpart of fused deposition modeling is microextrusion printing. In this technique a viscoelastic ink is made to flow through a nozzle by a pressure exceeding its yield stress (see Fig. 1.2(b)). The nozzle or build platform are then moved in a raster-scanned manner to form patterned layers. Once the shear-thinning ink is extruded, it becomes more viscous again and can withstand the subsequent printed layers. This technique is extensively exploited for bioprinting applications because of its good biocompatibility, > 40%, and its wide range of printable inks, with viscosities ranging from 30 mPa s to $> 6 \cdot 10^7$ mPa s [8]. To prevent the collapse of the printed structure, its stiffness can be further increased by using a sacrificial support material [19] or an additional curing step via thermal control [21, 22], ionic gelation [23] or photopolymerization [22].

As described in section 1.1.1, a recent implementation of micro-extrusion, embedded printing, allows printing soft matter without an additional curing step [15–17]. In this technique, a granular matrix material supports the extruded soft ink while it allows for nozzle motion (see section 2.1.2 for further details on the support material's rheology). Layers are then sequentially patterned through raster-scanning the nozzle (see Fig. 1.2(c)), the resulting three-dimensional part can then also be released by liquifying the support material [17].

Inkjet printing is a combination of ink- and light-based methods. As in standard desktop printers, a thermal or piezo print head generates droplets that are generally photopolymerized right after impact (see Fig. 1.2(d)) since the low viscosity of the ink would prevent direct build-up in three dimensions [24]. Three-dimensional inkjet printing benefits from the technological

maturity of print heads [25], which can be combined in large two-dimensional arrays to greatly increase throughput when forming the sequence of patterned layers. The high cell viability, > 85%, demonstrated with the inkjet method, as well as its affordability, make it suitable for bioprinting applications [8].

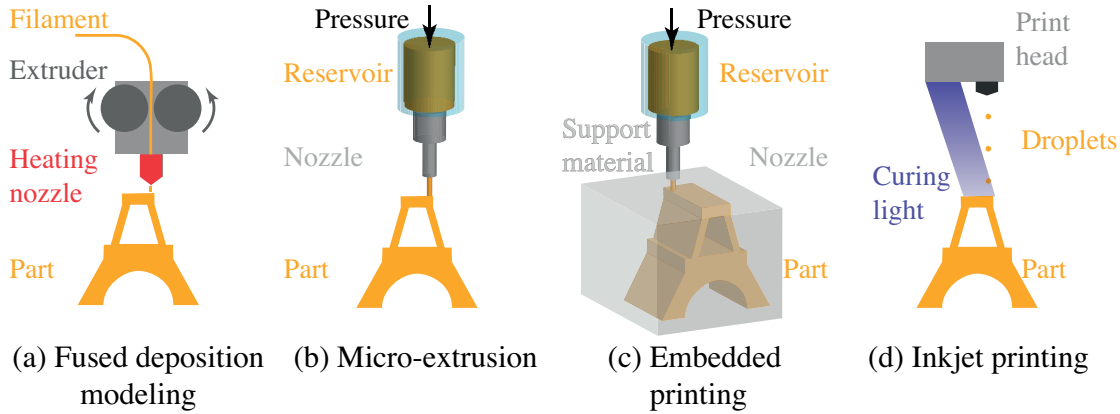


Figure 1.2 – Ink-based micro-additive manufacturing techniques. Fig. 1.2(a) is adapted from [19]

Light-based techniques

Laser-induced forward transfer is a specific laser-actuated implementation of the inkjet printing method. As shown in Fig. 1.3(a), upon the absorption of a nanosecond or picosecond laser pulse, a highly focused jet is formed and picoliter volumes are transferred from a donor slide, coated with a micrometric layer of ink, towards the printed part [26]. As in micro-extrusion and inkjet printing, the ink's low viscosity might prevent the direct three-dimensional build-up of the part, thus the transferred ink can be cured using ionic gelation [27] or photocrosslinking [8]. Owing to the absence of nozzle, lower shear stresses are applied to the ink, thus resulting in > 95% cell viability, which makes laser-induced forward transfer a technique of choice for bioprinting [9, 28].

Selective laser sintering operates by melting and fusing together patterned layers of a polymer powder with a high-power raster-scanned laser beam (see Fig. 1.3(b)). Once a layer is sintered, the part is lowered down and a roll applies a fresh thin powder layer. The part is thus formed layer-by-layer. The un-sintered powder acts as a support material for the part being printed and can be subsequently recycled. This printing technique is limited in resolution by the powder layer $\sim 100\ \mu\text{m}$ (see section 1.1.3) and therefore prints parts in the mesoscale range.

Stereolithography is the oldest and one of the most mature additive manufacturing techniques [4, 19]. In this printing technique, a three-dimensional part is fabricated by selectively photopolymerizing a liquid resin. Recent technological developments enabled the fast and continuous production of entire layers [29]. In this particular implementation of stereolithogra-

phy, called continuous liquid interface production, a two-dimensional light pattern is imaged in a vat of photopolymer to cure a layer (see Fig. 1.3(c)). A thin volume of resin remains liquid at the bottom of the vat as polymerization is oxygen-inhibited at the vat interface (see chapter 5 for further details on the inhibition phenomenon). In this way, the part can be produced by continuously lifting the pedestal, which also refills by gravity the cured volume. The printing speed is then ultimately limited by the resin viscosity [30].

In direct laser writing, as opposed to continuous liquid interface production, a layer of material is built through pointwise scanning and curing of a voxel (see Fig. 1.3(d)). Direct laser writing is induced by highly-focused laser pulses that triggers multiphoton absorption. This non-linear absorption phenomenon only takes place in regions of highest intensities, which allows to confine photopolymerization to the focal volume. This offers two main advantages: an unparalleled printing resolution (see section 1.1.3) and the ability to write structures deep into a volume of photoresist without any perturbing motion of the build volume. However, this technique requires complex and expensive femtosecond laser sources.

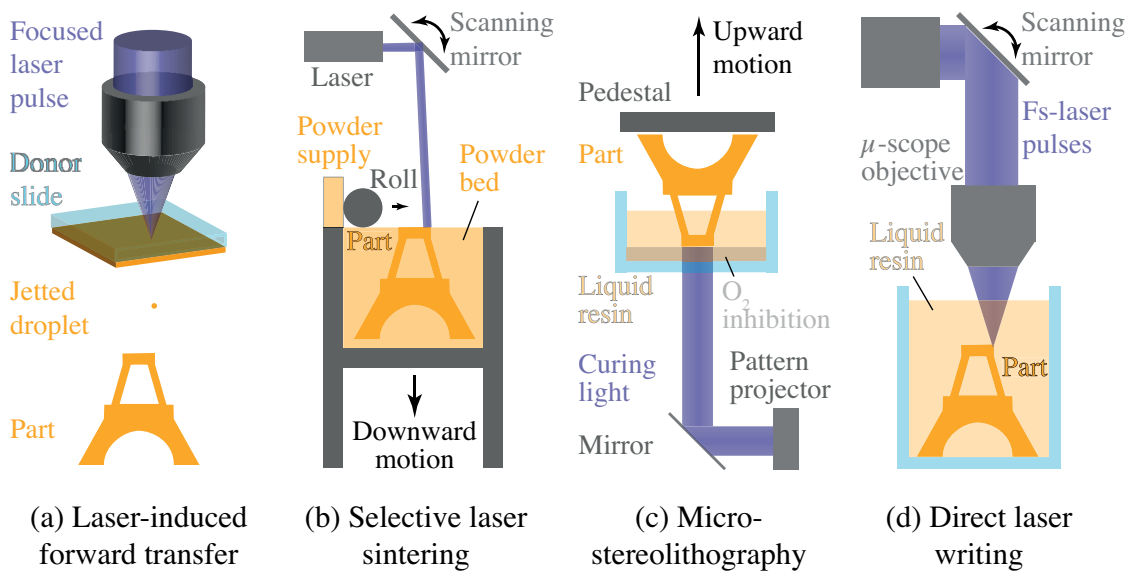


Figure 1.3 – Light-based micro-additive manufacturing techniques. Fig. 1.3(b)-(c) are adapted from [19]

1.1.3 Discussion

In general, light-based techniques are less affordable than ink-based ones because of the cost of the laser sources [19].

Summing up the printing performances of micro-additive manufacturing techniques in a resolution, throughput and material parametric space (see Fig. 1.4), we observe in addition that a larger range of printable materials can be formulated for ink-based techniques than the

photoresists available for light-based techniques, which are limited to plastics, ceramics and hydrogels. However, this larger range of printability comes to the cost of thorough optimization of the inks' rheological properties so that they can flow through the nozzle of micro-extruders and inkjet print heads. Inks with inappropriate rheology often result in nozzle-clogging and unreliable printing [8, 31]. Being a nozzleless technique, laser-induced forward transfer allows overcoming this limitation.

The ink rheology is also critical to achieve an optimal printing resolution with ink-based techniques. The resolution of ink-based printers is determined by the minimal quantity of ink they can deliver. Unsuitable rheological properties might result in the generation of satellite droplets or filaments that will degrade the printing resolution. Besides this requirement for clean printing, the resolution of ink-based techniques is defined by their nozzle size since the droplets and filaments roughly scales with the orifice through which they were produced [19, 32]. On the other hand, the resolution of light-based techniques is defined by how tight a light beam can be focused, which can be as small as a cubic volume defined by the wavelength $\sim \lambda^3$ [33], thus much smaller than the size of state-of-the-art nozzles. Hence, direct laser writing allows achieving the finest feature resolution as shown in Fig. 1.4. In the same way, being a nozzleless technique, laser-induced forward transfer can achieve a finer resolution than most ink-based techniques that print through nozzles.

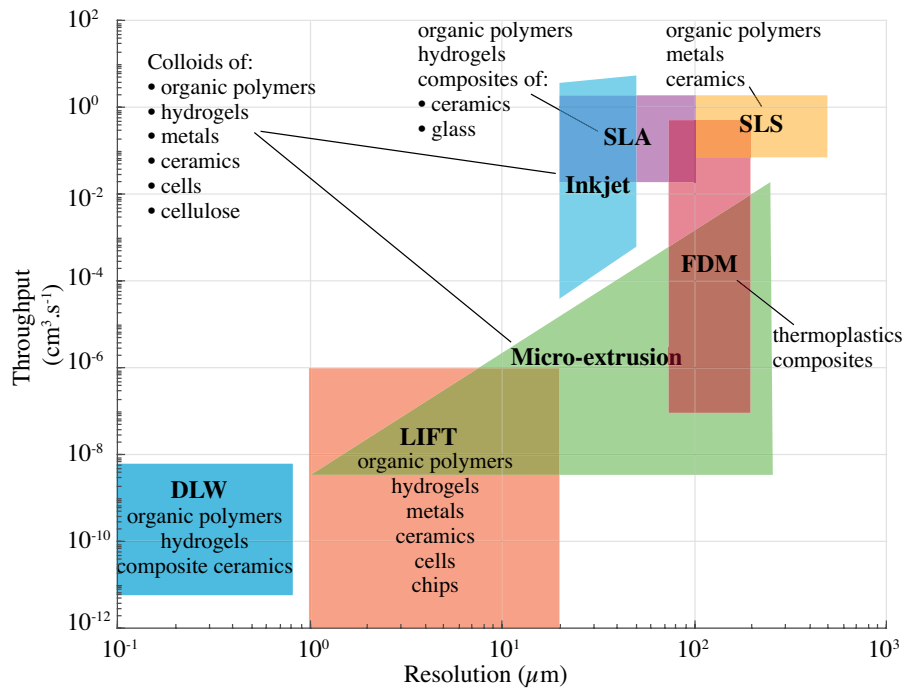


Figure 1.4 – Resolution, throughput and range of printable materials of some micro-additive manufacturing techniques. **DLW**: direct laser writing, **LIFT**: laser-induced forward transfer, **SLA**: stereolithography, **FDM**: fused deposition modeling, **SLS**: selective laser sintering. This diagram is a rough approximation based on the following references [5, 8, 9, 19, 20, 24–26, 29, 33, 34, 34–42]

However, there is an inherent trade-off between resolution and throughput as observed in Fig. 1.4. Techniques with a finer resolution will produce less volume of material whereas coarser techniques will have a higher volumetric throughput. To improve throughput, nozzles or light beams can be parallelized, as currently investigated for laser-induced forward transfer [36], and already implemented in inkjet printers, micro-extruders and continuous liquid interface production.

A broad spectrum of resolution, throughput and materials is already covered by existing additive manufacturing techniques. However, creating parts with enhanced functionalities by multi-resolution and multi-material printing still remains challenging.

1.2 Motivation

1.2.1 Compact toolkit for high-resolution additive manufacturing

Extensive research efforts have been dedicated to the improvement of the resolution and printing speed of micro-additive manufacturing techniques. Moreover, research groups have been focused on extending the range of printable materials with each manufacturing method in order to fabricate functional multi-material parts with a single printing device.

Alternatively, achieving multi-material printing could also be achieved by combining several printing techniques on a single platform. This would also allow building multi-resolution parts with an optimized throughput. Fine details would be created with a high-resolution but low-throughput technique while the bulk structure could be made with a coarse resolution but high-throughput technique, as illustrated in Fig. 1.4. Multiprocess manufacturing was recently attempted using a six-axis robotic arm to convey parts from one processing unit to another [43].

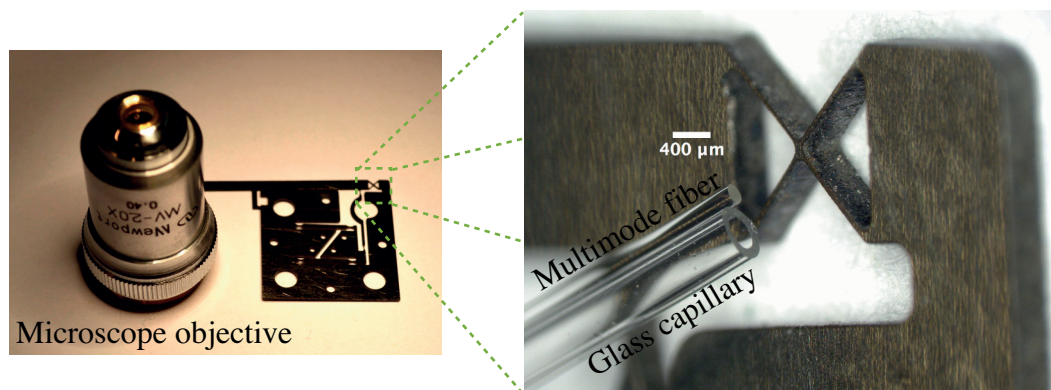


Figure 1.5 – Scale of our compact toolkit for micro-additive manufacturing compared to a standard microscope objective

Such an approach is insufficient to integrate multiple processes on a single platform since present additive manufacturing devices are too large to all be accessible by a robotic arm.

Thus, the integration of multiple printing techniques for multi-material and multi-resolution production also requires miniaturizing each manufacturing device.

With this aim in mind, I propose to develop a compact laser-actuated toolkit for high-resolution additive manufacturing. Laser-actuation has both the potential for high-resolution patterning (see Fig. 1.4) and to be used in compact devices. Actually, light can be guided and focused through ultra-thin multimode fibers [44,45], which, in comparison to standard focusing optics, are several orders of magnitude more compact as shown in Fig. 1.5.

The first component of the toolkit is a laser-actuated drop-on-demand device that could deliver *in situ* precise quantities of liquid (see Fig. 1.6). This device is based on previous works on high-velocity jets that were laser-induced in a glass micro-capillary [46]. In this work, the curvature of the meniscus created by the wetting angle of the ink on glass was exploited to flow-focus the ink with a laser-induced shockwave. In chapter 4 of this thesis, I investigate the potential of this technique to reproducibly generate flow-focused droplets of a wide range of viscous inks. Fig. 1.6 shows the envisioned compact laser-actuation of the liquid with a laser pulse focused through a multimode fiber thanks to a phase control system.

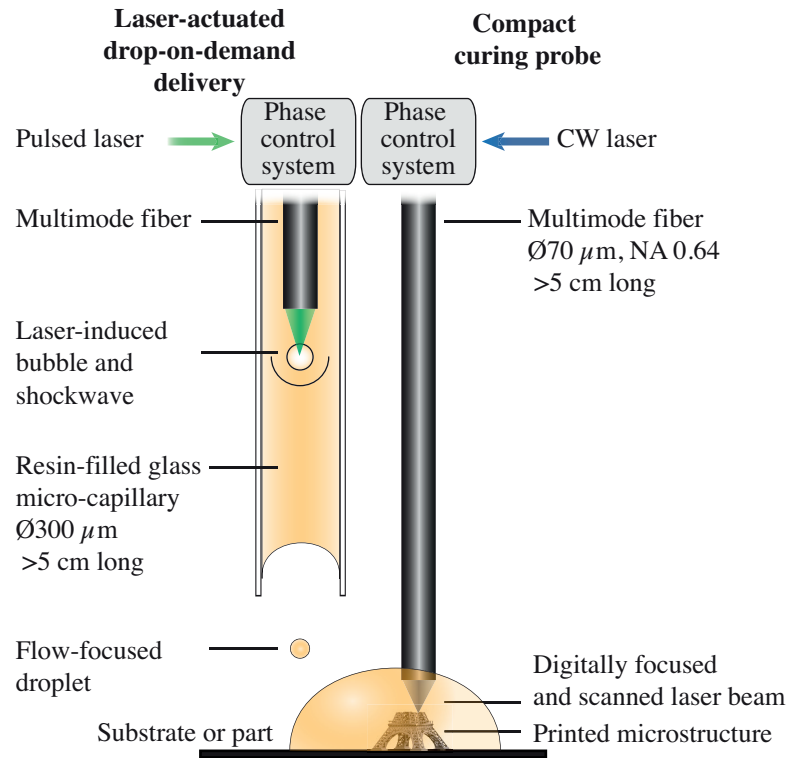


Figure 1.6 – Designed compact toolkit for micro-additive manufacturing

The second component of the toolkit is a compact curing probe. This probe is built around an ultra-thin multimode fiber through which laser light is digitally scanned with a phase control system to photopolymerize three-dimensional microstructures (see Fig. 1.6). To avoid the use of complex and expensive femtosecond lasers, I propose to exploit oxygen-inhibition of

photopolymerization (chapter 5) to selectively cure three-dimensional microstructures with an affordable continuous-wave laser light through the multimode fiber (chapter 6).

In an ideal printing configuration, the two compact devices would be placed alongside, so that the curing probe selectively cures the jetted photoresist (see Fig. 1.6). This compact system could also potentially be employed to fabricate microstructures in areas otherwise inaccessible, for instance in *in vivo* applications.

1.2.2 Embedded printing through laser-induced forward transfer

In this thesis, I also investigate the potential of laser-induced forward transfer to improve the throughput and resolution of the embedded printing technique, which have only been implemented with micro-extrusion nozzles [15–18].

With this current implementation, the micro-extrusion nozzle is inserted and moved into the support matrix material (see Fig. 1.7(a)) to directly deposit continuous ink filaments, which allows fabricating bulk structures and closed shells.

However, reproducing the complex micro-architecture of cells and extracellular components that can be found in living tissues requires delivering picoliter ink doses with a resolution close to the size of a cell ($<20\mu\text{m}$) [24]. Since continuous microextrusion printers do not fulfill these requirements, I alternatively suggest to use drop-on-demand techniques for direct three-dimensional pinpoint delivery of picoliter volumes into the support material.

To this end, I propose to control the deposition depth of the ink by varying its jetting velocity. The support matrix material has Bingham plastic properties, it behaves as a solid below its yield stress and flows like a liquid above this critical stress (see chapter 2 for further details). Thus, we expect that above a threshold velocity the ink will puncture the soft material and will then be gradually slowed down [47].

Though inkjet printing has a micrometric printing resolution and can be parallelized for high-throughput applications, it can only jet liquids over a limited range of velocities ($1\text{--}30\text{ m s}^{-1}$) [8, 25].

On the other hand, laser-induced forward transfer allows jetting materials over a wide range of velocities [48, 49]. Moreover, this jetting method has a sufficient lateral resolution (see Fig. 1.4) to create three-dimensional ink patterns that mimic the complex micro-architecture of tissues [8, 24]. To our knowledge the axial printing resolution of laser-induced forward transfer in a soft material has never been investigated, in spite of extensive research on its lateral printing resolution and precision [50–52]. Thus, in chapter 3 of this thesis, I study depth-controlled laser-induced injection into a soft material with the aim of providing an alternative to nozzle-based embedded printing (see Fig. 1.7(b)).

Interestingly, three-dimensional microstructures are currently printed with laser-induced

forward transfer in a layer-by-layer process, which includes time-consuming gelation steps between every few layers [51, 53, 54]. Hence, directly controlling the ink deposition over three-dimensions would also greatly improve the overall throughput of this printing technique.

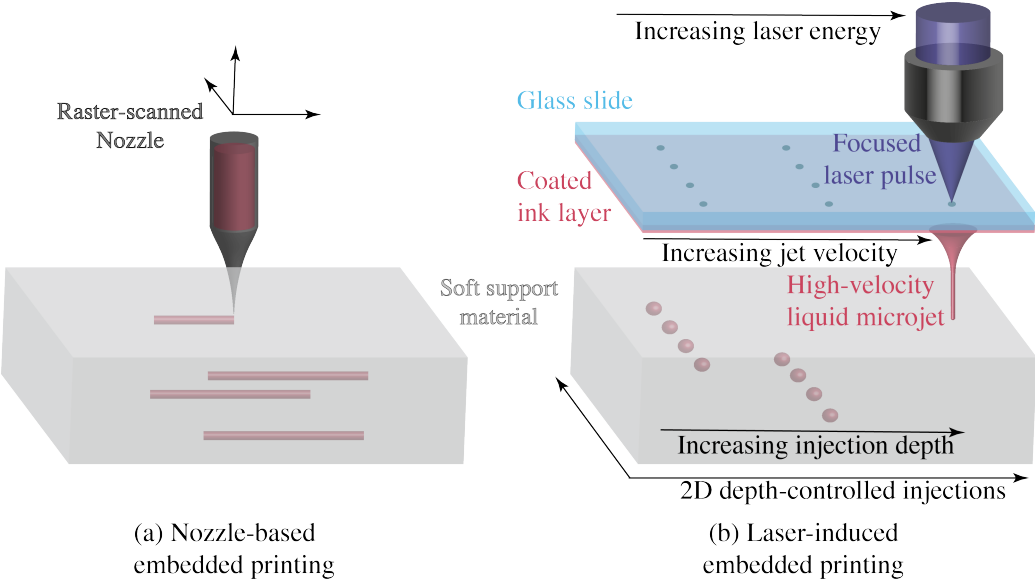


Figure 1.7 – Nozzle and laser-based embedded printing

2 Dimensionless analysis for optofluidics

This chapter introduces a few concepts of fluid mechanics that are essential to the understanding of chapters 3 and 4, in which optofluidics devices are studied.

We first present the rheological properties of the different fluids used in this thesis and then describe the mathematical tools needed to perform a dimensionless analysis of liquid jetting in inkjet printing and laser-induced forward transfer processes. In particular, these tools allow determining the optimal jetting regime for stable single-droplet generation, which produces the best printing quality in ink-based printers.

Some of the material presented in this chapter can be found in the following paper:

- Paul Delrot, Miguel A. Modestino, François Gallaire, Demetri Psaltis, and Christophe Moser. Inkjet Printing of Viscous Monodisperse Microdroplets by Laser-Induced Flow Focusing. *Physical Review Applied*, 6(2):024003-1:024003-8, August 2016.

2.1 Rheology of Newtonian, non-Newtonian liquids and Bingham plastics

To analyse the dynamics of fluids, it is necessary to characterize their viscous and flow properties. This is often done using flow curves, which we introduce in this section to describe the rheology of Newtonian and non-Newtonian liquids as well as Bingham plastics.

2.1.1 Viscosity, shear rate and shear force

Let us assume a liquid standing between two infinite parallel plates separated by a distance h . If we create a steady-state shear flow by keeping one plate still and moving the other at constant velocity v_0 , we observe the appearance of friction forces \vec{F} on the bottom plate and $-\vec{F}$ on the top plate (see Fig. 2.1).

Moreover the liquid is also set into motion and a steady-state gradient of velocity $v(\vec{y})$ is created. Since the velocity is continuous at the borders, the liquid velocity is null at the border of the standing plate and v_0 on the moving plate border. In the case of a Newtonian liquid, as depicted in Fig. 2.1, the steady-state velocity gradient is linear [55] and the velocity field is then:

$$v(\vec{y}) = \frac{y}{h} \vec{v}_0 \quad (2.1)$$

Furthermore, the viscous friction force \vec{F} is proportional to the surface S of the plates. Normalising the force \vec{F} by the surface S , it can be expressed as a function of the viscosity η of the liquid:

$$\frac{\vec{F}}{S} = \frac{\eta}{h} \vec{v}_0 \quad (2.2)$$

Thus, the higher the liquid viscosity η , the larger the friction force \vec{F} opposed to the motion.

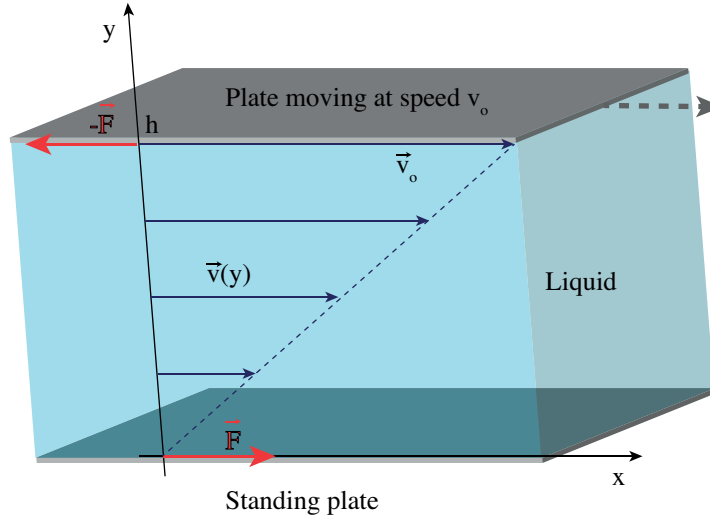


Figure 2.1 – Steady-state shear flow

More generally, the friction force can be written as:

$$\frac{\vec{F}}{S} = \eta \frac{\partial \vec{v}_x}{\partial y} \quad (2.3)$$

The norm of this relationship is more known as the constitutive equation of Newtonian liquids [55]:

$$\tau = \eta \dot{\gamma} \quad (2.4)$$

2.1. Rheology of Newtonian, non-Newtonian liquids and Bingham plastics

where we introduced the *shear stress* τ and the *shear rate* $\dot{\gamma}$:

$$\tau = \frac{\|\vec{F}\|}{S} \quad (2.5)$$

$$\dot{\gamma} = \frac{\partial \|\vec{v}_x\|}{\partial y} \quad (2.6)$$

2.1.2 Flow curves

The simple relationship of Eq. 2.4 characterizes the evolution of shear stress as a function of shear rate and allows describing the flow curves of Newtonian liquids (see Fig. 2.2(a)).

This description can be extended to other types of fluids using the *Herschel-Bulkley* model [19,55]:

$$\tau = \tau_y + k\dot{\gamma}^n \quad (2.7)$$

where τ is the shear stress, τ_y the material yield stress, $\dot{\gamma}$ the shear rate, k the consistency index and n the flow index.

Some dispersed materials, such as granular media, are organized into three-dimensional structures, called coagulated structures, that exhibit some strength. The yield stress τ_y is used to describe the threshold stress that needs to be applied to these materials so that the coagulated structure is destroyed and goes from a solid phase to a liquid phase [55]. In other words, these materials exhibit a solid behavior at low shear stresses and flow like liquids for shear stresses exceeding their yield stress τ_y .

Newtonian liquids

Using the Herschel-Bulkley model, it is possible to describe some ideal rheological behaviors.

Considering a material that is not a coagulated structure, that is to say $\tau_y = 0$, and with a flow index $n = 1$, we derive from Eq. 2.7 the specific case of Newtonian liquids described in Eq. 2.4:

$$\tau = \eta\dot{\gamma} \quad (2.8)$$

where the consistency index k of Eq. 2.7 is here equivalent to the viscosity η of the Newtonian liquid in Eq. 2.4.

Thus, we see on the flow curve of Fig. 2.2(a), that the shear stress τ of ideal Newtonian liquids, like water or glycerol, increases linearly with the applied shear rate $\dot{\gamma}$. We also note that the viscosity η of an ideal Newtonian liquid remains constant with the shear rate $\dot{\gamma}$ (see bottom

graph in Fig. 2.2(a)).

Bingham plastics

On the other hand, some dispersed materials have a non-zero yield stress τ_y and a flow index $n = 1$. Applying these parameters to Eq. 2.7 yields the Bingham equation [55]:

$$\tau = \tau_y + \eta_p \dot{\gamma} \quad (2.9)$$

where the consistency index k of Eq. 2.7 is here termed the plastic viscosity η_p .

Such materials, called ideal Bingham plastics, behave as solids for shear stresses $\tau < \tau_y$. Applying a shear stress $\tau > \tau_y$ destroys their cohesive structure and they start flowing as Newtonian liquids (see flow curve in Fig. 2.2(b)). Like Newtonian liquids, the plastic viscosity η_p of ideal Bingham plastics is independent of the shear rate $\dot{\gamma}$ once they start flowing ($\tau > \tau_y$), as depicted in Fig. 2.2(b).

Blended gelatin [17] is a Bingham plastic and its rheological properties are exploited to provide a support material for soft matter in three-dimensional embedded printing (see section 1.1.1). In the same time, the coagulated structure of blended gelatin, can yield to let a thin nozzle flow into it to deposit an ink (see Fig. 1.2(c)).

Non-Newtonian liquids

Ideal non-Newtonian liquids exhibit a zero yield stress $\tau_y = 0$. They can be shear-thinning, also called pseudo-plastic ($n < 1$) or shear-thickening, also termed as dilatant ($n > 1$). Applying these parameters in the Herschel-Bulkley model (see Eq. 2.7) yields the *Ostwald-De Waele* equation or *power-law* model of liquids [55]:

$$\tau = k \dot{\gamma}^n \quad (2.10)$$

By introducing the concept of apparent viscosity η_a as the ratio of shear stress τ over shear rate $\dot{\gamma}$:

$$\eta_a = \frac{\tau}{\dot{\gamma}} \quad (2.11)$$

we see from Eq. 2.10 and Eq. 2.11 that the flow curve of non-Newtonian liquids can be described by the relationship:

$$\tau = \eta_a(\dot{\gamma}) \cdot \dot{\gamma} \quad (2.12)$$

where the apparent viscosity η_a is:

$$\eta_a(\dot{\gamma}) = k \dot{\gamma}^{n-1} \quad (2.13)$$

2.1. Rheology of Newtonian, non-Newtonian liquids and Bingham plastics

Hence, shear-thinning liquids ($n < 1$), such as some polymer solutions [56], show a decrease in the apparent viscosity η_a with the applied shear rate $\dot{\gamma}$, as shown in the bottom graph of Fig. 2.2(c). Moreover, from Eqs. 2.12-2.13, we derive that their flow curve is characterized by a decreasing slope in the shear stress τ response to an applied shear rate $\dot{\gamma}$ that increases (see flow curve in Fig. 2.2(c)).

Practically, in the case of inkjet printing, such shear-thinning liquids have a non-linear behavior. They tend to be highly viscous for low shear rates, typically at the beginning of the jetting process, and then start flowing with less resistance once set into motion.

Shear-thickening liquids ($n > 1$), as opposed to shear-thinning fluids, exhibit an increase of their apparent viscosity η_a with shear rate (see the bottom graph of Fig. 2.2(d)). In the same way, their flow curve is described by an increasing slope of the shear stress σ curve with the applied shear rate $\dot{\gamma}$ (see Fig. 2.2(d)). In other words, the resistance of these liquids to flow grows with the velocity of the body flowing into it. This behavior can be observed in some suspensions of large particles [57].

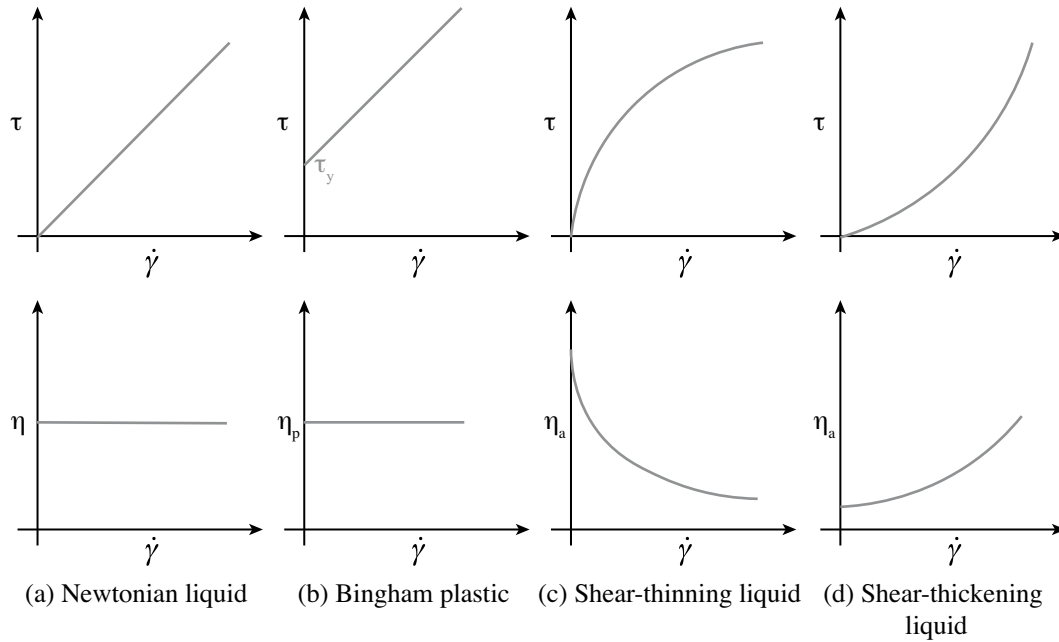


Figure 2.2 – Ideal flow curves of Newtonian, non-Newtonian liquids and Bingham plastics with the evolution of their viscosity as a function of shear rate. These curves are plotted for an intermediate range of shear rate, therefore $\dot{\gamma} > 0$ at the intersection of the x and y axis.

2.2 Dimensionless analysis of inkjet printing

2.2.1 Dimensionless numbers

In conventional thermal and piezoelectric inkjet printers, the drop production mechanism is based on the generation of a pressure pulse that ejects a small amount of incompressible liquid through a nozzle (see Fig. 2.3). If the kinetic energy imparted to the liquid overcomes the surface energy and viscous dissipation of the liquid, one or more droplets are formed.

Though droplet production is a complex process, the two dimensionless Reynolds and Weber numbers are commonly used to characterise inkjet printing [25, 58].

The Reynolds number (Re) represents the ratio of inertial and viscous forces. The Weber number (We) corresponds to the ratio of the kinetic and surface energies. Re and We respectively give an indication on whether a jet can be created, and if it can lead to droplet formation. These numbers are defined as:

$$Re = \frac{\rho R V}{\eta} \quad (2.14)$$

$$We = \frac{\rho R V^2}{\sigma} \quad (2.15)$$

where ρ is the liquid density, R is a characteristic length, V the liquid velocity, η the liquid dynamic viscosity and σ its surface tension (see Fig. 2.3).

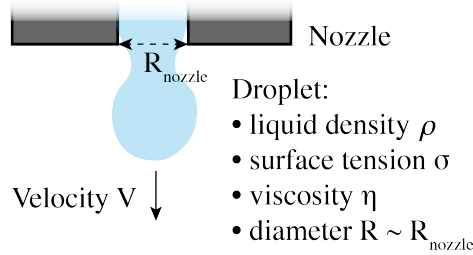


Figure 2.3 – Parameters for droplet generation through a nozzle

Another dimensionless number is often used in inkjet printing to characterise the printability of liquids without the influence of velocity [25]. The so-called Ohnesorge number (Oh) is defined as:

$$Oh = \frac{\sqrt{We}}{Re} \quad (2.16)$$

From Eq.2.14-2.15, Eq.2.16 yields the following expression for Oh :

$$Oh = \frac{\eta}{\sqrt{\sigma \rho R}} \quad (2.17)$$

It is noteworthy that the Ohnesorge number Oh is the ratio of the characteristic time scale t_c and t_μ for capillary and viscous effects to respectively appear:

$$Oh = \frac{t_c}{t_\mu} \quad (2.18)$$

where:

$$t_c = \sqrt{\frac{\rho R^3}{\sigma}} \quad (2.19)$$

and:

$$t_\mu = \frac{\rho R^2}{\eta} \quad (2.20)$$

2.2.2 Printability map of inkjet printing

Using these dimensionless numbers, several criteria were derived from experimental measurements and numerical models to map the regime for stable satellite-free drop generation from a nozzle in the frame of conventional thermal and piezoelectric inkjet printers [25, 58]. Satellite droplets are indeed detrimental to the printing performances since they degrade the printing resolution.

First, setting the characteristic length R in Eq. 2.15 as the drop diameter, the fluid must be imparted a sufficient velocity to overcome surface energy, yielding a criterion on $We > 4$ [58], which is equivalent to the dashed line $Re = 2/Oh$ in Fig. 2.4. In conventional thermal and piezoelectric print heads, this drop diameter R roughly scales with the nozzle diameter [32] (see Fig. 2.3).

Moreover, in order to avoid drop splashing on the substrate, a condition on the drop terminal velocity and on the ink surface tension can be plotted as $OhRe^{5/4} = 50$ in Fig. 2.4 [25, 58]. Finally, a previous study [59] related the jettability of an ink through a nozzle of diameter R with the Ohnesorge number Oh . If the ink is too viscous, $Oh > \sim 1$, viscous effects appear faster than capillary effects (see Eq. 2.18) and droplet breakup cannot occur, whereas if Oh is too low, $Oh < \sim 0.1$, a trail of satellite droplets is likely to be formed.

Based on these criteria, previous works [25, 58, 60] showed that it is possible to build an universal printability map in $Oh-Re$ space. We adapted this diagram in Fig. 2.4 to analyze the performances of our compact drop-on-demand device (see chapter 4), where the printability region for conventional inkjet printers is colored in grey .

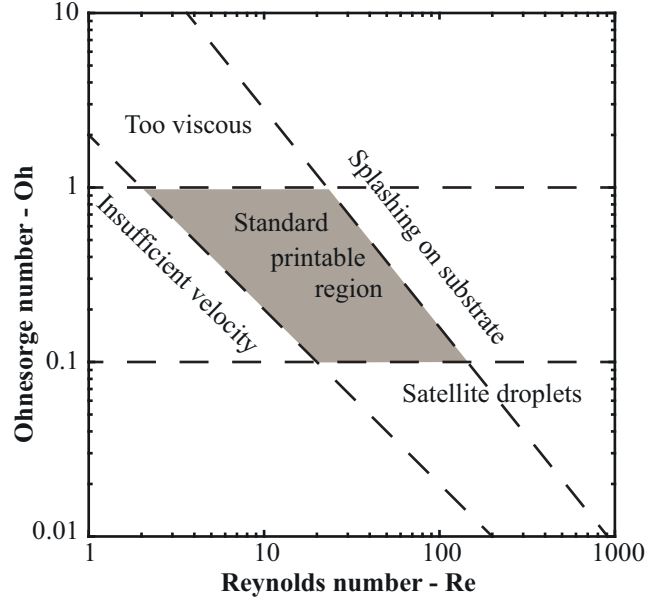


Figure 2.4 – Printability region for conventional thermal and piezoelectric inkjet printers, adapted from [25, 58, 60]

2.3 Dimensionless analysis of laser-induced forward transfer

2.3.1 Dimensionless numbers

A similar dimensionless analysis can be applied to the jetting process of laser-induced forward transfer [61, 62]. In this jetting process, a thin (10-100 μm) layer of ink is coated on a planar transparent slide (see Fig. 2.5). Upon the absorption of a nanosecond laser pulse by a thin light-absorbing layer, a shockwave is produced, which propels the underneath liquid. As in inkjet printing, if the kinetic energy imparted to the column of liquid is sufficient to overcome viscous dissipation and surface energy, a high-aspect ratio jet is subsequently formed and generates one or more liquid droplets.

Modified Ohnesorge number

Recent studies proposed to adapt the Ohnesorge and Deborah numbers to map the jetting regime of viscous inks in laser-induced forward transfer [61, 62]. The modified Ohnesorge number Oh^* , introduced by Turkoz et al. [62], accounts for the geometry of laser-induced forward transfer and the modification of the ink's viscosity $\eta(\dot{\gamma})$ by the high shear rate $\dot{\gamma}$ occurring in the ink layer during jetting (see the shear velocity v_{shear} profile in Fig. 2.5). This modified number reads:

$$Oh^* = \frac{\eta(\dot{\gamma})}{\sqrt{\sigma \rho R}} \quad (2.21)$$

2.3. Dimensionless analysis of laser-induced forward transfer

where $\eta(\dot{\gamma})$ is the shear-rate dependant ink viscosity, σ its surface tension, ρ its density and R the width of the liquid filament (see Fig. 2.5).

The shear velocity v_{shear} induced by the jetting process can be derived from mass balance considerations [62] as:

$$v_{shear} = \frac{v_{jet} R_b}{H} \quad (2.22)$$

where v_{jet} is the mean jet velocity, R_b the focus radius and H the thickness of the ink layer (see Fig. 2.5).

Thus, the resulting shear rate $\dot{\gamma} = \frac{v_{shear}}{H}$ is equal to:

$$\dot{\gamma} = \frac{v_{jet} R_b}{H^2} \quad (2.23)$$

Time-resolved imaging of the laser-induced jetting is required to determine the jet velocity v_{jet} and derive the shear rate $\dot{\gamma}$. Combined to a rheological measurement of the shear-rate dependence of the ink viscosity $\eta(\dot{\gamma})$, this allows building a parametric space of the jetting regimes as a function of the modified Ohnesorge number Oh^* .

Modified Deborah number

The Deborah number De is the ratio of the characteristic internal relaxation time λ_r of the liquid over the time scale of the deformation applied to the liquid t_p :

$$De = \frac{\lambda_r}{t_p} \quad (2.24)$$

where λ_r is an empirical parameter [61] and t_p can be expressed as a function of the capillary time scale t_c of Eq. 2.19 [63]:

$$t_p = \frac{t_c}{\sqrt{0.118}} \quad (2.25)$$

In other words, the Deborah number is here used to predict if the liquid filament does not relax before capillary effects arise to break it up into one or more droplets.

To account for the high-aspect ratio L_{max}/H of the laser-induced liquid filament (see Fig. 2.5), which reduces the relaxation time λ_r , previous studies proposed a modified version of the Deborah number De^* :

$$De^* = \frac{\lambda_r}{t_p} \frac{H}{L_{max}} \quad (2.26)$$

The aspect ratio L_{max}/H can be estimated as [62]:

$$\frac{L_{max}}{H} \sim \frac{v_{jet}}{v_c} \quad (2.27)$$

where v_{jet} is the mean jet velocity (see Fig. 2.5) and v_c is the typical breakup speed:

$$v_c = \sqrt{\frac{\sigma}{\rho H}} \quad (2.28)$$

Finally, the modified Deborah number De^* reads:

$$De^* = \frac{\lambda_r}{t_p} \frac{v_c}{v_{jet}} \quad (2.29)$$

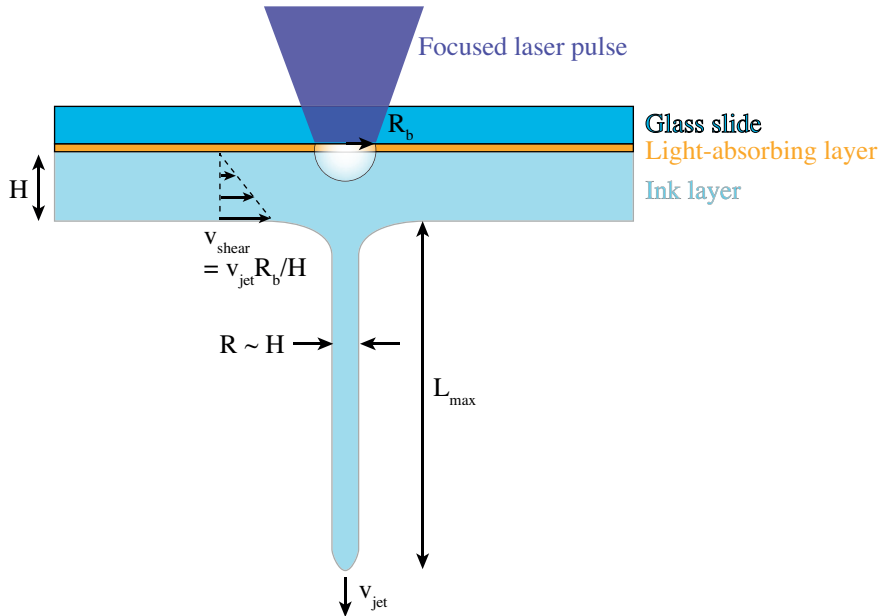


Figure 2.5 – Parameters for droplet generation via laser-induced forward transfer, adapted from [62]

2.3.2 Printability map of laser-induced forward transfer

As in inkjet printing, several criteria were derived from experimental measurements and numerical models to map the different jetting regimes of laser-induced forward transfer [61, 62].

First, the same considerations on the ratio of the capillary and viscous time scales (see Eq. 2.18) apply for laser-induced forward transfer as in inkjet printing. If the ink is too viscous,

2.3. Dimensionless analysis of laser-induced forward transfer

$Oh^* > \sim 1$, viscous effects appear faster than capillary effects and droplet breakup cannot occur, whereas if Oh^* is too low, $Oh^* < \sim 0.1$, multiple droplets are likely to be formed. These two criteria are equivalent to the vertical dashed lines in Fig. 2.6.

Considering the modified Deborah number De^* , two empirical conditions were found: $De^* > \sim 0.02$ and $De^* > Oh^*$ [62]. The first condition states a minimum value for De^* to first form a liquid jet before the liquid relaxes (see the dashed horizontal line in Fig. 2.6), while the second condition sets another minimum value on De^* to additionally induce a liquid breakup. The condition $De^* > \sim 0.02$ can be interpreted as a requirement to induce liquid deformation faster than the liquid relaxation time λ_r (see Eq. 2.24). In the same way, the condition $De^* > Oh^*$ is equivalent to $t_c < \sim \sqrt{\lambda_r t_\mu}$ (see Eqs. 2.18, 2.24, 2.25) which accounts for the fact that capillary breakup of the liquid filament should occur before the combined relaxation and viscous effects appear.

The single-drop jetting regime therefore lies between the vertical dashed lines, derived from the criteria on the modified Ohnesorge number, and above the diagonal line that represents the requirement for a faster droplet breakup than liquid relaxation (see gray region in Fig. 2.6).

Based on this semi-empirical model, Turkoz et al. [62] showed that a prior measurement of the ink's rheological properties allows predicting in which jetting regime laser-induced forward transfer will take place. We use this jetting map to analyze the performances of our experiments on laser-induced three-dimensional embedded printing in chapter 3.

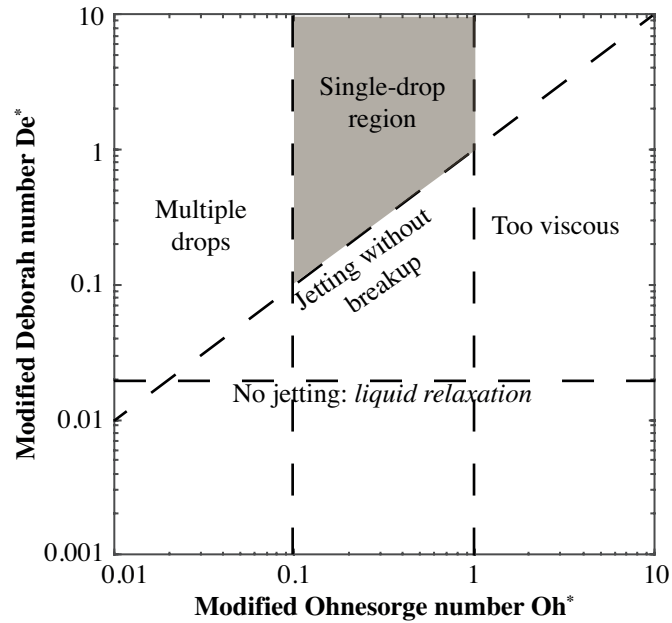


Figure 2.6 – Jetting map for laser-induced forward transfer, adapted from [62]

2.4 Conclusion

The basic concepts of fluid dynamics introduced in this chapter provide simple tools to characterize the rheology of the different fluids used in this thesis. In addition, a comparison of the time scale of the different physical phenomena in action during drop generation allows predicting and analyzing the jetting regimes of both inkjet printing, studied in chapter 4, and laser-induced forward transfer, which we investigate in the next chapter.

3 Laser-induced direct three-dimensional liquid delivery

In this chapter, laser-induced forward transfer is used as a direct three-dimensional liquid delivery tool, with the aim of providing an alternative to nozzle-based embedded printing.

First, the challenges of existing embedded printing techniques are reviewed to motivate the use of laser-induced forward transfer for depth-controlled liquid delivery. I show that direct three-dimensional liquid delivery can be achieved by producing stable liquid jets over a large range of velocity. I further study the potential of this jetting technique as a cell-delivery vehicle and finally discuss the limitations of the current experimental device.

Parts of the material presented in this chapter were submitted to a peer-reviewed journal under the following title:

- Depth-controlled laser-induced jet injection for direct three-dimensional liquid delivery, Paul Delrot, Sylvain P. Hauser, Jan Krizek, and Christophe Moser.

3.1 Introduction and motivation

3.1.1 Microextrusion embedded printing

Three-dimensional embedded printing enables free-form fabrication of soft materials [19]. In this printing technique, a microextrusion printer directly deposits filaments of a soft ink into a volume of support material. The support material has Bingham plastic rheological properties (see section 2.1.2), as the extrusion nozzle translates into it to raster scan the three-dimensional structure, the gel-like support material fluidizes (see Fig. 3.1(a)). On the other hand, this support material has a solid behavior for shear stresses lower than its yield stress. Hence, while this gel-like material allows the nozzle to freely move, it supports the built soft three-dimensional structures, which would otherwise collapse.

Since microextruders generate continuous ink filaments, this printing method is suitable to fabricate bulk structures or closed shells with a resolution between $50\text{ }\mu\text{m}$ and $200\text{ }\mu\text{m}$ [15–17].

Chapter 3. Laser-induced direct three-dimensional liquid delivery

However, optimally mimicking the complex three-dimensional micro-architectures of tissues requires delivering picoliter ink doses with a $\sim 20\text{-}\mu\text{m}$ resolution [24], close to the dimension of a cell. These requirements are currently not met by continuous microextrusion printers.

3.1.2 Drop-on-demand embedded printing

Depth-controlled three-dimensional delivery

Alternatively, I propose to use drop-on-demand printing techniques for direct depth-controlled delivery of picoliter volumes into the gel-like support material. These techniques also have the advantage of being easily parallelized to increase throughput (see chapter 1).

To control the droplet deposition depth, I suggest to exploit the Bingham plastic properties of the support material. Fluidization of the support gel occurs above its yield stress (see section 2.1.2), we thus expect a droplet of ink to puncture and fluidize the support material above a threshold velocity [47]. Above this velocity, the gel behaves as a viscous Newtonian liquid, which will slow down the injected droplets. To build soft three-dimensional microstructures, I therefore propose to perform depth-controlled delivery by varying the droplet velocity, faster droplets being deposited deeper into the support material as described in Fig. 3.1(b).

In this way, targeting a large span of injection depth requires generating microdrops over a wide range of velocity.

Inkjet printing

Among the ink-based printing techniques (see section 1.1.2), inkjet printing offers a microscale printing resolution and can be readily parallelized for high-throughput applications. On the other hand, it can only jet liquids over a limited range of velocity [8, 25] ($1\text{-}30\text{ m s}^{-1}$), as shown in Fig. 3.1(c).

Laser-induced forward transfer

In contrast, laser-induced forward transfer allows jetting viscous materials over a wide velocity range, from 20 m s^{-1} to more than 150 m s^{-1} [48, 49]. In addition, this jetting method offers a high throughput ($>10^4$ drops/s) and a micrometric lateral resolution (see Fig. 3.1(d)) that enable the fast replication of the complex micro-architectures of tissues [8, 9].

Interestingly, controlling the deposition depth of droplets would add a degree of freedom to laser-induced forward transfer, turning this conventional two-dimensional patterning technique into a direct three-dimensional printing technique. Thus, the time-consuming gelation steps currently required when building a microstructure layer-by-layer could be avoided, thus greatly improving the overall throughput of laser-induced forward transfer [51, 53, 54]. Finally, it is noteworthy that the axial printing resolution of laser-induced forward

3.2. Generation of high-velocity jets by laser-induced forward transfer

transfer into a soft material has never been investigated, in spite of extensive research on its lateral printing resolution and precision [50–52].

In this chapter, I first describe the methods employed to laser-induce stable jet of an alginate-based ink. I then show that the velocity of these jets can be controlled by varying the laser fluence, which in turn enables to control the injection depth of the jets in a 300- μm thick volume of gelatin. The potential of this three-dimensional delivery technique for cell-delivery is then further studied.

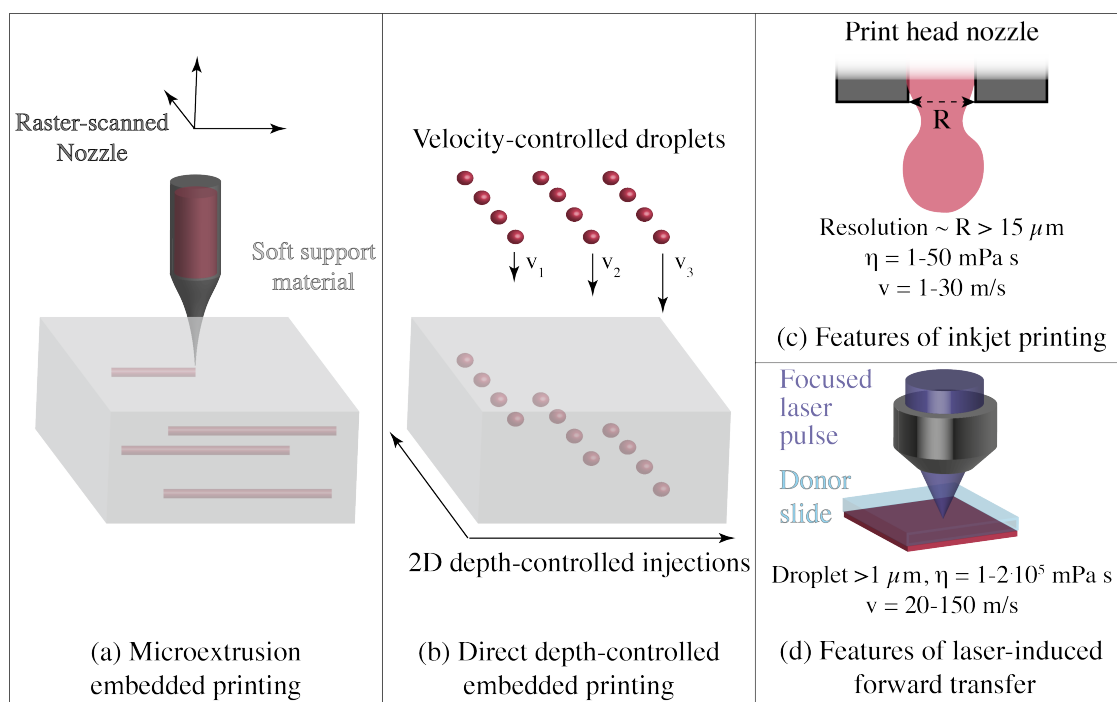


Figure 3.1 – Improving throughput of three-dimensional embedded printing via depth-controlled injection

3.2 Generation of high-velocity jets by laser-induced forward transfer

This section further describes the concept of direct three-dimensional liquid delivery using laser-induced forward transfer. The rheology of the gelatin substrate, essential to this depth-controlled injection, is characterized. The variation of the jet velocity was also calibrated using time-resolved imaging to ensure an accurate jet injection depth.

3.2.1 Methods

Concept and experimental setup

Direct three-dimensional liquid delivery was achieved by adapting a two-dimensional laser-induced forward transfer system developed by Fraunhofer-ILT (LIFTSYS). I realized the adaptation of this commercial laser-induced forward transfer system together with Sylvain Hauser, an EPFL master student.

The principle of three-dimensional liquid delivery is described in Fig. 3.2(a). Upon absorption of a laser pulse, liquid jets are generated from the donor slide. Increasing laser fluences result in faster jets. As their impact velocity increases, these liquid jets penetrate deeper into the gelatin receiver substrate. While this substrate lets the jet flow above a threshold velocity, it acts as a support material once they stopped. This behavior stems from the substrate's Bingham plastic properties, further described in the next section and in section 2.1.2 of chapter 2.

The solid receiver slide typically used in standard laser-induced forward transfer systems was replaced by a 300- μm thick soft gelatin substrate so that microjets were directly injected from the donor slide into this soft substrate (see Fig. 3.2(a)). The donor slide and the top surface of the gelatin substrate were placed 1400 μm apart. Both the donor slide and receiver substrate were carried in the LIFTSYS machine by two-axis stages for two-dimensional lateral motion and patterning.

The donor slide (see Fig. 3.2(b)) consisted of a standard silica microscope slide onto which a 60-nm light-absorptive titanium layer was sputtered (Alliance Concept, DP650). A 30- μm thick layer of liquid ink was then coated with a doctor blade (Elcometer, model 3580) onto this titanium layer. The donor slide was subsequently placed in the LIFTSYS machine where 5-ns UV laser pulses were absorbed by the titanium layer and induced shockwaves, thereby producing liquid microjets of ink [64, 65].

The liquid ink was made of 1% (w/v) sodium alginate (Sigma Aldrich) into a 1:3 (v/v) mixture of glycerin (>99.5%, Roth) and deionized water. To image the depth and morphology of injection, 0.2- μm fluorescent beads (Thermo Fischer, FluoSpheres®F8811) were added to the ink with a concentration of $5 \cdot 10^9$ beads/mL. For the experiments investigating the potential of our technique as a direct three-dimensional cell-delivery vehicle, cell-like fluorescent beads (≈ 10 μm , density: 1.05 g mL⁻¹, Polysciences, Fluoresbrite®YG) were also added to the ink with a concentration of $1 \cdot 10^7$ beads/mL, similar to cell concentrations used in previous studies on cell delivery using laser-induced forward transfer [66, 67].

Gelatin as a soft support material

Previous studies on laser-induced forward transfer systems used either solid receiver substrates when patterning non-sensitive material [65], or receiver slides coated with a thin layer of damping material such as Matrigel or gelatin in order to increase cell viability for

3.2. Generation of high-velocity jets by laser-induced forward transfer

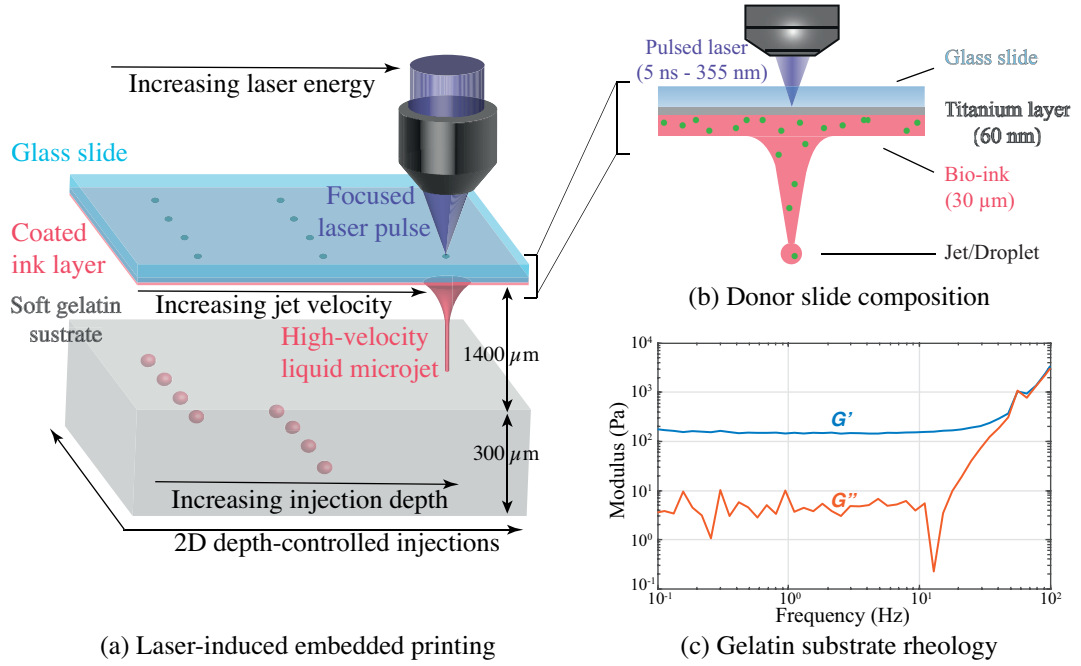


Figure 3.2 – (a) Experimental setup for three-dimensional liquid delivery by laser-induced forward transfer. (b) Composition of the donor slide (c) Rheological analysis of elastic (G') and viscous (G'') modulus for the gelatin receiver substrate showing Bingham plastic behavior

bio-printing applications [50, 68, 69].

In this thesis, to investigate direct three-dimensional liquid delivery, the receiver substrate consisted of a 300- μm thick soft gelatin substrate. Gelatin, as an inert and biocompatible material [70], has been used as a soft tissue model [47, 71, 72] or as a scaffold material for soft tissue engineering applications [73–75]. Interestingly, gelatin exhibits Bingham plastics rheological properties. As shown in the rheological analysis of Fig. 3.2(c), its elastic (G') and viscous (G'') remain constant below a threshold oscillation frequency ($\sim 10\text{Hz}$), which corresponds to a threshold shear stress. This is typical of a solid material. Above the yield stress, the gelatin elastic modulus (G') and viscous modulus (G'') increases linearly, which denotes a Newtonian liquid behavior (see section 2.1.2). In terms of jet dynamics, this means that above a threshold jet velocity, gelatin will be punctured and the jet will flow into it. Once the drag force has sufficiently slowed down the jet, gelatin will act as a solid support material for the injected dose.

Analysis of the depth-controlled injections

In order to perform confocal imaging of the injections, we used coverslip-mounted plastic dishes (MatTek, model P35G-1.5-14-C) as gelatin containers (receiver substrates). A solution of 2% (w/v) gelatin (Sigma-Aldrich, 300 g bloom force) and 0.5% (w/v) CaCl_2 (Sigma-Aldrich) in deionized water was prepared at 37°C and mixed with 0.2- μm fluorescent beads (Thermo

Fischer, FluoSpheres®F8810) at a concentration of $5 \cdot 10^9$ beads/mL. Labeling the gelatin substrate with fluorescent markers orthogonal to that of the injected liquid allowed us determining precisely the top surface of the gelatin volume and the injection depth. The liquid mixture was then poured in the plasma-cleaned dish to form a $300\text{-}\mu\text{m}$ thick volume with a flat top surface. The receiver substrates were stored at 5°C at least for two hours, until experiments took place. The experiments were run at 22°C and lasted 4 min thus not degrading the gelatin's rheological properties, after which the receiver substrates were stored back at 5°C until being imaged. As mentioned above, the injections were imaged with a confocal fluorescent microscope under a protected atmosphere (22°C , $> 85\%$ humidity) to prevent drying of the samples. Finally, the image tiles were reconstructed using an open-source plugin [76].

Time-resolved imaging of jet velocity

The jet dynamics were imaged using a custom-made high-brightness continuous light source combined with a high-speed camera (Vision Research, Phantom Miro M310) mounted with a microscope objective. These time-resolved imaging experiments were performed together with my colleague Jan Krizek.

The dimensions of the LIFTSYS machine allowed us to image the jetting velocity near the donor slide. However, the small space available within the machine did not allow us imaging the impact of the jets onto the soft gelatin substrate.

3.2.2 Control of the jetting velocity with the laser fluence

Precise and efficient three-dimensional liquid delivery requires controlling the injected dose, its dispersion, which we define as the lateral resolution, as well as its injection depth. More specifically, depth-controlled nozzle-free injections demand the production of liquid microjets over a wide range of velocity.

By varying the incident laser fluence on the donor slide (see Fig. 3.2(a)) we demonstrate microjet generation with estimated velocities at impact ranging from 10 m/s to more than 80 m/s (see Fig. 3.3(a)). The estimated velocity at impact on the substrate is measured $1400\text{ }\mu\text{m}$ away from the donor slide, where the top surface of the soft gelatin substrate stands during injection experiments (see the dashed lines in Figs. 3.3(b)-(d)).

Interestingly, our device allows generating stable jets, with a high directionality over this wide range of velocity (see Figs. 3.3(b)-(d)) whereas at high-velocity standard inkjet printers create turbulent jets and satellite droplets, which can degrade the lateral resolution of injection. In the same way, as shown in Figs. 3.3(b)-(d), our laser-based system enables the production of these high-speed jets with a width as small as $\sim 15\text{ }\mu\text{m}$, which also contributes to a finer lateral resolution of injection (see section 3.3.1) than in existing microextrusion embedded printers [15–17].

3.2. Generation of high-velocity jets by laser-induced forward transfer

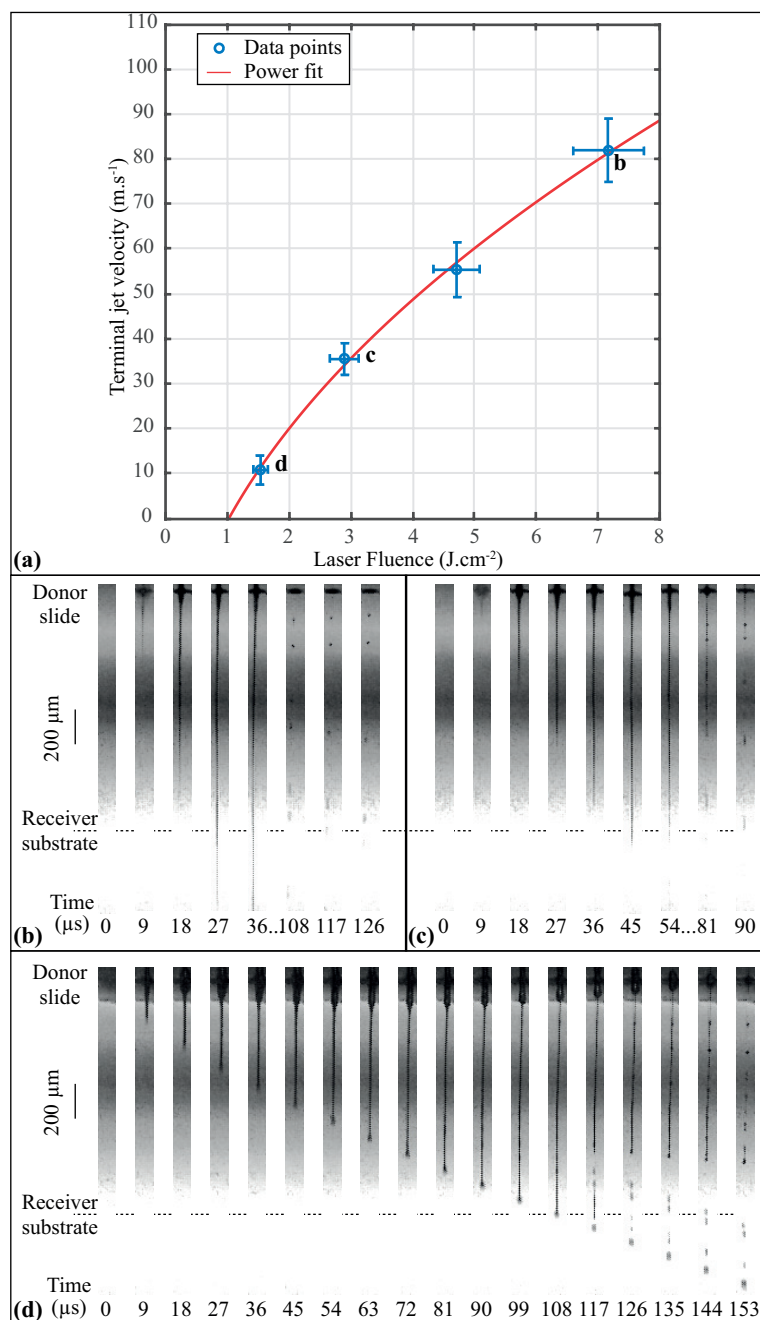


Figure 3.3 – (a) Jet velocity at 1.4 mm from the donor slide as a function of the incident laser fluence on the donor slide (b) Time-resolved imaging of the laser induced jet for a $7.17 \pm 0.57 \text{ J cm}^{-2}$ laser fluence (c) $2.89 \pm 0.23 \text{ J cm}^{-2}$ laser fluence (d) $1.53 \pm 0.12 \text{ J cm}^{-2}$ laser fluence. Low velocity liquid droplets or trailing filaments can be observed for times $>108 \mu\text{s}$, $>81 \mu\text{s}$ and $>99 \mu\text{s}$ in Fig. 3.3(b), 3.3(c) and 3.3(d) respectively. These low velocity volumes are responsible for the liquid deposited on top of the injection sites (see Fig. 3.4(a)).

Laser-induced jets could potentially be produced over an even larger dynamic range of velocity

by increasing the ink's viscosity, as viscosity tends to stabilize laser-induced jet and droplet generation [31, 77]. However, for this study the LIFTSYS's laser experimentally limited us to an upper fluence limit of $7.17 \pm 0.57 \text{ J cm}^{-2}$, therefore the stability of higher velocity jetting could not be investigated.

3.3 Depth-controlled injection for direct three-dimensional liquid delivery

3.3.1 Depth-controlled injection

To assess the ability of laser-induced forward transfer to achieve depth-controlled injections I used the setup of Fig. 3.2(a) with the unseeded ink described in section 3.2.1, and generated grids of 11 by 20 jets, each row of jets being injected with an increasing laser fluence and therefore with an increasing jet velocity (see Fig. 3.3(a)).

Above a threshold velocity, the gelatin substrate was punctured and the injection depth was reproducibly controlled from 0 to $\sim 230 \text{ }\mu\text{m}$, linearly scaling with the jet velocity (see red data points and dashed fit in Fig. 3.4(a)). This linear trend is consistent with the viscous stress model developed by Tagawa et al. [47] in which a viscous drag force, proportional to the jet velocity v , is applied to the liquid as it penetrates into the material. The injection depth D_p , which is the length of the column of material injected, then linearly scales with the jet velocity v as:

$$D_p = \frac{1}{c_v}(v - v_c) \quad (3.1)$$

where c_v is a fitting parameter in s^{-1} and v_c is the threshold velocity for puncturing the material [47], which we find to be $v_c = 7.5 \text{ m/s}$ by fitting the data with this viscous stress model. Such a threshold model is also consistent with the Bingham plastic behavior measured for the gelatin substrate (see Fig. 3.2(c)) since below a yield velocity, the material remains solid to the impact of the jet whereas above this yield velocity, it flows under impact.

The depth precision of the injection is $\pm 25 \text{ }\mu\text{m}$ (see red error bars in Fig. 3.4(a)) while the lateral precision of delivery is $\pm 4 \text{ }\mu\text{m}$ (not depicted here). In addition, the lateral resolution of injection of the laser-assisted device, which is defined as the lateral area over which the delivered liquid is dispersed, is $12 \pm 4 \text{ }\mu\text{m}$ (see cross-sections of injection sites in Figs. 3.4(b)-(d)). This low dispersion of the delivered liquid is likely due to the ultra-thin microjets generated by laser-induced forward transfer (see Figs. 3.3(b)-(d)) rather than the gelation of the alginate-based ink in the Ca^{2+} -rich gelatin substrate. Analyzing the respective penetration time of the jet and gelation time of the alginate-based ink reveals indeed that the injection occurs over a time shorter by several order of magnitude, $\sim 3 \text{ }\mu\text{s}$, than the diffusion [78] of calcium ions over $6 \text{ }\mu\text{m}$, $\sim 30 \text{ ms}$.

3.3. Depth-controlled injection for direct three-dimensional liquid delivery

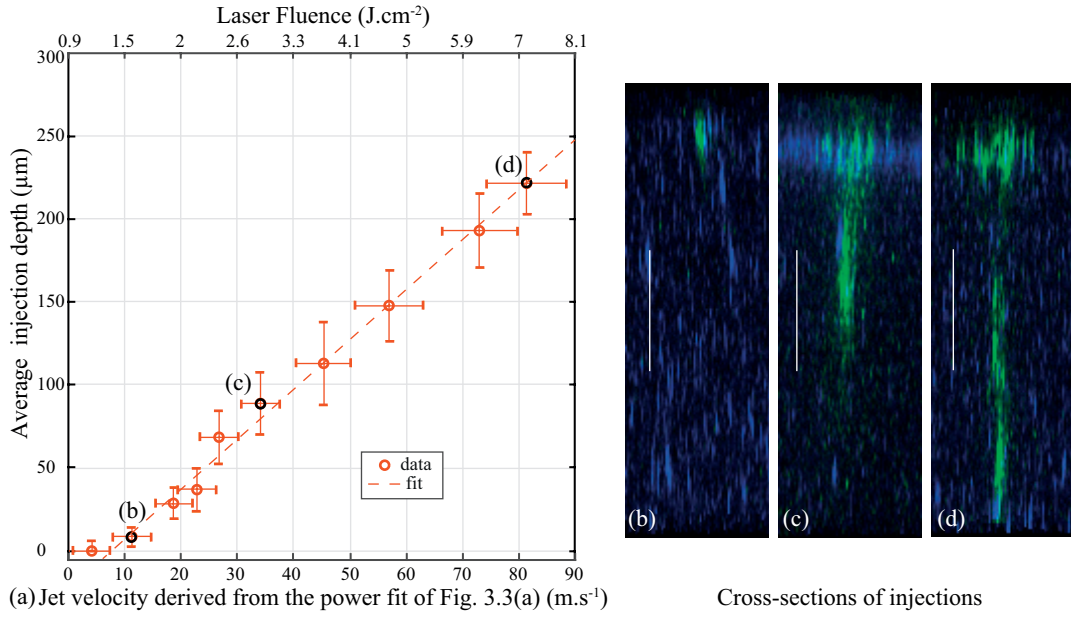


Figure 3.4 – Control of the injection depth by the jetting velocity. The data points are linearly fitted to show consistency with a viscous stress model [47]. Cross-sections of the injected ink are depicted for various data points of the plain ink, scale bar: $100\ \mu\text{m}$, green: injected liquid, blue: soft gelatin substrate

3.3.2 Morphology of injection

Though the principle of laser-assisted depth-controlled injection is validated, the geometry of micro-injections shown in the imaging cross-sections of Figs. 3.4(b)-(d), with a thin injected column of ink capped with a larger volume on the gelatin surface, differs from the desired local deposition at a specific depth depicted in Fig. 3.2(a).

First, as shown in Fig. 3.5, an important part of the jetted volume was not even injected into the material. A possible backflow of the injected liquid towards the substrate surface could account for the presence of this larger volume of liquid on the substrate surface than inside the gelatin substrate. However, such a backflow model would experimentally be evidenced by an asymptotic depth of injection [79], which is not observed in Fig. 3.4(a). Thus, I rather speculate that the volume of liquid appearing on the top surface of injection (see imaging cross-sections of Figs. 3.4(b)-(d)) is due to the low velocity trailing filament and satellite droplets produced at the end of the laser-induced jetting process (see images for times $>108\ \mu\text{s}$, $>81\ \mu\text{s}$ and $>99\ \mu\text{s}$ in Figs. 3.3(b), 3.3(c) and 3.3(d) respectively).

The ratio of injected ink over the whole volume of jetted ink quickly reaches an asymptotic value of $\sim 12\%$ once the jet overcomes the threshold velocity for puncture, as respectively shown with red circles in Fig. 3.5 and Fig. 3.4(a). Improving this ratio would require to either impart the same velocity to the whole body of jetted liquid or to suppress its low velocity components, namely the trailing filament and satellite droplets (see Figs. 3.3(b)-(d)). These

two conditions are equivalent to jetting a single high-velocity droplet, as discussed in section 3.3.4.

Though our laser-based system currently has a relatively low injection efficiency, it allows injecting picoliter doses (see green squares in Fig. 3.5) over a two-dimensional area with a $\pm 25 \mu\text{m}$ depth-control as well as a $\pm 4 \mu\text{m}$ lateral precision and a $12 \pm 4 \mu\text{m}$ lateral dispersion. This micrometric lateral and axial control over the liquid delivery is comparable to the size of a cell and therefore falls within the range of the optimal printing precision for direct three-dimensional delivery of cells or particles [24]. I thus investigate in the next section the ability of the system to deliver particles at a pinpoint location in a volume.

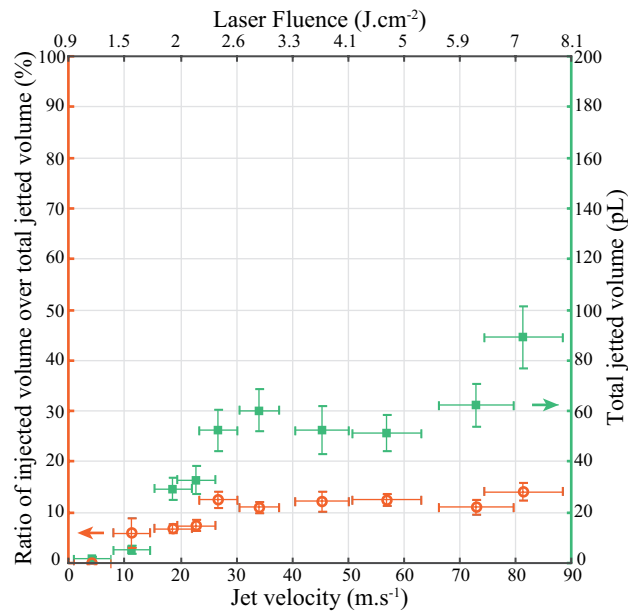


Figure 3.5 – Injection efficiency for the plain ink

3.3.3 Application to particle delivery

Laser-induced forward transfer, as a precise biocompatible printing system, has been extensively used in the past years for two-dimensional cell patterning or to build layer-by-layer three-dimensional tissue engineered constructs [7, 27, 51]. Nozzle-free depth-controlled delivery of cells or particles within soft tissues or support material would for instance enable studying cell responses to specific micro-architectures in a minimally invasive way. To study the potential of our direct three-dimensional laser-based injector to carry a cell-like payload, the liquid ink was seeded with $\approx 10 \mu\text{m}$ fluorescent beads (see section 3.2.1 for further details).

The particle-seeded liquid was injected less deep into the soft gelatin substrate than the plain liquid (see blue and red datapoints respectively in Fig. 3.6(a)), a phenomenon already observed in previous work on needle-free injection [80]. Here, as evidenced by the poorer fit

3.3. Depth-controlled injection for direct three-dimensional liquid delivery

to the viscous stress model (see blue dashed line in Fig. 3.6(a)) compared to the plain liquid, I hypothesize that the seeded particles influence the puncture ability of the jet. The particles are indeed approximately the same size, $\varnothing 10\ \mu\text{m}$, as the jet thickness, $\sim 12\ \mu\text{m}$, which could affect the jet cross-sectional drag area, thus reducing its potential for puncture and penetration.

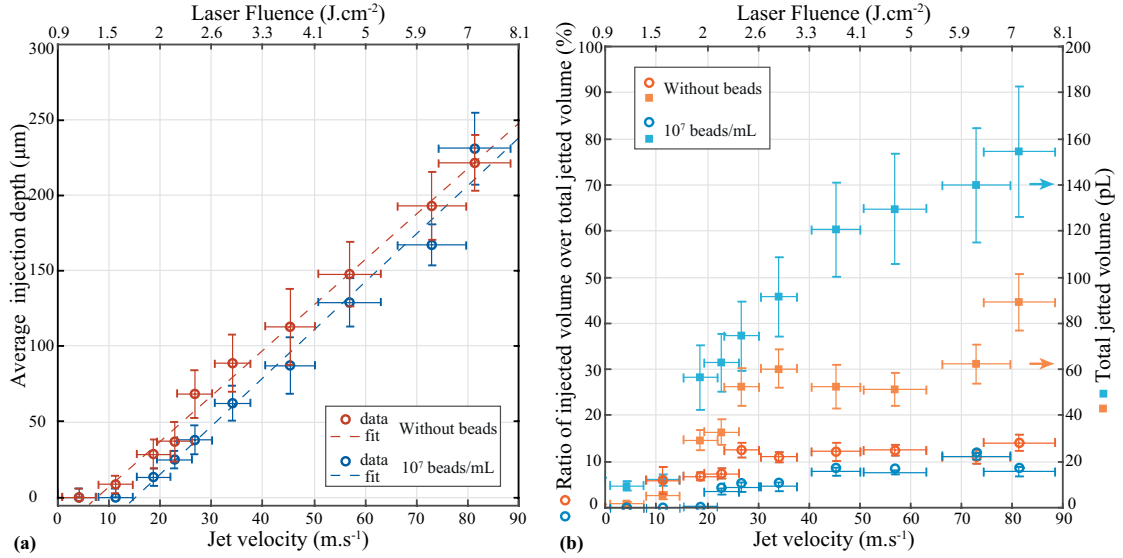


Figure 3.6 – Injection performances of the plain ink and particle-seeded ink (a) Injection depth as a function of the jet velocity and laser fluence (b) Injection efficiency and total jetted volume

The ratio of injected ink over total jetted volume of the particle-seeded liquid is almost halved compared to the plain liquid, reaching an asymptotic value of $\sim 7\%$ (see blue circles in Fig. 3.6(b)), which is caused by the larger amount of liquid jetted with the particle-seeded liquid than with the plain liquid (see blue and orange squares in Fig. 3.4(b)). I speculate that a larger volume of low-velocity liquid was pulled towards the substrate by bead aggregates, possibly induced by capillary forces between beads. This hypothesis is supported by the higher average number of beads deposited per dose than what would be expected from the initial bead concentration in the liquid. As shown in Fig. 3.7, fitting the experimental bead distributions by Poisson distributions [50] reveals that an average 1.15 ± 0.06 and 2.35 ± 0.14 beads per dose are respectively delivered for 2.4 ± 0.2 and $6.3 \pm 0.5\ \text{J cm}^{-2}$ laser fluences, whereas combining the measured dose volume (see blue squares in Fig. 3.4(b)) with the 10^7 beads/mL concentration indicates that 0.75 ± 0.15 and 1.4 ± 0.22 bead per dose would respectively be expected. This inconsistency suggests that beads are forming aggregates prior or during jetting, and are likely to increase the amount of low-velocity liquid transferred towards the gelatin substrate.

However, as shown in the cross-section of injection of Fig. 3.7, I demonstrated that cell-like beads can be injected into a soft gelatin substrate using the laser-based microjet device. The injected beads lie in the $12\text{-}\mu\text{m}$ diameter thin column of liquid depicted in Fig. 3.4(b), thus precise lateral delivery of the cell-like payload can be achieved. Since more volume of liquid

was delivered on the substrate surface than injected into the substrate, the likelihood of bead injection into the substrate is proportionally decreased (see Fig. 3.7). Similarly, this degrades the control over the delivery depth of the particles, as indicated by the green error bar that shows the $\pm 57 \mu\text{m}$ depth deviation of the injected beads for jets generated at $7.2 \pm 0.6 \text{ J cm}^{-2}$ laser fluence.

Embedding particles in a single high-velocity droplet would allow overcoming this limitation to achieve axially localized deposition. Generation of high-velocity single-drops could be demonstrated through modification of the ink rheology as discussed in the next section.

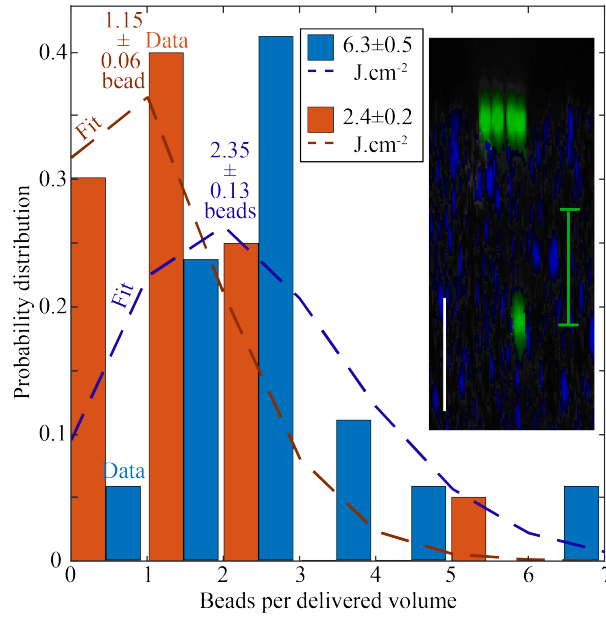


Figure 3.7 – Probability distribution of the amount of beads per delivered dose for two laser fluences. The orange and blue bar plots respectively represent the measured distribution of delivered beads for doses jetted at $2.4 \pm 0.2 \text{ J cm}^{-2}$ and $6.3 \pm 0.5 \text{ J cm}^{-2}$, $N = 20$. The dashed orange and blue lines are Poisson distribution fits to the experimental bead distribution. A cross-section of injection with the seeded ink is shown on the left, several beads (in bright green) are deposited on the top gelatin surface (in blue) while one bead is injected $\sim 170 \mu\text{m}$ into the substrate. The green deviation bar represents the depth-uncertainty on the deposition of beads for a laser fluence of $7.2 \pm 0.6 \text{ J cm}^{-2}$. The image is processed to better distinguish the deposited beads. White scale bar: $100 \mu\text{m}$.

3.3.4 Dimensionless analysis for the generation of high-velocity single-droplet

Direct three-dimensional liquid delivery for embedded printing requires accurately controlling the injection depth of the jetted liquid. I proposed and demonstrated depth-controlled injection by varying the jetting velocity via laser-induced forward transfer. Though experimental results (see section 3.3.1) validated this concept, axially localized liquid delivery would

3.3. Depth-controlled injection for direct three-dimensional liquid delivery

require generating single-droplets over a wide range of velocity. As an outlook, I discuss in this section the changes to operate on the ink composition to perform laser-assisted single-droplet jetting.

Printability diagram

To analyze the jetting regimes of the laser-assisted device, I use the dimensionless printability diagram defined in section 2.3.2.

This diagram is a parametric space of the dimensionless Deborah De^* and Ohnesorge Oh^* numbers, modified to account for the specificities of laser-induced forward transfer [62]. De^* represents the ratio of the characteristic internal relaxation time of the liquid over the time scale of the deformation applied to the liquid. In other words, De^* is used to predict if the liquid jet relaxes before capillary effects arise to break it up into one or more droplets. In the same way, Oh^* is the ratio of the characteristic time scales for capillary and viscous effects to respectively appear.

Using these dimensionless numbers, previous works [61,62] defined a predictive semi-empirical model for the jetting regimes of laser-induced forward transfer, as shown in Fig. 3.8.

Briefly, below a threshold value $De^* \sim 0.2$, the liquid relaxes too fast for jetting to take place (see *no jetting:liquid relaxation* region in Fig. 3.8). In addition, viscous effect will prevent jetting or capillary breakup for large Ohnesorge numbers ($Oh^* > \sim 1$). On the other hand, capillary effects dominate for small Ohnesorge numbers ($Oh^* < \sim 0.1$), thus resulting in the generation of multiple droplets (see *multiple drops* region in Fig. 3.8). Finally, for $Oh^* > De^*$ and $De^* \sim 0.2$, jetting is possible but viscous effects will dominate the jetting process and prevent breakup of the liquid filament (see *jetting without breakup* region in Fig. 3.8). All these criteria allow defining a parametric space for single drop generation, as shown in grey in Fig. 3.8 (see section 2.3.2 for further details on the printability diagram).

Experimental results

By superimposing the experimental data points with the printability diagram, we observe that the experimental parameters lie at the border of the viscosity threshold for breakup (see blue circles and diagonal line $De^* > Oh^*$ in Fig. 3.8).

We effectively imaged jetting with breakup for the lowest velocities (see Fig. 3.3(d)), and jetting without breakup for the highest velocities as accurately predicted by the diagram. However, as $Oh^* \sim 1$ for our ink, we do not expect the filament to breakup and generate multiple drops as experimentally imaged (see Fig. 3.3(d)).

Table 3.1 summarizes the parameters used for plotting the experimental results, as well as their references.

Parameter	Value	Reference
R jet thickness (m)	$15 \cdot 10^{-6}$	experimental data
v_{jet} mean jet velocity (s^{-1})	10-81	experimental data
$\dot{\gamma}$ shear rate (s^{-1})	$0.35-6.8 \cdot 10^5$	experimental data
σ ink surface tension (N m)	$44.6 \cdot 10^{-3}$	[61]
ρ ink density ($kg\ m^{-3}$)	1010	[61]
$\eta(\dot{\gamma})$ ink viscosity (Pa s)	$27 \cdot 10^{-3}$	[81]
v_c breakup speed ($m\ s^{-1}$)	1.7	[62]
λ_r characteristic relaxation time (s)	$560 \cdot 10^{-6}$	[61]
De^* modified Deborah number	0.46-3.3	experimental data, [61, 62, 81]
Oh^* modified Ohnesorge number	1.0	experimental data, [61, 81]

Table 3.1 – Parameters for the dimensionless analysis of the laser-induced jetting regimes

Predictive jetting regimes with modification of the ink

The ink being composed of water, glycerol and sodium alginate (see section 3.2.1), changing the concentration of sodium alginate appears to be the most straightforward way to change the ink relaxation properties.

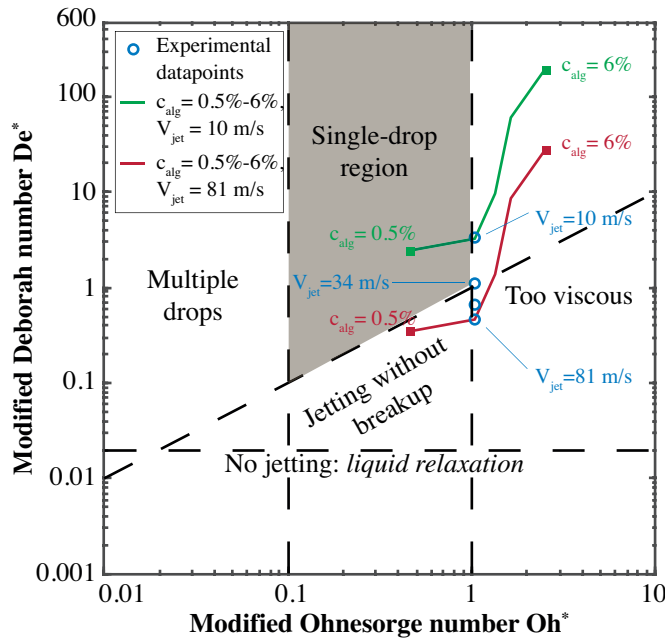


Figure 3.8 – Dimensionless analysis of the laser-induced jetting process

Not only will a modification of sodium alginate concentration change the characteristic relaxation time of the ink [61], but it will also modify the ink's viscosity [81]. A decreasing sodium alginate concentration c_{alg} will result in a shorter relaxation time λ_r and therefore in

a decreasing Deborah number De^* ¹. Similarly, a decreasing sodium alginate concentration will result in a decreasing viscosity and therefore in a decreasing Ohnesorge number Oh^* .

Assuming that the concentration change of sodium alginate does not affect the jetting velocity, I plotted the parametric curve $Oh^*(c_{alg})-De^*(c_{alg})$ for sodium alginate concentration between 0.5% and 6% of the volume and 10-m s⁻¹ and 81-m s⁻¹ jetting velocities, as respectively depicted by the green and red curves in Fig. 3.8.

We observe that stable single-droplet generation is more likely to take place if the sodium alginate concentration is decreased. This physically means that capillary effects are favored by this concentration decrease, which will be studied in future work.

3.4 Conclusion

In this chapter, to provide an alternative to microextrusion-based embedded printing, I demonstrated depth-controlled liquid injection into a 300- μm soft gelatin substrate over two dimensions, thus achieving direct three-dimensional liquid delivery. The injection depth was controlled by producing 15- μm stable liquid streams over a wide range of velocity with a laser-induced forward system.

The axial resolution of delivery is currently limited by the injection profile, as the low-velocity components of the laser-induced jets are not injected into the substrate. Since no splash back of the high-velocity jets was experimentally observed at the impact on the gelatin substrate, a possible solution would be to generate high-velocity single-droplets instead of jets. In this way, the whole liquid volume would travel at the same velocity and would thus be injected at the same depth. A dimensionless analysis of the jetting regimes reveals that single-droplet generation could be achieved by lowering the ink's concentration in sodium alginate.

Finally, as this system can deliver picoliter doses up to depth of $\sim 230 \mu\text{m}$ with a 25- μm depth repeatability and a 12- μm lateral resolution, it could offer a precise and high-throughput alternative to existing needle-free microjet injectors [82].

¹It is noteworthy that the ink's surface tension and density will also slightly evolve with the sodium alginate concentration, which we account for plotting the curves of Fig. 3.8

4 Compact laser-assisted inkjet printing of highly viscous fluids

In this chapter, a flow focusing phenomenon is exploited to laser-induce viscous microdrops on demand through a glass microcapillary, which constitutes the first part of my compact toolkit for high-resolution additive manufacturing.

I first introduce the challenges of drop-on-demand generation and then present the hydrodynamic phenomenon that allows generating high velocity jets through a glass microcapillary. I show that this laser-induced flow focusing phenomenon can be exploited to produce monodisperse droplets with a wider range of viscous materials than conventional inkjet printers. I finally investigate the biocompatibility of the drop-on-demand device and discuss how to further compact it.

Some of the material presented in this chapter can be found in the following paper:

- Paul Delrot, Miguel A. Modestino, François Gallaire, Demetri Psaltis, and Christophe Moser. Inkjet Printing of Viscous Monodisperse Microdroplets by Laser-Induced Flow Focusing. *Physical Review Applied*, 6(2):024003-1:024003-8, August 2016.

4.1 Introduction

Integrating several printing techniques into a single platform requires miniaturizing each additive manufacturing tool. In this frame, the desired compact ink delivery tool should accommodate a wide range of printable materials, while being able to dispense an amount of ink as small as possible to achieve an optimal printing resolution.

Microextrusion (see section 1.1.2 and Fig. 4.1(a)) has the widest range of printable inks among the different ink delivery techniques, with viscosities ranging from 30 mPa s to $> 6 \cdot 10^7$ mPa s [8]. Though it can produce micrometric-thin filaments of ink through a thin nozzle, its continuous mode of operation precludes its use for high-resolution material delivery. On the other hand, compact inkjet print heads (see section 1.1.2 and Fig. 4.1(b)) allow delivering single droplets of ink with volumes in the picoliter range. However, this jetting technique has

Chapter 4. Compact laser-assisted inkjet printing of highly viscous fluids

a limited range of printable liquids, since the ink viscosity should remain between 1 and 50 mPa s [8, 25] to avoid clogging of the nozzle.

Alternatively, nozzle-free approaches have been used to circumvent nozzle-clogging issues, for instance photoacoustic actuation [83] or laser-induced forward transfer [84]. Thanks to its unconfined geometry, laser-induced forward transfer can be employed with a micrometric resolution for the deposition of highly viscous biological inks (1-300 mPa s) [8,9] and functional inks (>200 Pa s), such as silver nanoparticle suspensions [85] (see section 1.1.2 and Fig. 4.1(c)). However, the planar geometry of laser-induced forward transfer prevents its use as a compact drop-on-demand device.

A more compact implementation of laser-actuated liquid jetting was recently implemented to generate high-velocity jets for needle-free drug delivery [46, 47, 86]. In this technique, a nanosecond laser pulse is focused on an water-filled glass microcapillary, thus vaporizing part of the liquid and producing a shockwave (see Fig. 4.1(d)). Owing to the curvature of the liquid meniscus and the axisymmetry of the microcapillary, the laser-induced flow is focused and allows generating supersonic jets one order of magnitude smaller than the capillary size.

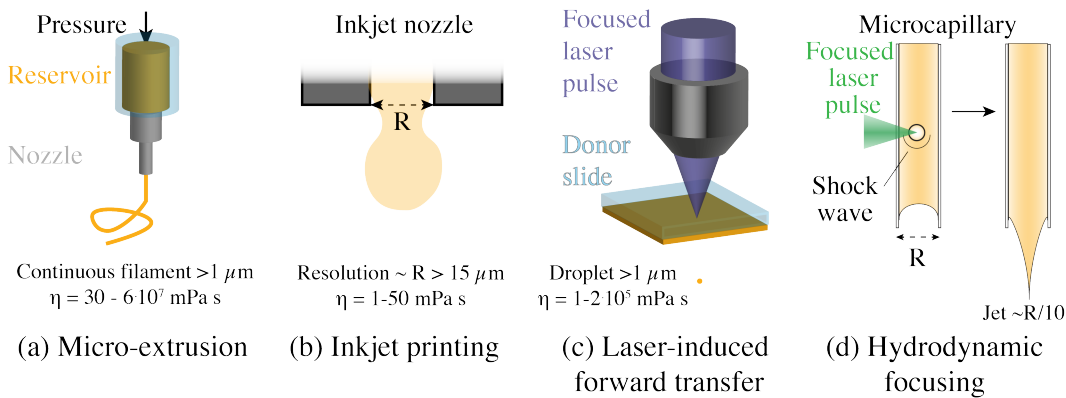


Figure 4.1 – Principle and performances of ink delivery systems (η : ink viscosity)

To develop the compact drop-on-demand device of my high-resolution additive manufacturing toolkit, I use the same flow focusing effect in a 300- μm microcapillary with the aim of broadening the range of functional materials that can be printed using conventional inkjet printers. This flow focusing jetting method can indeed generate liquid streams smaller than the nozzle from which they originate, which has the potential to overcome the nozzle clogging limitations of conventional inkjet printers. In addition, this device could potentially be arranged in a compact setup since laser actuation can be provided through ultra-thin light guiding media, such as multimode fibers.

In this chapter, I study the jetting regimes of this laser-actuated inkjet printer with a wide range of viscous liquids. The achievable printing resolution and biocompatibility of the drop-on-demand device are then investigated.

4.2 Generation of viscous monodisperse droplets by laser-induced flow-focusing

Prior to measuring the printing performances of the drop-on-demand device as a function of the inks' rheological properties, its jetting dynamics are studied and the subsequent jetting regimes are calibrated as a function of the laser energy. To do so, a time-resolved imaging setup was built together with a precise energy monitoring, as described in the next section.

4.2.1 Experimental setup

Methods

Micro-drops were produced at room temperature by focusing a 5-ns laser pulse (Continuum, ML-II, 532 nm) with a 10x microscope objective on a liquid-filled glass microcapillary (see Fig. 4.2(a)). The laser pulse was split in two arms by a polarizing beamsplitter, and the energy was then calibrated to a ratio 1:1 between the microscope objective focal spot and the energy-meter arm thanks to a half-wave plate. The energy sent on the liquid was thus monitored with the energy-meter (Thorlabs, ES111C) and adjusted using optical density filters and the laser internal variable attenuator. Time-resolved imaging of the droplet generation was achieved by synchronizing a custom-made LED-based pulsed Köhler illumination and a fast camera (Vision Research, Phantom Miro M310) with a delay generator (Berkeley Nucleonics, Model 577).

The glass micro-capillary, which takes the role of the nozzle of the drop-on-demand device, was set in a upright configuration (see Fig. 4.2(b)) as in conventional inkjet printers. The Bond number $B = \Delta\rho g(D/2)^2/\sigma$ [46] which represents the ratio of the gravitational and surface tension forces is estimated to be between 10^{-4} and 10^{-2} for the different capillary sizes (where $\Delta\rho$ is the density difference between the liquid and air phases, g the acceleration of gravity, D the diameter of the capillary and σ surface tension of the liquid). Hence, gravity is not expected to significantly affect the actuation of the liquid in the micro-capillary, nor the meniscus concavity.

A hydrophobic treatment [87] (1H,1H,2H,2H-perfluorooctyltrichlorosilane, ABCR, Germany) on the tip of the capillary pinned the contact line of the meniscus. In this way, the contact angle θ of the meniscus and the distance Z between the laser focal spot and the meniscus was controlled via gentle actuation of the syringe pump (New Era Pump Systems Inc, NE-1000) connected to the upper end of the capillary. Borosilicate glass micro-capillaries with inner diameters D ranging from 100 to 300 μm were used (Capillary Tube Supplies Ltd for the 100 and 200- μm capillaries, BLAUBRAND intraMark for the 300- μm capillaries). The droplets were deposited on glass microscope slides actuated by a two-axis microscope stage (Thorlabs, MLS203-1).

Formulation of the inks

The shear-thinning polymer precursor solutions were stained with an organic dye, oil red EGN (Aldrich, USA) at a 56-mM concentration to absorb laser light at 532 nm. These solutions were: 1,6-hexanediol diacrylate (HDDA; 80%, Aldrich, USA) and trimethylolpropane triacrylate (TMPTA; >70%, Aldrich, USA), which were mixed with 2 wt% phenylbis(2,4,6-trimethyl-benzol)phosphine oxide (PI; 97%, Aldrich, Germany) as a photo-initiator. SU-8 with 50% solid content (SU-8; Gersteltec, Switzerland) was also used as received. Dynamic viscosity and surface tension of the non-newtonian liquids were respectively measured with a rheometer at low shear rates (Malvern Instruments Ltd, Bohlin CVO 120) and using the pendant drop method [88].

Newtonian mixtures of water and glycerol (99.5%, Rotipuran, Roth, Germany) were studied as a model for bio-inks and for comparison with the non-Newtonian behavior of the polymer precursor solutions and stained with 52 mM of Allura Red AC (ARAC; 80%, Sigma Aldrich, USA). The dynamic viscosity (2 to 210 mPa s) and density of these mixtures were estimated with Cheng's empirical formula [89], variations of the lab temperature were monitored during the experiments.

Further information on the rheology of Newtonian and non-Newtonian liquids is available in chapter 2.

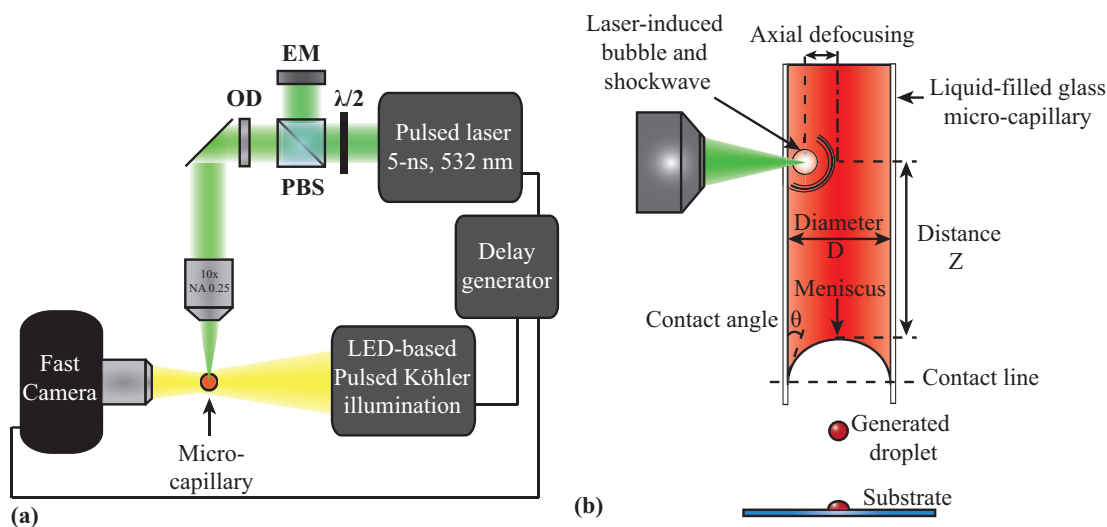


Figure 4.2 – Experimental setup: (a) top-view of the time-resolved imaging setup, the capillary axis is perpendicular to the graph, $\lambda/2$: half-wave plate, PBS: polarizing beam-splitter, EM: energy-meter, OD: optical density; (b) side-view of the micro-capillary in which the droplets were generated and description of the experimental parameters impacting the droplet size and velocity.

4.2.2 Dynamics of flow-focused jetting

The mechanisms underlying the dynamics of droplet formation in my experiments (see Fig.4.3(a-b)) correlate well to those described by Peters et al. [86] for the generation of thin supersonic jets from water-filled capillaries [46].

At time $t = 0 \mu\text{s}$, a laser pulse is fired and absorbed by the dyed solution, hence creating a bubble (see upper left corner of the picture at time $t = 150 \mu\text{s}$ in Fig.4.3(a)). The consequent instantaneous pressure pulse first accounts for the acceleration of the liquid-air interface (see Fig.4.3(b)). The concavity of the meniscus helps to focus the flow along the axis of the capillary and results in a further acceleration of the jet.

The wetting properties of the solutions on the glass capillary were demonstrated both experimentally and theoretically to be critical for the flow focusing [46, 86, 90, 91], with narrow contact angles resulting into thinner jets. Therefore, in order to jet droplets as small as possible to ensure an optimal printing resolution, the wetting interactions between the solutions and the capillary were controlled to keep a low contact angle. Following the acceleration phase, the bubble collapse and the fluid surface tension slow down and stretch the jet (see Figs. 4.3(a-b)) until it breaks up. With a correct tuning of the laser energy, satellite-free droplet generation of viscous liquids was achieved, as shown Figure 4.3(a) (see Section 4.2.3 for more details on the jetting regimes).

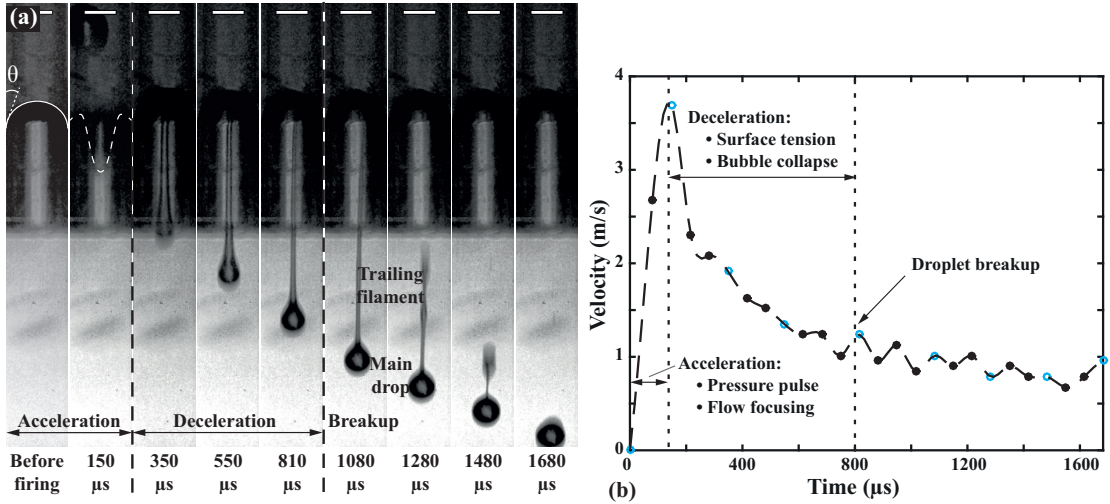


Figure 4.3 – (a) Time-resolved imaging of the flow-focusing phenomenon, the 300- μm capillary was filled with a mixture of water-glycerol (67 mPa s viscosity at 25°C). The liquid-air interface is highlighted with respectively a solid and dashed white line for clarity on the first two images corresponding to pre-firing and post-firing of the laser. The lateral borders of the images correspond to the inner capillary walls. The black surroundings below the meniscus are due to distortion induced by the glass thickness of the capillary. Scale bar: 200 μm . (b) Jet dynamics corresponding to the droplet formation depicted in Fig. 4.3(a) (dashed line: spline interpolation). The blue circles are the data points corresponding to the pictures of Fig. 4.3(a).

Thermal and piezoelectric actuators are able to trigger repeatable pressure pulses, which contribute to the precision of commercial inkjet printers. In order to achieve a reproducible generation of jets and droplets with my laser-assisted drop-on-demand device, I designed the experiments so that the laser pulse was absorbed in a well-defined focal volume of liquid from one experiment to another. Hence, the solutions were stained to absorb 90% of the laser light within a 10- μm liquid thickness. In the same way, the laser focal spot was axially translated with respect to the capillary axis, to be focused in proximity of the capillary's inner wall (see Fig. 4.2(b) and Fig. 4.3(a)). Under these conditions the off-axis location of the laser-induced bubble, did not impact the axisymmetry of the flow-focusing provided that the distance $Z > 1.5D$ for most solutions (see Fig. 4.2(b)), or $Z > 2D$ for highly viscous fluids.

Another important feature of inkjet printers is their printing speed, which is typically more than 10 kHz for conventional inkjet printers. The rates achievable by my drop-on-demand device could approach this range in the case of low viscosity solutions, as they are only limited by the time for the meniscus to set back to its initial position after droplet generation. For a 300- μm capillary, this corresponded to $\sim 500\ \mu\text{s}$ for the least viscous liquids to $\sim 2000\ \mu\text{s}$ for the most viscous inks, as shown in Figs. 4.3(a-b), which would potentially result in repetition rate between 2 kHz and 500 Hz. However the effective repetition rate of my drop-on-demand system could not be investigated due to the low operating frequency of the pulsed laser (15 Hz).

4.2.3 Jetting regimes for Newtonian and non-Newtonian inks

Production of satellite-free micro-droplets is of high interest [92–94] since satellite drops negatively impact the quality of printing. Hence, I characterised the jetting regimes of the laser-assisted device to ensure that a single minimal volume of liquid is dispensed at a time.

The interplay of dynamic viscosity of the jetted inks and the laser fluence was demonstrated to be of importance in laser-induced forward transfer, which is a similar process to the one used in my experiments, though nozzleless. For both Newtonian [77] and non-Newtonian inks [95], viscous inks tended to stabilise the jets and allowed to select the stable printing regime on a larger range of laser fluence, thus avoiding the need for fine adjustments of the laser.

Here, with increasing laser pulse energy three different jetting regimes were observed, which were also viscosity-dependent: a sub-threshold regime, a satellite-free jetting regime and a regime with multiple droplet generation. First, at low pulse energy, only a bubble was observed without droplet generation (see regime I in Fig. 4.4(a-b)). Even if a sufficient amount of laser energy was absorbed to generate a cavitation bubble, the transferred kinetic energy to the open interface of the liquid was insufficient to accelerate the fluid to a point of breakup. Within this regime surface energy and viscous dissipation prevented the formation of droplets.

By increasing the laser energy, a satellite-free jetting regime was observed with an energy threshold specific to each ink (see regime II in Figs. 4.4(a-b)). At the upper energy end of this

4.2. Generation of viscous monodisperse droplets by laser-induced flow-focusing

regime, two droplets could be noticed before their coalescence. Interestingly, the range of pulse energy over which stable satellite-free droplet generation was achievable increased with the dynamic viscosity of the liquids for both Newtonian and non-Newtonian inks, which is consistent with the results mentioned above for laser-induced forward transfer [77, 95]. This result is likely dominated by the interplay of two competing phenomena: the axial contraction of the trailing liquid filament attached to the main drop which favors satellite-free drop formation (see Fig. 4.3(a)) and the radial collapse of this filament, which on the contrary leads to the formation of satellite droplets [96]. In the case of more viscous fluids, the radial collapse would be delayed through viscous dissipation, allowing the formation of satellite-free drops even for high pulse energies that generate long trailing filaments [96].

Moreover, the velocity of the Newtonian inks at breakup of the generated satellite-free droplets was measured to be of the order of 1-2 m/s, which is low enough to prevent the micro-droplets from splashing on the substrate [97]. On the other hand, the non-Newtonian TMPTA and SU-8 droplets had significantly slower velocity at breakup (0.5-1.5 m/s) and drop pinch-off was also significantly delayed with respect to the Newtonian inks. Previous studies showed that polymer viscoelasticity and specifically polymer extensional strain hardening [98, 99] accounts for this phenomenon. For the same reason, we would expect satellite-free droplets to be generated with more ease and therefore on a larger energy range using the polymer shear-thinning inks. Indeed, thanks to their elasticity, polymer inks have been demonstrated [94] to be more resistant to the capillary-driven radial necking of a filament following a main drop (see for instance Fig. 4.3(a)). However, this expected behaviour cannot be clearly extrapolated from my results as seen in Figs. 4.4(a-b).

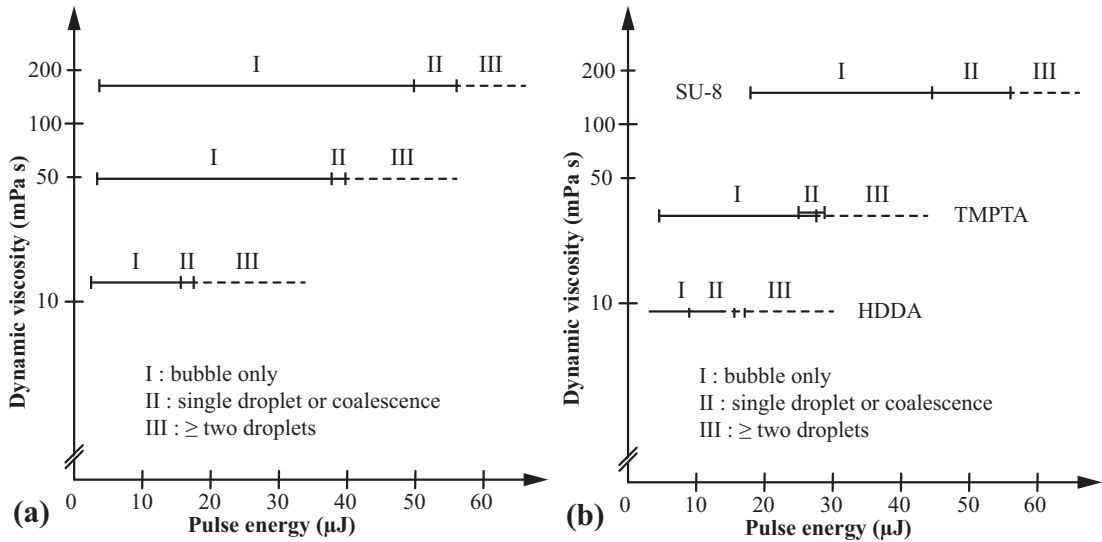


Figure 4.4 – Jetting regimes of inks with various dynamic viscosity for the same capillary diameter (300 μm), the y-axis has a logarithmic scale, the distance Z between the laser focal spot and meniscus was kept constant at 500 μm. (a) Newtonian water-glycerol solutions. (b) Non-Newtonian polymer solutions.

Finally, when a higher pulse energy was used, a third jetting regime was observed in which a faster, longer and thinner jet was ejected and broke up into two droplets or more (see III in Fig. 4.4(a-b)).

As shown in Fig. 4.4(b), the ejection of TMPTA satellite-free droplet overlapped with the two other ejection regimes, which resulted from a poor reproducibility of the jetting process with TMPTA. Micro-aggregates of the light-absorbing dye were observed in the capillary, possibly due to a saturation of the ink with the dye and we believe that the inhomogeneous distribution of the dye resulted in this poor reproducibility. For the other solutions, the cross-over between the satellite-free regime and the other regimes was measured to be between 7 and 18% of the satellite-free energy range, thus leaving a sufficient working range for stable satellite-free droplet generation.

4.3 Printing performances

Having demonstrated that stable satellite-free drop generation can be performed over a large range of viscous inks for specific energy ranges, I evaluated the printing performances of our drop-on-demand device with respect to standard inkjet printers.

4.3.1 Range of printable liquids

To compare the performances of the laser-assisted device to conventional thermal and piezo-electric inkjet printers, I used the dimensionless printability diagram defined in section 2.2.2.

This diagram is a parametric space of the dimensionless Reynolds Re and Ohnesorge Oh numbers, which respectively represent the ratio of inertial and viscous forces and the ratio of the time scales for capillary and viscous effects to appear. Using these dimensionless numbers, previous works defined a semi-empirical model for the range of materials printable by conventional inkjet printers, as shown in the grey region in Fig. 4.5 (see section 2.2.1 for further details on the printability diagram).

By superimposing the experimental data points for the Newtonian mixtures to this printability diagram, we observe that the range of Ohnesorge numbers for which satellite-free droplets were generated is extended to $\sim 0.01 < Oh < \sim 1.5$ with the laser-assisted flow-focusing drop-on-demand system, whereas the standard printable region of inkjet printers is limited to $\sim 0.1 < Oh < \sim 1$, as shown in Fig. 4.5.

This result is in good agreement with the work of Castrejón-Pita et al. in which droplets were produced from large nozzles thanks to piezoelectric-driven flow focusing [60]. The most plausible explanation for this extension of the satellite-free ejection regime with respect to conventional inkjet printers is that my device is less sensitive to viscosity. Indeed, the measured initial velocity of the jet in the case of satellite-free droplet generation was in the range 4-7 m/s for both Newtonian and Non-Newtonian inks and all the capillaries I tested.

Such initial velocities correspond to $Re \sim 200$ for the least viscous inks and to $Re \sim 5$ for the most viscous ones. The initial acceleration phase was then inertia dominated for the range of viscous liquid studied, which is also consistent with previous works [86, 90] on both inviscid and low-viscosity liquids.

Furthermore, as shown in Fig. 4.5, it appears that my experimental data points are roughly located along the line representing the surface energy barrier defined by Derby [58] as: $We \approx 4$. This is due to the fact that I experimentally adjusted the laser pulse energy to be slightly above the droplet generation threshold in order to obtain satellite-free drops. Therefore, the kinetic energy imparted to the droplets was close to the surface energy threshold, which corresponds to the criterion $We > 4$.

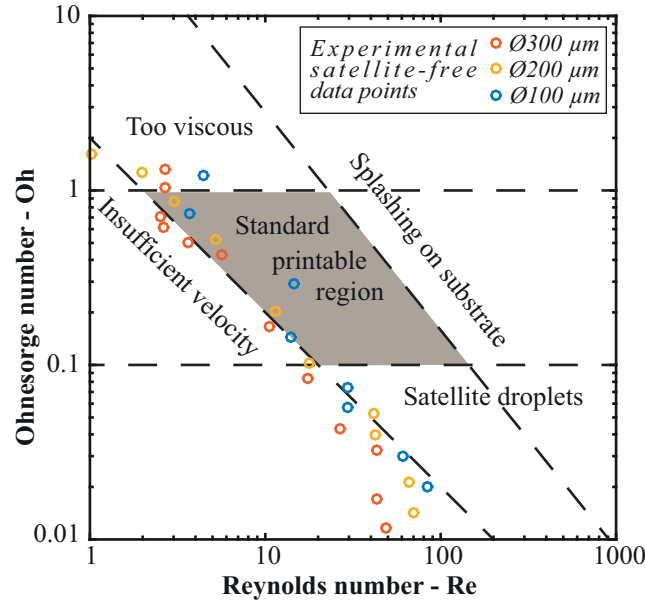


Figure 4.5 – Conventional inkjet printability region adapted from [58, 60] superimposed with the experimental data points obtained with our laser-assisted flow-focusing device in the satellite-free jetting regime and with the water-glycerol Newtonian mixtures. Red, yellow and blue dots were respectively obtained for 300, 200 and 100- μm capillary diameters. Error bars are omitted for clarity, each data point is the results of at least 10 experiments.

4.3.2 Printing resolution

The data of Fig. 4.5 can be further rescaled to provide a master curve for the resolution capability of the laser-assisted device as a function of the Ohnesorge number of the jetted Newtonian liquids, (see Fig. 4.6).

The general trend observed in Fig. 4.6 for all capillary sizes is a rapid increase of the droplet diameters with Oh for $0.01 < Oh < 0.2$ followed by a plateau for higher Ohnesorge numbers.

This plateau shows that the size of the droplets produced by my device has little dependency on the inks viscosity for highly viscous solutions. This is a promising feature since droplets of even more viscous solutions could possibly be produced without significant impact on the drop size.

However, experimental results suggest that the upper limit of ejection of viscous liquids is set by the laser-induced bubbles. For highly viscous liquids, the cavitation bubbles expanded along the capillary axis and surface tension led to the formation of static bubbles inside the capillary thus preventing further droplet generation. A way to circumvent this issue would be to generate multiple bubbles, instantaneously or not, to create multiple pressure waves whose intensity would superimpose on the open liquid interface.

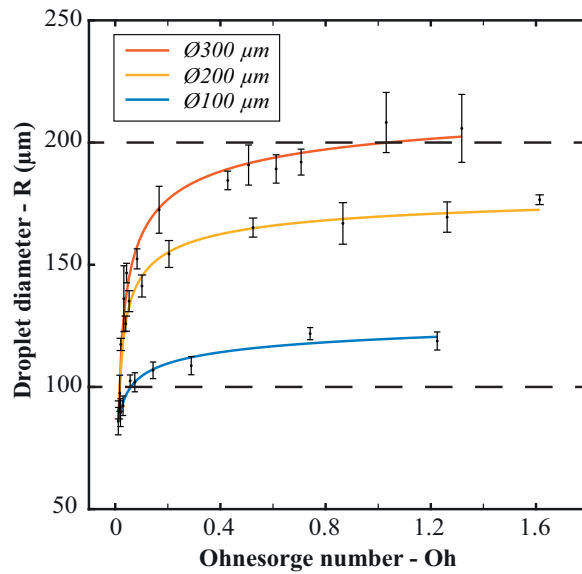


Figure 4.6 – Satellite-free drop diameter of water-glycerol mixtures as a function of the Ohnesorge number for various capillary sizes. The distance Z between the laser focal spot and the meniscus was kept constant at $Z = 500, 400$ and $350\mu\text{m}$ respectively for $D = 300, 200$ and $100\mu\text{m}$. Power law fits are also displayed. Each data point is the result of at least 10 experiments.

As shown in Fig. 4.6, satellite-free droplets with a size smaller than the nozzle from which they originated were generated up to $Oh > 1.3$ (corresponding to viscosities up to 210 mPa s) for capillary diameters $D = 300\mu\text{m}$ and $200\mu\text{m}$. For a smaller orifice diameter, $D = 100\mu\text{m}$, the droplets of viscosity up to 110 mPa s ($Oh \sim 1.2$) were approximately equal to the size of the nozzle. Thus, by scaling down the orifice of the drop-on-demand device, the advantage of the sub-nozzle resolution was lost. A possible explanation for this result is that at a smaller nozzle scale the time for viscous effects to arise is comparable to the flow-focusing time of the device. In other words, viscous dissipation would degrade the geometry of the flow focusing. However, further theoretical studies of the phenomena can help clarify how the droplet size relates to the tube radius as well as to interpret the trend of the master curves of Fig. 4.6.

4.4 Biocompatibility of the laser-actuation

Bio-inks are highly sensitive to heat and could therefore be degraded during the laser-induced drop generation. In order to assess the potentiality of the laser-assisted drop-on-demand device to deliver biomolecules, bio-inks respectively containing mouse and rabbits immunoglobulins (IgGs) were printed on poly-L-lysine slides. An immunoassay was performed to check the integrity of the deposited IgGs following the protocol of [100].

The droplets were generated in the satellite-free jetting regime (see section 4.2.3) and columns of rabbit IgGs were alternatively printed with columns of mouse IgGs on a slide placed 2 mm below the capillary tip. Prior to drying and blocking the slides with bovine serum albumin, the array was imaged under bright field microscopy (see Fig. 4.7(a)). The droplets were generated with a good reproducibility and controllability, as showed in Fig. 4.7(a-b), and even when multiple droplets were generated, the axisymmetry of the jet allowed us to keep a clean printing process.

Finally, after washing the slides, an immunoassay was performed with Cy3-conjugated secondary antibodies against rabbit IgG and Cy5-conjugated secondary antibodies against mouse IgG. The fluorescent marking was specific to the mouse and rabbit IgGs (see Fig. 4.7(b)), thus demonstrating that the functionality of the IgGs was not affected by the laser-assisted printing process. This is achieved as only a small fraction of the biomaterials is exposed to the laser pulse, while the bulk of the printed material is not expected to exhibit a significant temperature increase during the process.

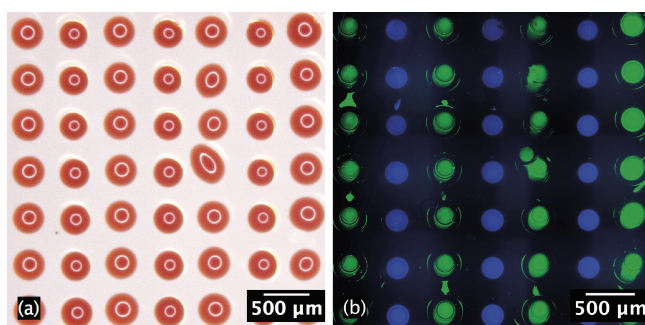


Figure 4.7 – (a) Array of droplets (60%(v/v) of glycerol in PBS) with rabbit and mouse IgGs imaged with a bright-field microscope prior to droplet drying. All droplets appear red due to the light-absorbing dye. (b) The same array imaged under fluorescence after drying the droplet and performing an immunoassay with fluorescent-labelled secondary anti-IgGs against rabbit (in blue) and mouse (in green) (false colors).

However, at high operating frequencies, the temperature rise in the system may become important. The role of thermal effects in the growth and collapse of a laser-induced bubble was investigated by Sun et al. [101] in a water-filled micro-capillary. With similar experimental conditions to mine, they reported an abrupt rise of the bubble vapor temperature to $\sim 170^{\circ}\text{C}$ for a few microseconds, followed by a decrease to $\sim 60^{\circ}\text{C}$ in $\sim 400\ \mu\text{s}$. Similarly, in thermal inkjet

printing, in which the fluid is also bubble-actuated, inks are heated to 200-300°C for $\sim 2 \mu\text{s}$ [8], resulting in a general temperature rise of 4-10°C in the print head at a high frequency (3.5 kHz) [102]. Thus, various inks with cell and protein content were reported to be viably jettable using thermal inkjet printers [8]. By analogy, my laser-assisted system could potentially be viable for sensitive bio-inks at high operating frequencies. This issue was not investigated in this thesis due to the low repetition rate of our laser (15 Hz).

4.5 Compact fiber-based drop-on-demand system

The current actuation of the drop-on-demand device is based on focusing a laser pulse on the side of the microcapillary with a microscope objective (see Fig. 4.2(b)).

Focusing light through thin multimode fibers ($\varnothing 100 \mu\text{m}$) was demonstrated in several groups [44, 103] using phase control systems, as spatial light modulators. To further compact the drop-on-demand tool, I envision to employ this digital light focusing method through a multimode fiber enclosed in the microcapillary (see Fig. 4.8(a)).

Furthermore, engineering the input laser wavefront could allow simultaneously generating multiple focal spots through the multimode fiber, thus structuring the shape of the induced sum of shockwaves [104]. This approach could intensify the flow focusing effect and lead to the production of smaller droplets (see Fig. 4.8(b)).

Such digital light focusing techniques are implemented and further described in this thesis to build three-dimensional microstructures through a $\varnothing 70\text{--}100 \mu\text{m}$ fiber (see chapter 6).

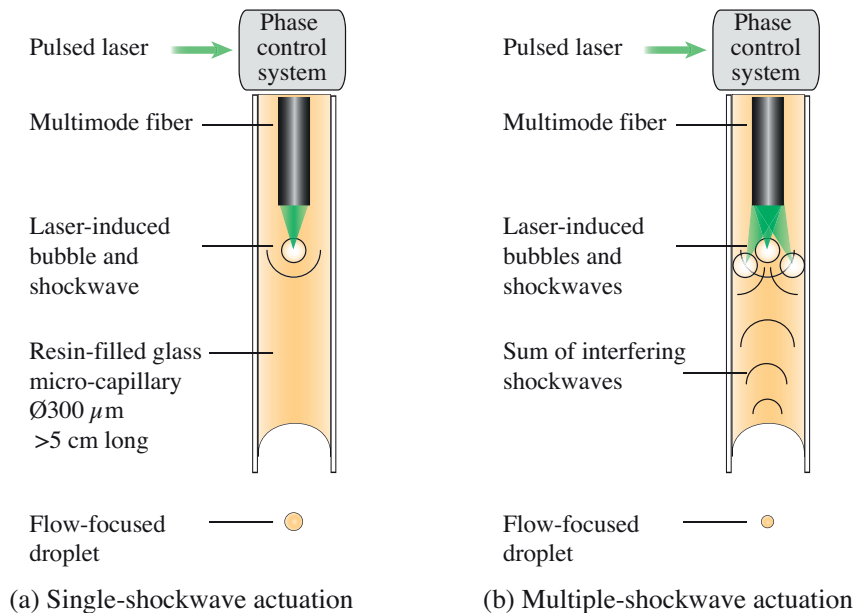


Figure 4.8 – Envisioned compact drop-on-demand device based on laser-actuation through a multimode optical fiber

4.6 Conclusion

In this chapter, I demonstrated that the range of printable inks of conventional inkjet printers can be broadened by generating viscous microdroplets through a 300- μm thin microcapillary using a laser-induced flow focusing phenomenon. The experimental results show that viscous microdrops (2-200 mPa s) can be generated with a sub-nozzle resolution, which could circumvent the nozzle clogging limitation of existing inkjet printers.

The current drop-on-demand device constitutes the basis of the first component of my compact toolkit for high-resolution additive manufacturing. This tool could be made more compact using digital light focusing through a multimode fiber, as implemented in the compact curing probe, the second component of my compact toolkit. This fiber-based curing probe is studied in chapters 5-6.

5 Single-photon non-linear photopolymerization

This chapter presents the chemical phenomenon exploited in the second component of my compact toolkit for high-resolution additive manufacturing: single-photon non-linear photopolymerization.

I first introduce the concept of free-radical chain photopolymerization and then review the literature on micro-additive manufacturing techniques to motivate the use of single-photon photopolymerization. I show that free-radical scavenging, induced by oxygen inhibition, can be used to generate a non-linearity in the photopolymerization dynamics of an off-the-shelf photoresist. Finally, methods to perform a live measurement of photopolymerization kinetics are discussed.

Some of the material presented in this chapter can be found in the following paper:

- Paul Delrot, Damien Loterie, Demetri Psaltis, and Christophe Moser. Single-photon three-dimensional microfabrication through a multimode optical fiber. *Optics Express*, 26(2):1766:1778, January 2018.

5.1 Introduction and motivation

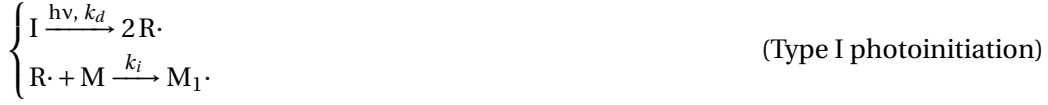
5.1.1 Free-radical chain photopolymerization

Three-dimensional microfabrication is an enabling technology that allows, for instance, the study of interactions at the cellular level [20, 26] by mimicking biological micro-architectures, or to manipulate light by building photonic microstructures [10–12].

A way to generate such microstructures is to selectively cure a liquid photosensitive material [36]. This is usually achieved through radical chain photopolymerization, which consists of three steps: *photoinitiation*, *propagation* and *termination* [105, 106]. In the photoinitiation step, an initiating molecule I is first photocleaved to generally yield two radicals $R\cdot$. These radicals then react with a first polymer precursor molecule M , which can be a monomer or a

Chapter 5. Single-photon non-linear photopolymerization

short polymer, to start chain growth with the chain-initiating radical $M_1\cdot$:



This reactive pathway corresponds to type I photoinitiation. On the other hand, in type II photoinitiation, the initiating molecule I requires a co-initiator molecule C to produce initiating radicals $R\cdot$:



Following the production of a chain-initiating radical $M_1\cdot$ by type I or type II photoinitiation, the polymer chain is grown by successive additions of polymer precursors M to the existing chain radical $M_n\cdot$, thus creating a longer chain radical $M_{n+1}\cdot$. This is the propagation step:



Polymer growth terminates through the reaction of two chain radicals $M_n\cdot$ and $M_m\cdot$ to yield either a coupled inactivated polymer chain M_{n+m} or two inactivated polymer chains M_n and M_m . This is the termination step:



Solidification, or gelation, of the polymer occurs through crosslinking of the growing polymer chains that forms an "infinite" polymer network (see Fig. 5.1(a)). Flory [107] showed that solidification statistically takes place when a threshold quantity of the polymer precursor is converted into polymer chains, this is the gelation threshold γ_c :

$$\gamma_c = \frac{1}{f-1} \quad (5.1)$$

where f is the number of polymerizable groups, or functionality, of the polymer precursor M . For instance, trimethylolpropane triacrylate, a polymer precursor used in this thesis has 6 functional groups, it thus gels when a 20%-conversion is reached.

After photopolymerization, the structure is developed with a solvent and only the voxels where the conversion overcame the gelation threshold will remain insoluble (see Fig. 5.1(b)). This

threshold also allows refining the size of the polymerized features by varying the exposure time of the polymer, as shown in Fig. 5.1(b) assuming a Gaussian profile of illumination.

Using this photopolymerization process, one can sequentially cure layers or voxels of a photoresist to form solid three-dimensional microstructures.

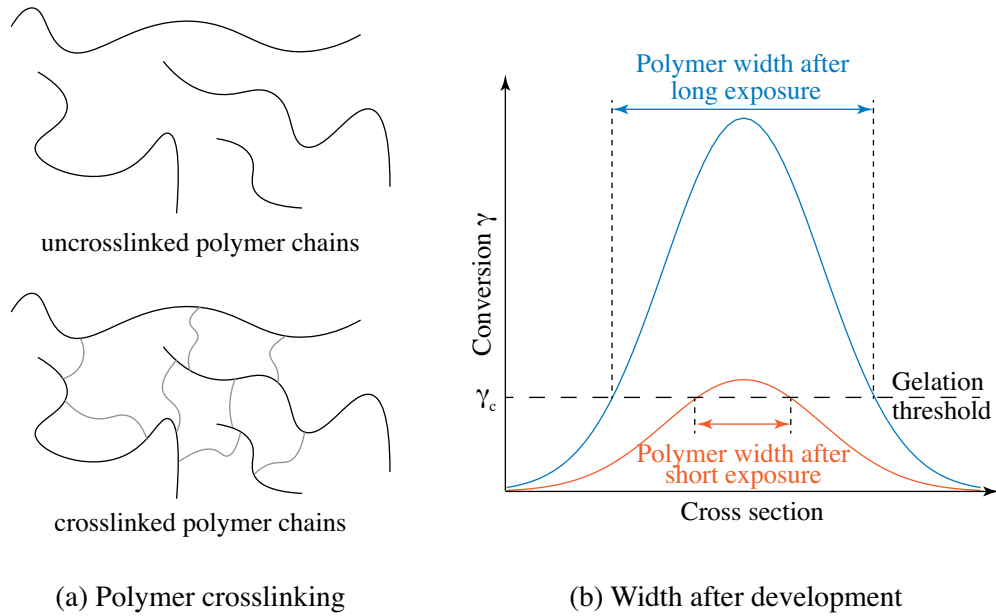


Figure 5.1 – Polymer gelation

5.1.2 Optimal three-dimensional microfabrication

The fabrication of these microstructures is best achieved without moving elements inside the build volume, as would occur in microstereolithography [108] for instance (see Fig. 5.2(a)), since these moving parts can distort the end product and decrease the axial printing resolution [36].

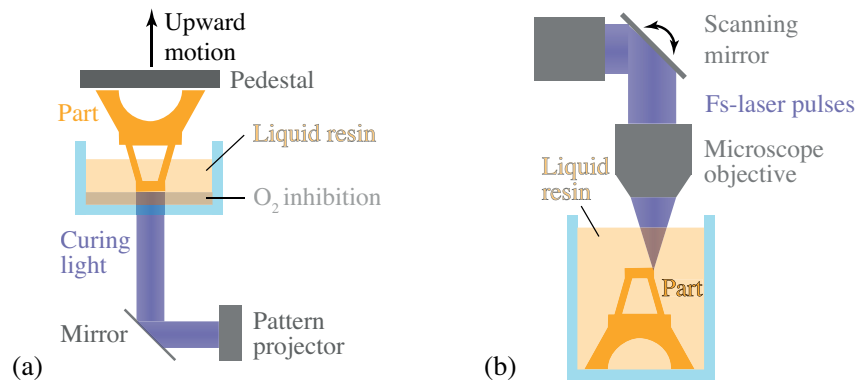


Figure 5.2 – (a) Micro-stereolithography and (b) direct laser writing

Hence, an optimal fabrication method consists in directly writing the solid three-dimensional microstructure deep into a liquid material. For a laser direct writing system, such a manufacturing method requires the ability to confine photopolymerization to a local voxel of material deep into a liquid photoresist (see Fig. 5.2(b)).

This confinement cannot be achieved with a purely linear photopolymerization process, such as the combination of single-photon absorption with a linear photoresist behavior [109, 110]. In this case, the accumulation of absorbed dose, and therefore the cumulative curing of the photoresist prevents axial features to be resolved. To illustrate this, I simulated the sequential laser scanning of two lines deep into a weakly-absorbing photoresist, to neglect the attenuation of the beam (see cross-section images in Fig. 5.3). The gelation threshold was arbitrarily defined to an absorbed dose (see brownish color in Fig. 5.3) so that the axial curing induced by one laser spot is much smaller than the axial separation of the two lines we intend to cure within the photoresist (see solid black lines in Fig. 5.3). As the lines are being scanned, the accumulation of dose creates a thick block of polymer instead of two resolved lines (see image on the right-hand side in Fig. 5.3).

This cumulative crosstalk induced by linear photopolymerization can be reduced by using a proximity-effect correction algorithm [111] to account for the exposure of each part of the microstructure by the other exposed layers, as discussed in chapter 6. On the other hand, in this chapter I show that the selective curing of a voxel of material can also be achieved by inducing a non-linearity in the photopolymerization process, either in the photoresist dose response or in the laser beam absorption.

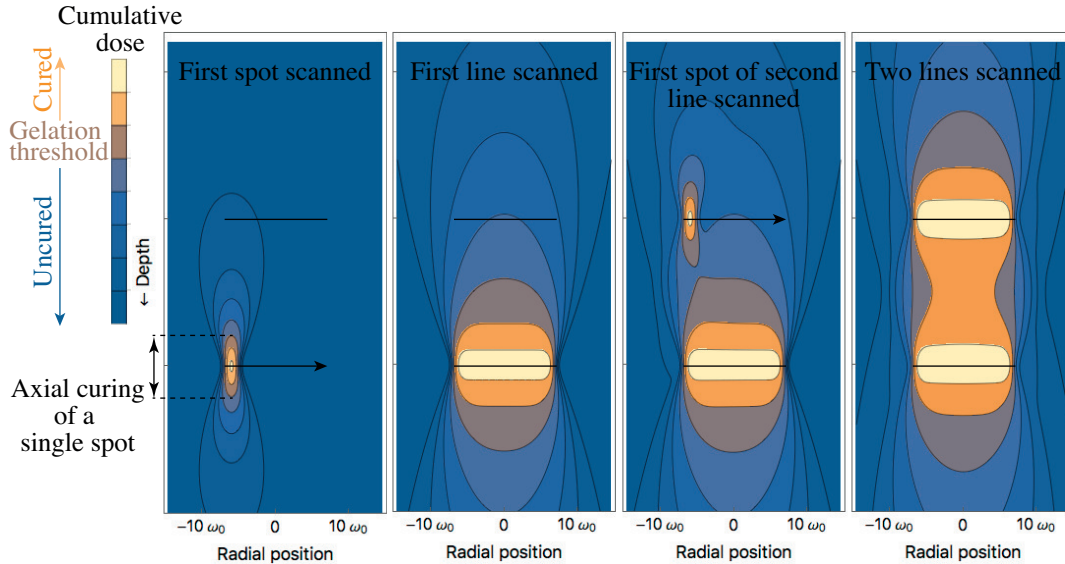


Figure 5.3 – Cumulative curing when scanning two lines deep into a photoresist with a linear photopolymerization process.

5.1.3 Two-photon photopolymerization

Non-linear absorption is implemented in two-photon photopolymerization (TPP), which was first introduced in 1997 by Maruo et al. [112] and has become the technique of choice for producing three-dimensional microstructures [113]. In TPP, a photo-initiating molecule is activated upon simultaneous absorption of two photons [114, 115], as opposed to single-photon absorption, see respectively in Fig. 5.4(a) the red and blue arrows. The resulting activated photo-initiating molecule then proceeds to a reactive triplet state and produces a radical $R\cdot$ that initiates polymer chain growth of $M_n\cdot$. Owing to the extremely small two-photon absorption cross-section of photo-initiating molecules ($10^2\text{-}10^3 \cdot 10^{-50} \text{cm}^4 \text{s photon}^{-1}$), which encompasses the limited lifetime ($10^{-15}\text{-}10^{-16} \text{s}$) of their excited state after the first photon is absorbed [116], TPP is confined to voxels where there is both a high photon flux density and an intense photon flux [117]. Typically, in most TPP systems, such conditions for non-linear absorption are met by focusing femtosecond laser pulses with high numerical aperture (NA) objectives. Though TPP systems can achieve a linewidth resolution of 80 nm [118], the complexity and cost of femtosecond lasers limit the integration of these printing systems within other manufacturing platforms and lessen their affordability.

To overcome these limitations and provide a compact and affordable alternative to TPP systems, I investigated alternative non-linear photopolymerization processes that could be implemented through a multimode fiber and with an inexpensive continuous-wave laser, which constitutes the second part of my compact toolkit for high-resolution additive manufacturing.

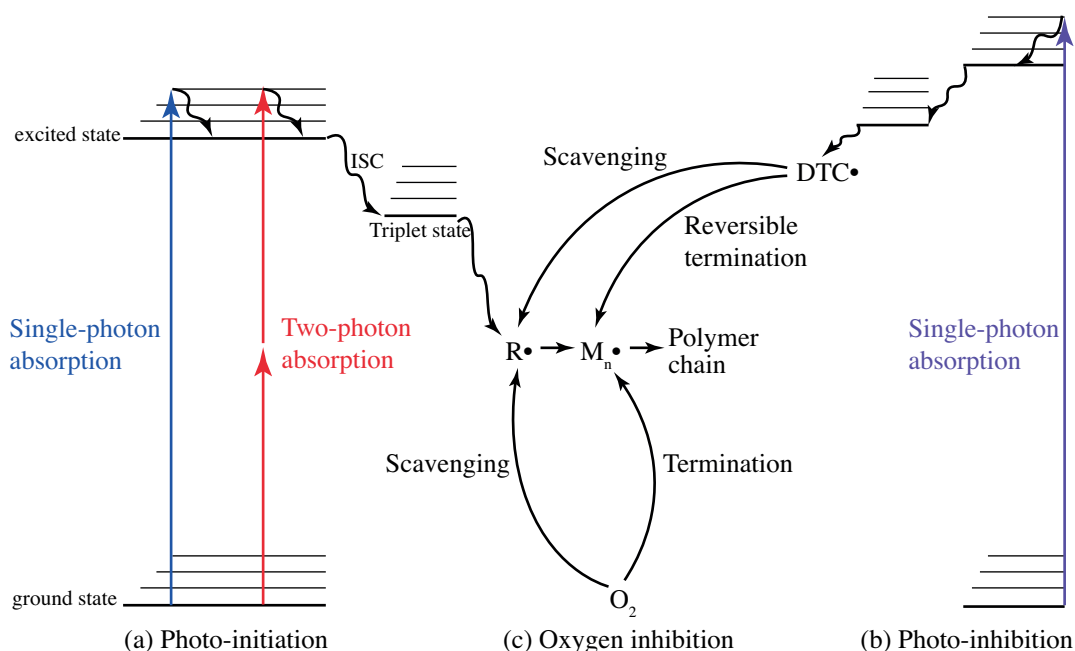


Figure 5.4 – Reactive pathways for polymerization photo-initiation, photo-inhibition and oxygen inhibition.

5.1.4 Alternative non-linear photopolymerization processes

The implementation complexity of TPP has oriented research towards alternative non-linear photopolymerization processes.

Two-color photo-initiation photo-inhibition polymerization

Scott et al. [119, 120] investigated the lateral spatial confinement of polymerization using a two-color photo-initiation photo-inhibition scheme in which a second continuous-wave laser (see violet arrow in Fig. 5.4(b)) generates dithiocarbamyl radicals $DTC\cdot$ that can either scavenge the free-radicals $R\cdot$ generated by the photo-initiating continuous-wave laser wavelength (see blue arrow in Fig. 5.4(a)), or reversibly terminate polymer growth. The authors did not explore axial spatial confinement of polymerization but suggested the use of an inhibiting “bottle beam” [121] to achieve it. Recent progress in designing an efficient non-linear photo-inhibitor [122] could open up this possibility.

High-intensity continuous-wave polymerization

Alternatively, several groups have recently demonstrated three-dimensional microfabrication deep into a photoresist through pointwise scanning of a highly-focused continuous-wave (CW) laser beam [109, 123–127]. The mechanisms behind this spatially confined photopolymerization process are still unclear: the authors respectively suggested a non-linear dose response of the photoresist [109], a possible photolysis of organic bonds [123] or an ultra-low single-photon absorption combined with photothermal effects [124, 125, 128]. Though simpler and more affordable than TPP, this direct writing technique still requires the generation of intensities as high as $\sim 10^7 \text{W.cm}^{-2}$ to reach the polymerization threshold. As reported by several authors [109, 123, 129], such intensity levels can result in erratic microexplosions in the material, thus reducing the printing dynamic range and damaging the printed microstructure and its vicinity.

Single-photon polymerization with oxygen inhibition

Another approach to induce a non-linear photopolymerization behavior consists in the combination of single-photon absorption and a non-linear dose response of the photoresist.

Oxygen, as a strong radical scavenger [105], inhibits photopolymerization through scavenging of free radicals $R\cdot$ or termination of chain radicals $M_n\cdot$ (see Fig. 5.4(c)), which can be described by the following reaction equations:



Oxygen inhibition is used to create a so-called "dead-zone" of polymerization for continuous liquid interface production [29]. In these inhibited zones of polymerization, the rate of radical photogeneration is lower than the rate of radical scavenging by oxygen and no polymerization takes place even after long exposures. On the other hand, in regions exposed to a higher intensity, a similar dose will result in polymerization since the rate of radical photogeneration will overcome the scavenging threshold.

Similarly, this phenomenon can be exploited to inhibit off-focal photopolymerization and selectively cure a voxel of material deep within a photopolymer with a CW laser source. This is evidenced by the simulation results of Fig. 5.5, whose model and parameters are further described in Appendix A. These simulations, performed for the experimental conditions of my intended microfabrication device (see Fig. 5.5(a)), show that oxygen inhibition (see dashed curves with O_2 in Fig. 5.5(b)) induces a non-linear axial polymerization growth that can potentially remove off-focal photopolymerization. This is supported by the comparison of the cross-sections views and solid and dashed red curves in Fig. 5.5 where an oxygen-inhibited photopolymerization yields an asymptotic axial polymer growth (see dashed red curve in Fig. 5.5(b)) whereas a non-inhibited photopolymerization process for the same 200-nW optical power results in a linear axial growth over time (see solid red curve in Fig. 5.5(b)). Below a threshold power of 100 nW, oxygen radical scavenging even prevents any photopolymerization (see blue dashed curve in Fig. 5.5(b)).

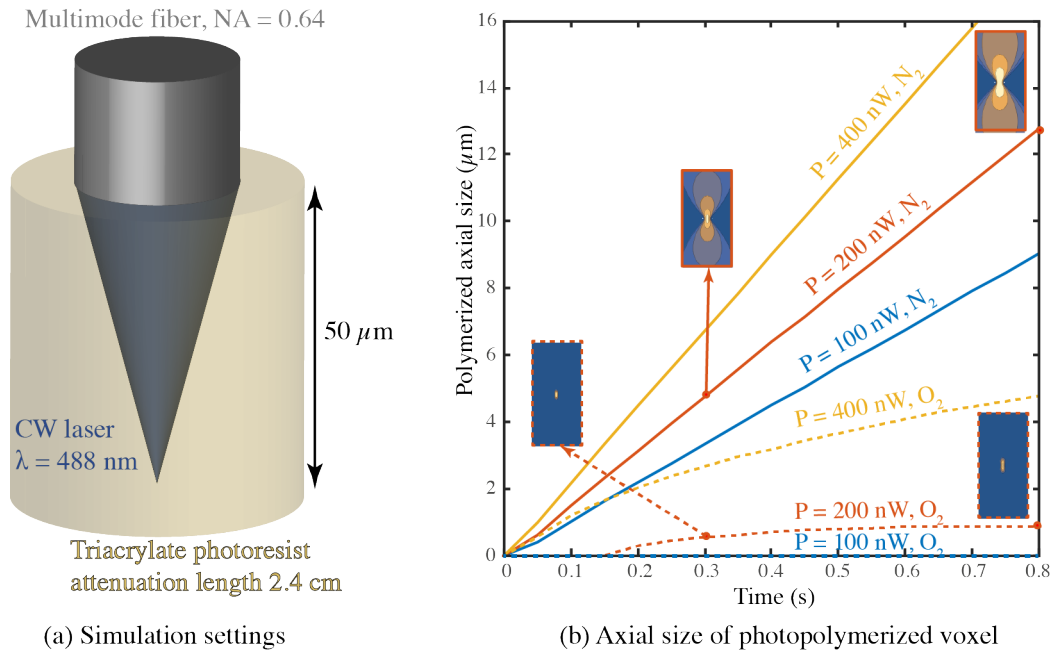


Figure 5.5 – Simulation of the effect of oxygen inhibition on the photopolymerization extent of a voxel produced 50- μm deep into our photoresist. N_2 : without oxygen inhibition, O_2 : with oxygen inhibition. Further information on the simulation model can be found in Appendix A

Maruo et al. [126] took advantage of this non-linear dose response to build three-dimensional microstructures through single-photon polymerization. This was achieved by focusing a CW laser with a 1.0-NA microscope objective to confine photopolymerization to the focal volume without suffering from the cumulative dose effect in the surrounding "dead-zones". With this method, intensities of 10^{-1}W.cm^{-2} , less harmful to materials than high-intensity CW polymerization, and off-the-shelf photo-initiators can be employed.

To build the curing probe of my high-resolution additive manufacturing toolkit, I used the same non-linear photopolymerization phenomenon through a thin multimode optical fiber ($\varnothing 70 \mu\text{m}$, NA 0.64) with the aim of providing a compact and affordable alternative to TPP systems.

In this chapter, I investigate the kinetics of single-photon photopolymerization and show that oxygen inhibition can be exploited to induce a non-linearity in the photopolymerization of an off-the-shelf photoresist. In chapter 6, I combine this non-linearity with a specific curing method to achieve three-dimensional microfabrication of solid and hollow microstructures by digitally focusing and scanning CW laser light through a multimode fiber.

5.2 Photopolymerization kinetics

To optimally exploit oxygen inhibition as a means of controlling the axial extent of single-photon polymerization, the non-linear gelation threshold of the photoresist was calibrated for different exposure times and writing powers, with and without oxygen.

5.2.1 Calibration methods

The selective curing of a voxel of material for true three-dimensional microfabrication requires inducing a non-linearity in the photopolymerization process, either in the photoresist dose response or in the laser beam absorption.

The intensity attenuation of a light beam undergoing a N -photon absorption process in a material can be generally expressed as:

$$\frac{dI(z)}{dz} = -\alpha \cdot I(z)^N \quad (5.2)$$

where $I(z)$ is the intensity of the light beam propagating along the z -axis and α is the N -photon absorption coefficient of the material [115].

Similarly, the effective non-linearity or linearity of CW-induced photopolymerization can be determined by measuring the exponent N of the relationship between the exposure dose D , the threshold power for photopolymerization P_{th} and the exposure time Δt [36, 109, 123, 129, 130]:

$$D \propto \Delta t \cdot P_{th}^N \quad (5.3)$$

Rewriting this relationship to show the trend of the threshold gelation dose D in a parametric space of threshold power versus exposure time:

$$P_{th} \propto \Delta t^{-1/N} \quad (5.4)$$

we infer that the non-linearity exponent N can be measured by varying the photoresist exposure time Δt and determining the associated threshold power for polymerization P_{th} [123].

The photoresist used in this chapter and chapter 6 was made of off-the-shelf chemical components: an organic polymer precursor trimethylolpropane triacrylate (TMPTA; >70%, Aldrich, USA), 1wt% of the Norrish type II photoinitiator (see section 5.1.1) camphorquinone (CQ; 97%, Aldrich, USA) and 0.5wt% of the synergist ethyl 4-(dimethylamino)benzoate (EDAB; 97%, Aldrich, USA).

To calibrate the photoresist's photopolymerization kinetics, I experimentally implemented the calibration method described above by focusing CW laser light at 488 nm into a droplet of photoresist deposited onto a plasma-cleaned glass slide (see left-hand side illustration in Fig. 6.2). The impact of oxygen on the photopolymerization threshold was measured by imaging the induced polymer spots with a DIC-microscope (see right-hand side measurement picture in Fig. 6.2). Prior to the experiment, the photoresist was either bubbled with O_2 and the droplet was let to reach gas equilibrium onto the glass slide for a few minutes, or the photoresist was bubbled with N_2 and enclosed between a glass slide and a coverslip. Laser light was focused in an inverted configuration through a microscope objective matching the numerical aperture of the multimode fiber we use in chapter 6 and reflections at the air-glass interface were taken into account. The same measurement was then performed with the multimode fiber setup (see chapter 6) for the oxygen-bubbled configuration and exhibited consistent results.

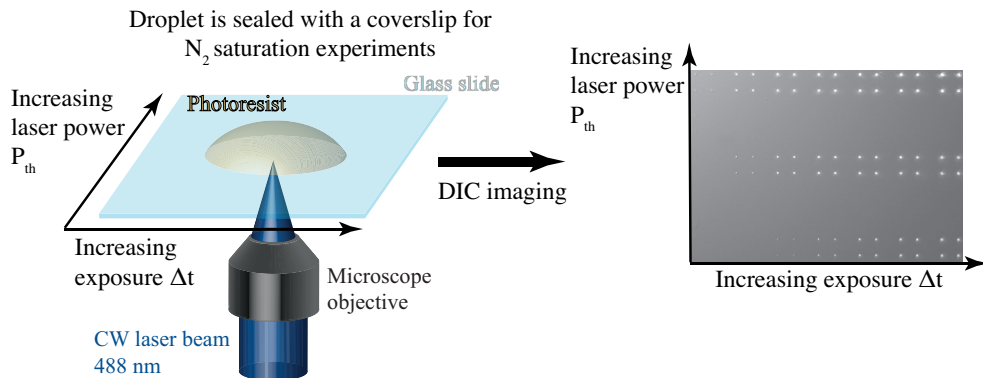


Figure 5.6 – Experimental procedure for the measurement of the photopolymerization non-linearity.

5.2.2 Single-photon non-linear photopolymerization

The calibration of the photopolymerization threshold clearly reveals a non-linear photopolymerization behavior for both the oxygen- and nitrogen-bubbled photoresists (see Fig. 5.7(a)) as the measured photopolymerization thresholds do not follow an isodose trend (see dashed lines in Fig. 5.7(a)), typical of a linear photopolymerization process. For the oxygen-bubbled photoresist, which is used for three-dimensional microfabrication, we find the non-linearity exponent to be $N_{O_2} = 3.36 \pm 0.21$ with a power-law fit on the data points with exposure time below 2 seconds. This value is similar to that obtained by Mueller et al. [130] with 7-diethylamino-3-thenoylcoumarin (DETC) and isopropylthioxanthone (ITX) photoinitiators. For exposure times longer than 2 s, the data points deviate from the power-law fit for both the oxygen- and nitrogen-bubbled photoresists, likely due to oxygen diffusion and photoinitiator depletion [130]. This deviation also evidences that bubbling the photoresist with nitrogen did not remove all the oxygen content, which might also account for the high non-linearity of the nitrogen-bubbled photoresist $N_{N_2} = 2.41 \pm 0.36$. The non-linearities measured here would likely turn towards $N = 1$, that is to say a linear photoresist behavior, for sufficiently small exposure times, where diffusion effects are too slow to quench photopolymerization.

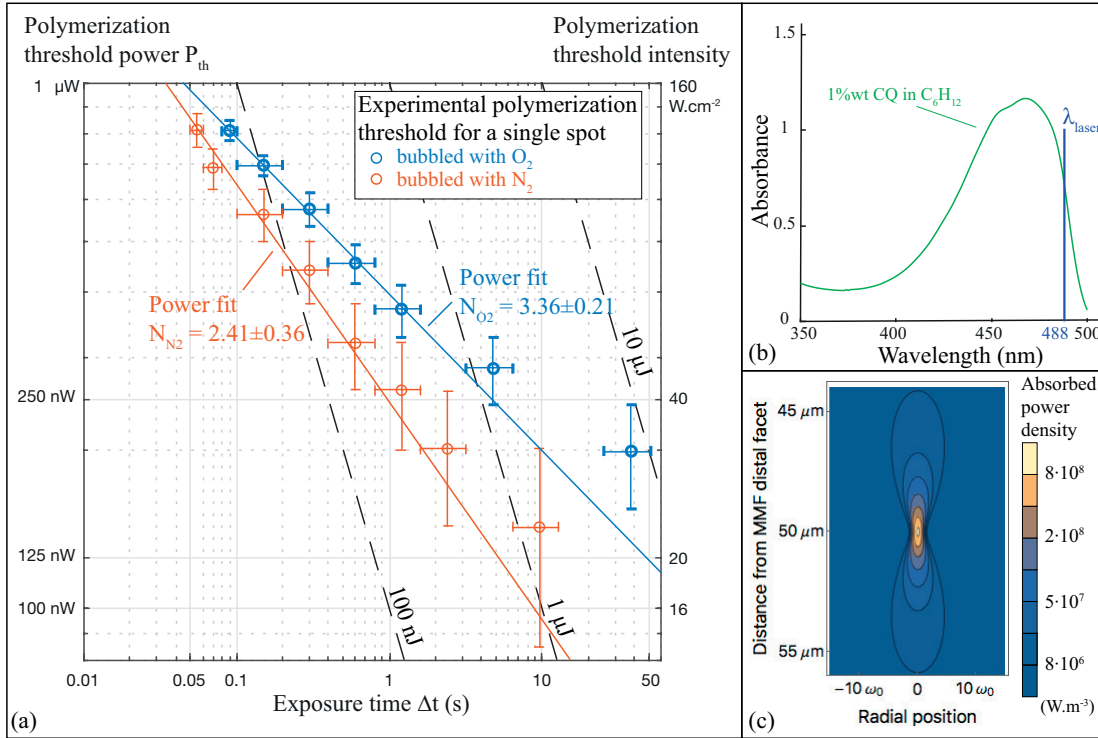


Figure 5.7 – (a) Polymerization threshold power of a single polymer spot versus the spot exposure time, the dashed lines are isodose lines (b) Absorption spectrum of camphorquinone (CQ) in C_6H_{12} ($l = 0.4$ cm) (c) Simulation of the beam propagation and absorption within the photoresist. The beam is focused 50 μ m below the multimode fiber.

Previous works reported on a similar non-linear photopolymerization behavior induced by CW laser light [109, 123–125, 128]. The authors speculated that the non-linearity stemmed from an ultra-low single-photon absorption [109, 124] as well as the photolysis of organic bonds [123], or single-photon photopolymerization inhibited by oxygen radical scavenging [126]. As to the non-linearity evidenced in my experiments, the used intensity level and the absorbance of the photoresist unambiguously rule out a non-linear absorption phenomenon, a photolysis of organic bonds and an ultra-low single-photon absorption phenomenon. Indeed, the laser intensities I used experimentally, $\sim 10^1\text{--}10^2\text{ W.cm}^{-2}$ (see Fig. 5.7(a)), are too low by several orders of magnitude to induce multiphoton absorption or avalanche ionization $\sim 10^{12}\text{ W.cm}^{-2}$ [117, 131], or to induce the photolysis of organic bonds $\sim 10^7\text{ W.cm}^{-2}$ [123]. In addition, as the name indicates, ultra-low single-photon absorption was performed with weak absorption conditions, for instance the absorbance is $A = 0.0072$ in the work of Do et al. [124], whereas my experiments are performed with a significant single-photon absorption (see Fig. 5.7(b)), which accounts for a 2.1% decrease of intensity after a $50\text{-}\mu\text{m}$ propagation within our photoresist. Moreover, photo-thermal effects at the focus can be ruled out as Tong et al. [128] showed that an absorbed light density of $\sim 10^{15}\text{ W.m}^{-3}$ is required to bring a photoresist to a temperature of 150°C , whereas the light density absorbed at focus is more than six orders of magnitude lower in my experiments (see Fig. 5.7(c)).

Hence, I speculate that the observed non-linear photopolymerization behavior results from a combination of single-photon absorption and a non-linearity of the photoresist, such as the one induced by oxygen radical scavenging. This hypothesis is supported by the lower non-linearity $N_{N_2} = 2.41 \pm 0.36$ measured with a nitrogen-bubbled photoresist (see Fig. 5.7(a)) and the low intensity level $\sim 10^{-1}\text{--}10^0\text{ W.cm}^{-2}$, close to mine, used by Maruo et al. in their seminal work on single-photon photopolymerization inhibited by oxygen radical scavenging [126].

The propagation and absorption of the laser beam from the distal facet of the multimode fiber to a focal spot $50\mu\text{m}$ deep into the photoresist are simulated (see Fig. 5.7(c)) and indicate more than a 100-fold contrast between the focus and regions $5\mu\text{m}$ off-focus. The combination of this high contrast with the non-linear photopolymerization threshold depicted in Fig. 5.7(a) suggests that off-focal photopolymerization can potentially be removed by illuminating the photoresist so that only the focal volume reaches the photopolymerization threshold. This is discussed in chapter 6, in which this phenomenon is exploited to build three-dimensional microstructures through a multimode fiber.

5.2.3 Time-resolved measurement of photopolymerization kinetics

The measurement setup of the photopolymerization threshold described in section 5.2.1 is not optimal. Though the impact of oxygen on the gelation threshold (see Fig. 5.7(a)) could be determined, I experimentally observed that the DIC microscope imaging of the samples quickly polymerizes the whole photoresist volume and degrades the quality of measurement. To better understand the non-linearity observed when the photoresist is bubbled with nitrogen,

Chapter 5. Single-photon non-linear photopolymerization

as well as to study the relative impact of camphorquinone and its co-initiator on the non-linear photopolymerization of TMPTA, a finer measurement of photopolymerization kinetics would be needed. Hence, I investigated the possibility to perform a live and time-resolved measurement of photopolymerization kinetics, as opposed to the *a posteriori* and discrete measurements used in sections 5.2.1-5.2.2. These time-resolved measurement setups of photopolymerization are discussed in the next two sub-sections.

Scattering detection of the photopolymerization onset

In order to obtain a better time resolution of the onset of photopolymerization as a function of the spot power than the one determined in Fig. 5.7(a), I implemented on our setup a measurement method based on the work of Engelhardt et al. [132] and Mueller et al. [130].

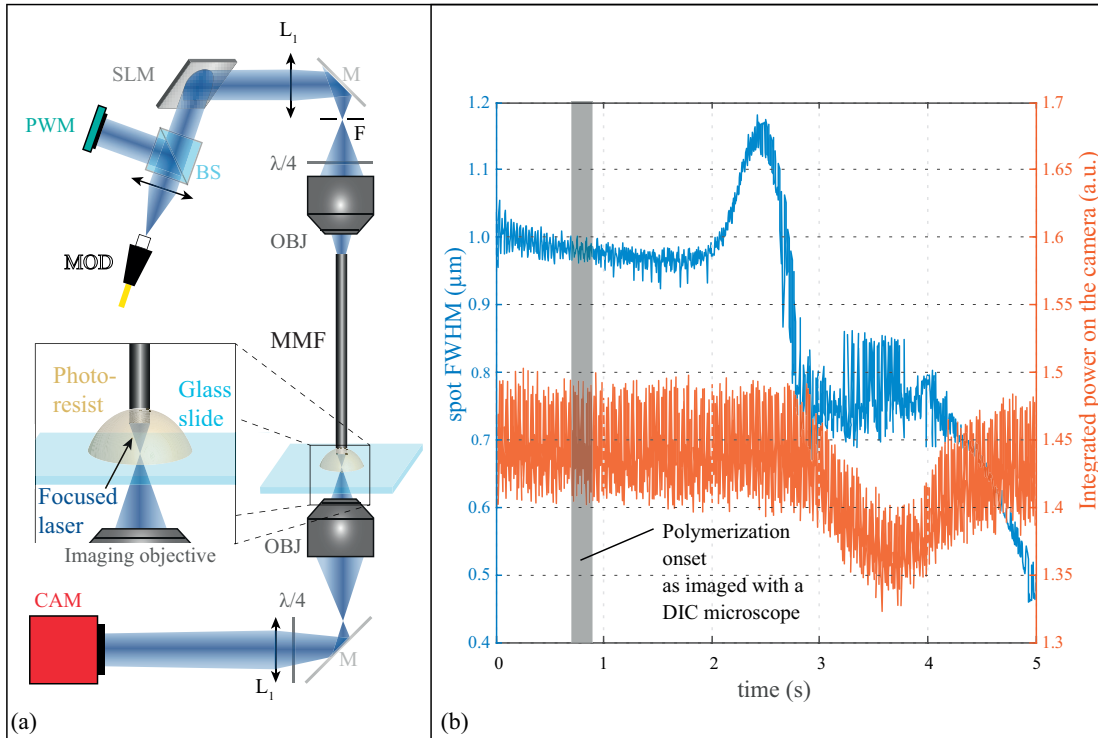


Figure 5.8 – (a) Experimental setup for time-resolved measurement of the photopolymerization threshold. Light is focused through the multimode fiber into a droplet of photoresist, and the resulting focused spot is imaged on a camera as photopolymerization occurs. MOD: single-mode fiber, PWM: power-meter, BS: non-polarizing beam-splitter, SLM: spatial light modulator, L_1 : lens, ($f=175$ mm), M: mirror, F: filtering diaphragm, $\lambda/4$: quarter wave-plate, OBJ: microscope objective (NA 0.8, 100x, Zeiss), MMF: multimode optical fiber (GOF85, NA 0.64, $\varnothing 70$ μm , Schott), CAM: camera (b) Time-resolved measurement of the photopolymerization threshold for a spot power of 352 ± 3 nW. The FWHM of the laser spot generated through the MMF is plotted over time (in blue, see left vertical axis), as well as the relative integrated power on the camera (in orange, see right vertical axis).

As shown in Fig. 5.8(a), the micro-additive manufacturing setup presented in chapter 6 was adapted so that the laser spot generated into the photoresist at the level of the glass substrate is directly imaged onto a camera (*CAM*). According to previous studies [130, 132], the onset of polymerization locally modifies the refractive index of the polymer, thus leading to scattering of the laser used to induce photopolymerization [132] or of another light probe [130].

Using the setup of Fig. 5.8(a), both the power integrated on the camera and the measured spot FWHM are monitored over time while photopolymerization occurs. However, a significant change of these signals that would evidence the onset of photopolymerization is not measured before time $t \sim 2s$ (see the blue curve in Fig. 5.8(b)), whereas DIC imaging of polymer spots generated with the same spot power showed that photopolymerization occurs within $0.8 \pm 0.1s$ (see the gray area in Fig. 5.8(b)). The measurement setup of Fig. 5.8(a) therefore over-estimates the time necessary for the onset of photopolymerization. Mueller et al. [130] calculated that the relative scattering signal induced by the voxel onset is of the order of a few percents, to which our measurement setup might not be sensitive.

Holographic detection of the photopolymerization onset

To overcome the sensitivity limitation of scattering detection, we are currently studying the possibility to measure the refractive index changes induced by polymerization using off-axis holography [133]. This study is a collaboration with my colleague Dr. Damien Loterie and Nathanaël Restori, an EPFL master student.

Briefly, as shown in Fig. 5.9(a), a photoresist sample sandwiched between two glass slides is made to polymerize locally by a blue laser light focused through a microscope objective *OBJ*. In parallel, a red laser beam, to which the photopolymer is not sensitive, is split into two components by a beamsplitter *BS1*: a reference beam and a probe beam. Thanks to a dichroic mirror *DM*, the probe beam follows the same optical path as the polymerizing beam. However, it is not focused on the sample but rather collimated so that refractive index changes within the photoresist sample modifies its wavefront. The probe beam is then recombined with the off-axis reference beam using the beamsplitter *BS2* and the two beams are made to interfere on the camera *CAM*.

The resulting interferometric fringes, which constitutes a hologram, are then imaged on the camera (see Fig. 5.9(b)) and allows retrieving the phase profile of the sample (see Fig. 5.5(c)). Providing that the probe laser source is noise-free, this type of interferometric measurement allows achieving nanometric height resolution [134], which corresponds to a refractive index change $\Delta n = 10^{-3}$ over a distance of $1 \mu m$, a resolution one order of magnitude better than the refractive index change of a monomer to a polymer.

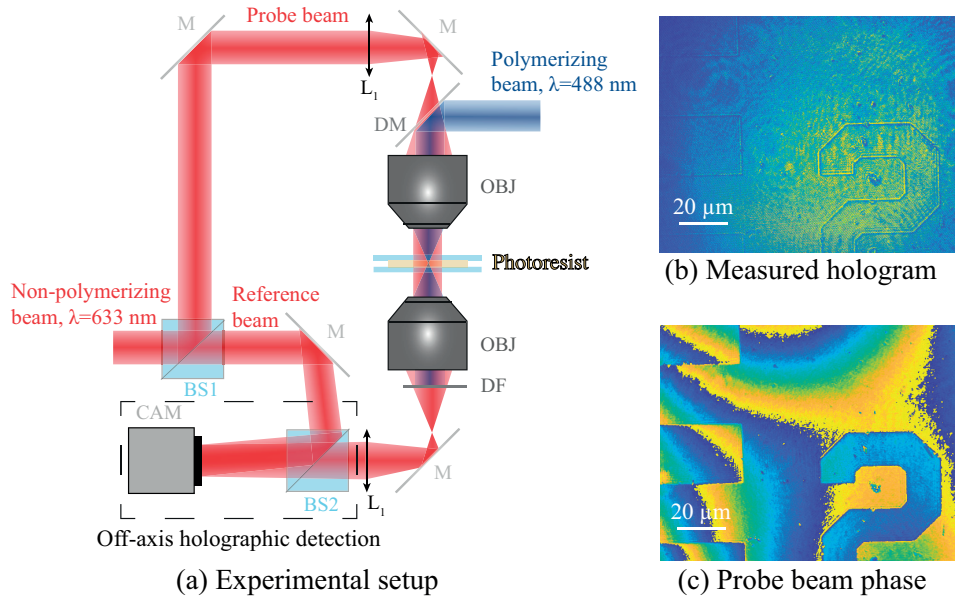


Figure 5.9 – (a) Experimental setup for time-resolved measurement of the photopolymerization threshold using off-axis holography. BS: non-polarizing beam-splitter, L_1 : relay lens, M:mirror, DM: dichroic mirror, DF: dichroic filter, OBJ: microscope objective (NA 0.8, 100x, Zeiss), CAM:camera.

5.3 Conclusion

As shown in this chapter, oxygen inhibition combined with single-photon absorption can generate a non-linear photopolymerization process, which we plan to further study with an optimized characterization setup. Analyzing the photopolymerization kinetics of the photoresist reveals that an inexpensive continuous-wave laser can potentially be employed to selectively cure a voxel of material without off-focal polymerization. To implement a compact and affordable alternative to current microfabrication setups, which are based on complex and expensive pulsed lasers, I implement this photopolymerization process through a multimode fiber for three-dimensional microfabrication, as discussed in the next chapter.

6 Three-dimensional microfabrication through a multimode fiber

In this chapter, the non-linear polymerization process presented in chapter 5, single-photon non-linear photopolymerization, is used to build three-dimensional microstructures through an ultra-thin multimode fiber, which constitutes the second part of my compact toolkit for high-resolution additive manufacturing.

I first introduce the challenges of image transmission through multimode fibers and then present the transmission matrix method that allows digitally scanning light through a multimode fiber. I show that optimal three-dimensional microfabrication through a multimode fiber requires a specific curing strategy and investigate the limitations of this compact printing device. Finally, proximity effect corrections algorithms are discussed, with the aim of improving the printing resolution of the compact microprinter.

Some of the material presented in this chapter can be found in the following paper:

- Paul Delrot, Damien Loterie, Demetri Psaltis, and Christophe Moser. Single-photon three-dimensional microfabrication through a multimode optical fiber. *Optics Express*, 26(2):1766:1778, January 2018.

6.1 Digital light scanning through a multimode fiber

6.1.1 Image transmission through multimode fibers

The integration of several printing techniques into a single platform requires to miniaturize each additive manufacturing tool. In the same way, *in vivo* micro-additive manufacturing would require minimally invasive tools to focus and scan light to cure photosensitive materials. Multimode fibers, which can be thinner than $100\text{ }\mu\text{m}$, have the potential to be used as compact optical elements for such applications.

Multimode fibers are indeed thin guiding media in which light is transmitted through total internal reflections that result from the higher refractive index of the core glass medium than

the cladding medium (see reflected rays in Fig. 6.1).

However, modal scrambling prevents image transmission through multimode fibers. Owing to the different propagation constants of the fiber's modes, an image supplied at the input of a fiber will be distorted as it travels through it; which eventually results in a scrambled speckle pattern at the output (see Fig. 6.1).

This limitation can be overcome since the effect of modal scrambling on image transmission is deterministic and can be compensated by measuring the multimode fiber's propagation characteristics [44, 135, 136], as discussed in the next section.

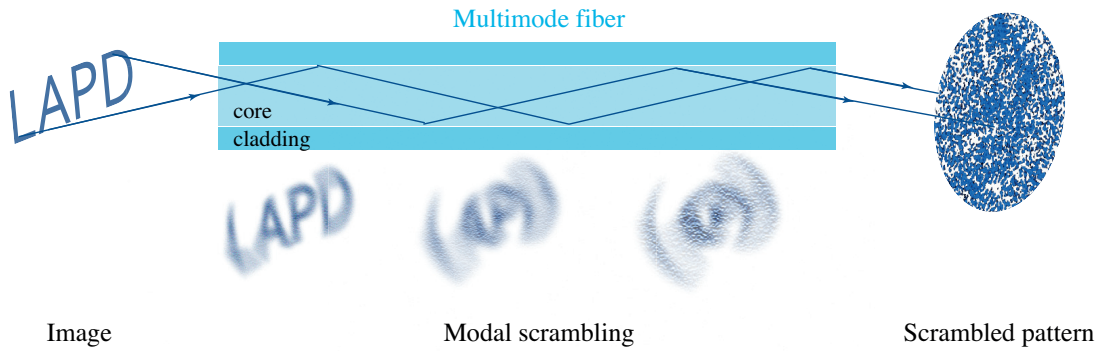


Figure 6.1 – Image transmission through a step-index multimode fiber

6.1.2 Calibration of the multimode fiber for the distal generation of focused laser spots

Since multimode fibers are scrambling media, the generation of focused laser spots through it requires a calibration step prior to each microfabrication experiment. This calibration step, which consists in the measurement of the fiber's transmission matrix, was developed by my colleague Dr. Damien Loterie during his PhD thesis [137, 138]. We then collaborated to build an upright version of his setup for three-dimensional microfabrication through multimode fibers.

The transmission matrix [139] of the multimode fiber is determined by measuring with off-axis holography the fiber's output response (on the distal side in Fig. 6.2(a)) to a series of independent plane waves that are fed to its input using wavefront shaping (on the proximal side in Fig. 6.2(a)).

In other words, a basis of independent plane waves is generated by a spatial light modulator (see SLM patterns in Fig. 6.2(b)), which corresponds to different input angles (or input vectors X in Fig. 6.2(b)) fed to the multimode fiber. Each of these input vectors results in a different scrambled speckle pattern, or output vector Y , at the fiber distal end. In this way, the scrambling transformation T applied to the input vector X to yield the output vector $Y = TX$

6.1. Digital light scanning through a multimode fiber

is determined. This transformation T is the fiber transmission matrix, and by numerically inverting this matrix to obtain T^{-1} , arbitrary output vectors Y , such as focused spots, can be generated by digitally producing the appropriate input wavefront $X = T^{-1}Y$.

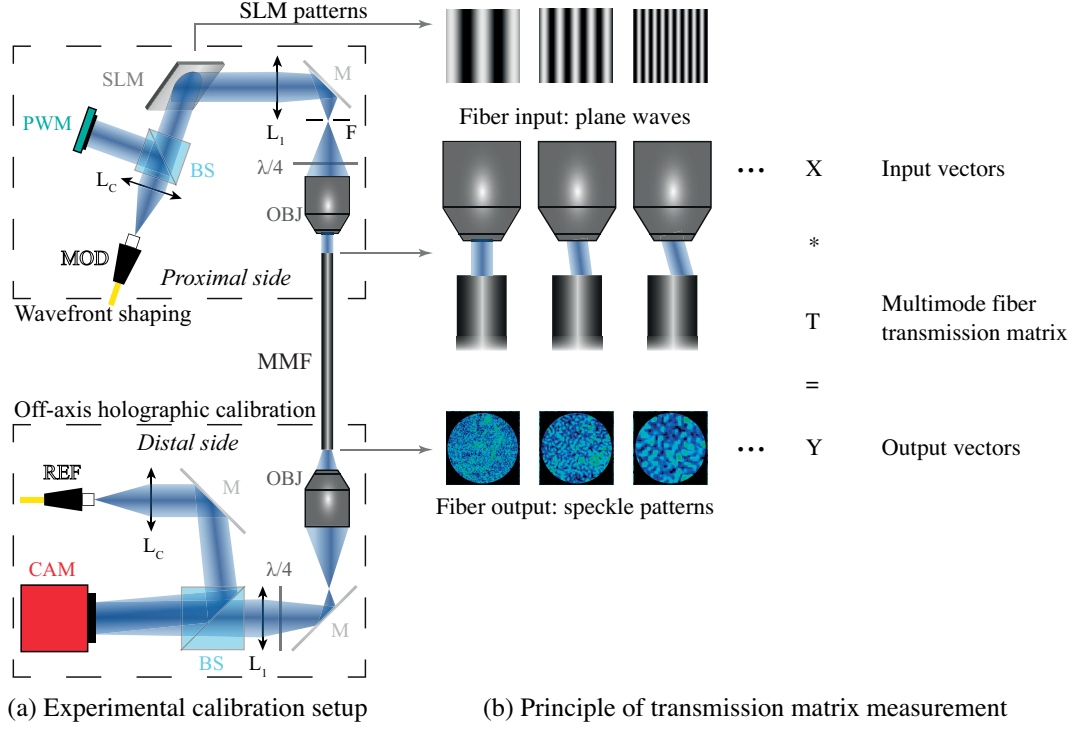


Figure 6.2 – Experimental setup for the calibration of the multimode fiber (MMF) prior to each microfabrication experiment. The MMF transmission matrix is determined by feeding a series of independent plane waves to its proximal side using wavefront shaping, the MMF's response to these inputs is measured on the distal side with off-axis holography

To measure the transmission matrix, CW laser light at 488 nm (Coherent, Sapphire 488 SF) is coupled into two polarization-maintaining single mode fibers *MOD* and *REF* with a 90:10 ratio (see Fig. 6.2(a)). The linearly-polarized *MOD* beam is collimated by a lens L_c ($f = 150$ mm) and modulated by a spatial light modulator (*SLM*; Pluto VIS, Holoeye). Half of the beam is sent to a powermeter *PWM* (Model 2936-C, Newport) through a 50:50 beamsplitter *BS* to monitor the beam power. The modulated beam is fed to the multimode optical fiber (*MMF*; GOF85, NA 0.64, $\varnothing 70 \mu\text{m}$, Schott), held in a syringe needle, through a 4-f system made of lens L_1 ($f = 175$ mm) and microscope objective *OBJ* (NA 0.8, 100x, Zeiss). The beam is further filtered by a pinhole *F* in the Fourier plane to retain only its modulated component. Because step-index fibers tend to preserve circular polarizations [103], the beam is circularly polarized with a quarter-wave plate $\lambda/4$ before being coupled to the fiber, and then set back to a linear polarization at the fiber output [103]. The resulting speckle pattern at the MMF distal side is combined with a tilted reference plane wave *REF* and imaged onto a camera *CAM*. Using this off-axis holographic system, we thus extract the amplitude and phase response of the MMF to a series of independent plane waves (which are points in the Fourier domain) to determine

the fiber's transmission matrix. Further details on this measurement can be found in previous works [45, 137].

6.1.3 Experimental setup for single-photon microfabrication

Following the calibration of the fiber's transmission matrix, focused CW laser spots can be generated ahead of the fiber's distal facet using the proximal wavefront shaping system.

The single-photon direct-writing experiments were then carried out with the experimental setup described in Fig. 6.3(a). The multimode fiber and proximal side of the calibration setup shown in Fig. 6.2(a) were jointly vertically displaced and the distal end of the fiber was dipped into a droplet of photoresist deposited on a plasma-cleaned glass slide. Three-dimensional microstructures were then fabricated in open-air conditions by digitally focusing and scanning point-by-point CW laser light through the fiber using the wavefront shaping system at the proximal end.

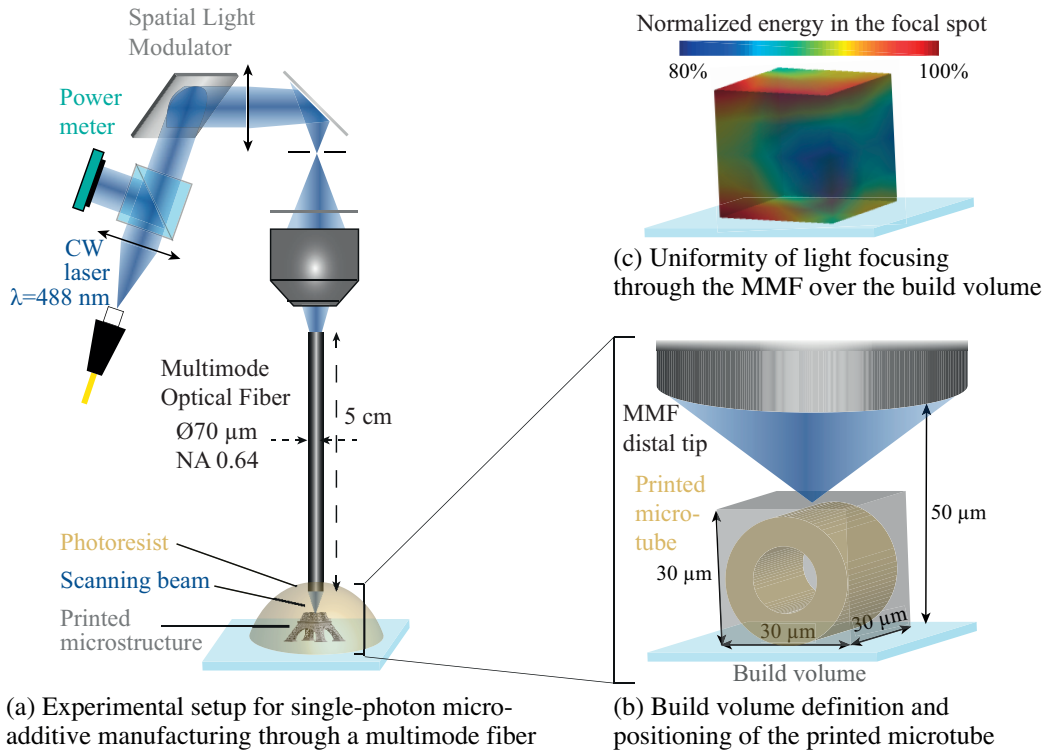


Figure 6.3 – Experimental setup and parameters for single-photon three-dimensional microfabrication through a multimode fiber

The microstructures were written into a cubic volume of 30- μm edge (see the close-up view in Fig. 6.3(b)). This build volume was centered on the optical axis of the fiber and microstructures were fabricated with a bottom-up approach, starting from the glass slide, 50 μm below the fiber's distal facet. The uniformity of light delivery over the build volume is of paramount

importance to correctly print microstructures. Therefore, the ratio of energy focused in the phase-controlled spot over the total field energy was measured and a maximal energy gap of 20% over the build volume was observed (see Fig. 6.3(c)), which I assume to be reasonable to print simple structures within this volume. The uniformity of light delivery could be improved to further enlarge the build volume, for instance by compensating for the spot distortion as light is focused off the fiber's axis [140].

To build three-dimensional microstructures through the multimode fiber with a CW laser, I used the photoresist described in chapter 5 for which was measured a non-linear single-photon photopolymerization behavior: an organic polymer precursor trimethylolpropane triacrylate (TMPTA; >70%, Aldrich, USA), 1wt% of the Norrish type II photoinitiator camphorquinone (CQ; 97%, Aldrich, USA) and 0.5wt% of the synergist ethyl 4-(dimethylamino) benzoate (EDAB; 97%, Aldrich, USA).

6.2 Curing method for optimal single-photon three-dimensional fabrication

6.2.1 Generation of high-contrast laser focal spots through the multimode fiber

The challenge of three-dimensional microfabrication using single-photon photopolymerization is to avoid the cumulative off-focal polymerization that may eventually solidify unwanted volumes. To prevent this cumulative polymerization and ensure the curing of a specific voxel element, the non-linear single-photon photopolymerization process determined in chapter 5 must be combined with a high contrast focus of light and an optimal curing method.

Therefore, using the setup of Fig. 6.3(a), light was focused 50 μm below the fiber's distal facet and the spot's point spread function intensity distribution was measured (see Figs. 6.4(a)-6.4(b)), showing more than a 200-fold contrast between the peak focal intensity (in white in Figs. 6.4(a)-6.4(b)) and the direct surroundings (in green in Figs. 6.4(a)-6.4(b)).

6.2.2 Sampling parameters

To determine the optimal curing method, using the setup of Fig. 6.3(a), I experimentally built test three-dimensional microstructures with various printing parameters. The test microstructure is a hollow microtube ($\varnothing_{in} = 21.5\mu\text{m}$, $\varnothing_{out} = 31.5\mu\text{m}$, length : $20\mu\text{m}$) whose axis is perpendicular to the fiber's optical axis (see Fig. 6.3(b) for the position of the microtube). Such a test microstructure allows studying both the axial confinement of photopolymerization through imaging the void of the tube, and the ability of my technique to print suspended structures. These microstructures were built through pointwise scanning with a bottom-up approach, starting from the glass substrate, 50 μm below the MMF's distal facet. The lateral and axial sampling pitches were varied between $\frac{1}{3}$ and $\frac{3}{2}$ of the respective lateral and axial spot FWHM (see Figs. 6.4(c)-6.4(d)) fitted from the measurement of Figs. 6.4(a)-6.4(b). The optimal

printing parameters were further investigated by varying the spot power from 70 nW to 800 nW, thus covering the range of polymerization threshold power determined in chapter 5 (see Fig. 6.5) whereas the exposure time per scanning spot was fixed to 0.06s or 0.1s to build the microstructures as fast as technically possible (see section 6.3) and to avoid long-term power drifts.

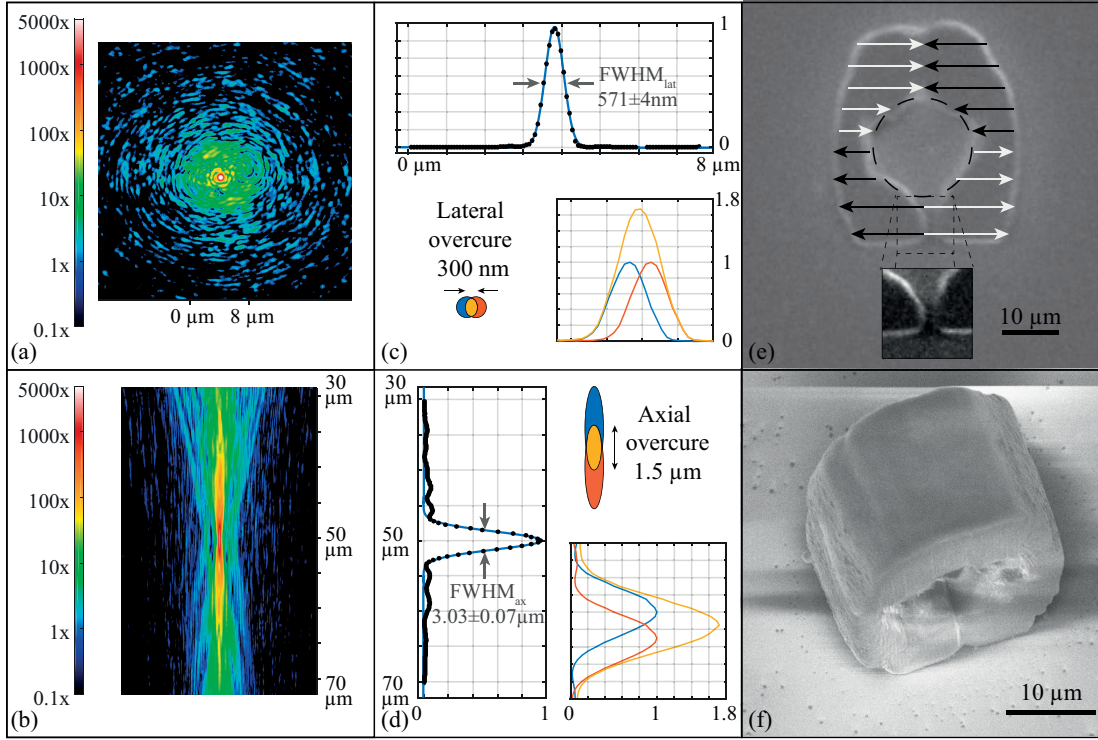


Figure 6.4 – (a) Lateral PSF measured through the MMF in the focal plane (b) Axial PSF measured through the MMF (c) Fit of the data of Fig. 6.4(a) and experimental lateral overlapping of the voxels during 3D printing with the computed cumulative intensity (d) Fit of the data of Fig. 6.4(b) and experimental axial overlapping of the voxels during 3D printing with the computed cumulative intensity (e) SEM image of a non-optimal printing of a micro-hollow tube through the MMF via single-photon photopolymerization (0.1s exposure time per spot, 159 ± 2 nW/spot). The axis of the microtube was printed orthogonally to the MMF optical axis, the microstructure fell aside during development revealing the tube's cross-section. The arrows indicate the scanning direction for building the microstructure. (f) SEM image of a micro-hollow tube printed through the MMF via single-photon photopolymerization (0.06s exposure time per spot, 208 ± 2 nW/spot).

6.2.3 Optimal curing strategy

I empirically determined that the optimal printing method consists in combining a large lateral and axial overlap of the scanning spots with an operating spot power below the polymerization threshold. More precisely, the respective optimal lateral and axial overlap of the spots are $\sim \frac{FWHM_{lat}}{2}$ and $\sim \frac{FWHM_{ax}}{2}$ (see the overcure parameters in Figs. 6.4(c)-6.4(d)) and the optimal

6.2. Curing method for optimal single-photon three-dimensional fabrication

experimental spot power is between $\sim 120\text{ nW}$ and $\sim 250\text{ nW}$ (see the gray area in Fig. 6.5). With a looser lateral and axial sampling I observed a collapse of the microstructure, if printed at all. A higher spot power resulted in an overpolymerized microcylinder, conversely a lower spot power yielded imperfectly printed microtubes.

I hypothesize that the lateral and axial overlap of the sampled spots resulted in an overcuring of one voxel (see blue spots and curves in Figs. 6.4(c)-6.4(d)) by the next one (see orange spots and curves in Figs. 6.4(c)-6.4(d)), thus providing a cumulative dose (see yellow spots and curves in Figs. 6.4(c)-6.4(d)) that overcame the photopolymerization threshold (see Fig. 6.5).

This hypothesis is further supported by the microtube depicted in Fig. 6.4(e), which is imperfectly printed. This microtube fell aside during development hence revealing the tube's cross-section. The white and black arrows indicate the scanning directions adopted to print the curved structure layer-by-layer, from bottom to top. Interestingly, the bottom of the microtube was incompletely sealed (see close-up view in Fig. 6.4(e)), and I speculate that this volume element did not reach the polymerization threshold as the contiguous spots located in this area were not consecutively overcured. Indeed, the pointwise scanning first took place in the direction of the black arrow. This lasted 5 seconds, during which the median free radicals might have diffused or be scavenged by oxygen before the lateral overlapping scanning started in the direction of the white arrow. However, further time-resolved studies of the photopolymerization kinetics (see section 5.2.3) could help interpret these optimal printing parameters.

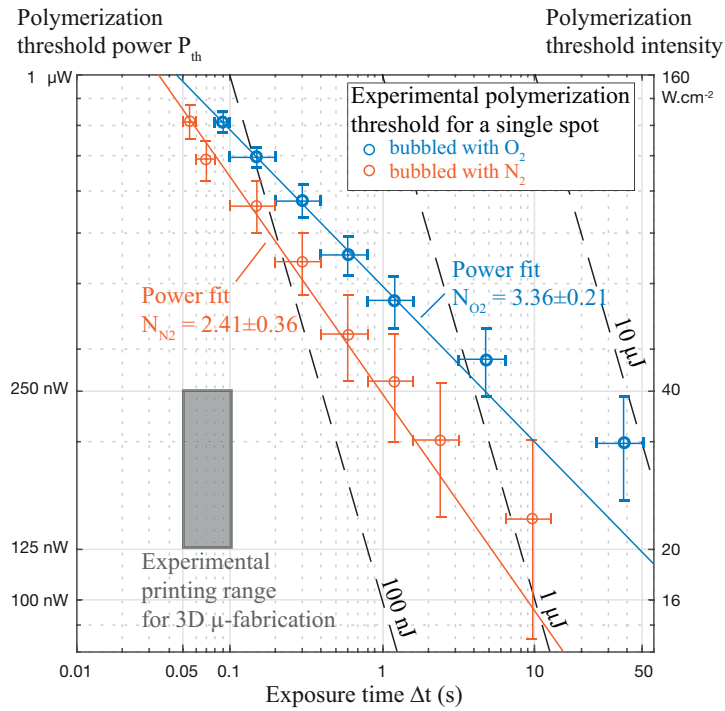


Figure 6.5 – Experimental printing range for three-dimensional microfabrication

Nonetheless, using a shorter exposure time per spot (0.06 s), a sealed microtube can be correctly printed (see Fig. 6.4(f)). The printed microtube exhibits a smooth surface but deviates from the designed model, the microtube's length is measured to be $20.0 \pm 0.3 \mu\text{m}$, the outer diameter $33.5 \pm 0.5 \mu\text{m}$ and the inner diameter $17.6 \pm 1.1 \mu\text{m}$ versus respectively $20 \mu\text{m}$, $31.5 \mu\text{m}$ and $21.5 \mu\text{m}$ as defined in the model. The microtube's walls are therefore too thick and further optimization of the printing parameters is required to produce accurate structures. Though not perfectly true to the model, this hollow microstructure demonstrates the possibility to remove the off-focal polymerization inherent to single-photon photopolymerization by taking advantage of the non-linearity of the photoresist.

6.3 Limitations of the current device

6.3.1 Hardware limitations

The printing speed of my curing system is currently limited by the refresh rate (20 Hz) of the spatial light modulator (SLM in Fig. 6.3(a)), which yields a one-hour printing time for the microtube depicted in Fig. 6.4(f). A digital micro-mirror device (DMD), capable of refresh rate over 20 kHz, could also be used as a phase control system [141] at the cost of a lower efficiency of modulation than SLMs. Owing to the low power required by the writing method, the power budget of the phase control system is not of crucial importance, and the use of a DMD would dramatically increase the printing speed. However, the scanning speed might ultimately be limited by the oxygen diffusion time [142].

Experimentally, I also observed that successful three-dimensional microfabrication requires to have more than $\sim 30\%$ of the MMF's output laser power focused within the phase-controlled spot. Otherwise, the laser power of the background speckle appears to cumulatively degrade the printing quality. Finally, my attempts to fabricate three-dimensional microstructures with a lower multimode fiber's numerical aperture ($\text{NA} = 0.22, 0.39$) did not succeed as no proper axial confinement of photopolymerization could be achieved.

6.3.2 Lateral printing resolution

To determine the achievable complexity of the microstructures printed with my curing device, its lateral and axial printing resolution was investigated. The printing resolution is determined following Abbe's criterion, that is to say the minimal printable grating period is measured, both laterally and axially, which is often different from the minimal achievable linewidth [11]. Hence, using the setup of Fig. 6.3(a), I printed a series of gratings with a decreasing period to determine the achievable lateral printing resolution. As evidenced in Fig. 6.6(a), a grating with a lateral pitch of $1.05 \pm 0.06 \mu\text{m}$ can be resolved (see blue curve in Fig. 6.6(a)) whereas a grating period of $0.9 \mu\text{m}$ cannot be resolved (see red curve in Fig. 6.6(a)). The lateral printing resolution could likely be improved using the phenomenon observed in Fig. 6.4(e), that is to say by writing the adjacent lines with a long time period between each. In this way, the free

radicals generated when writing the first line would have time to diffuse or be inhibited before writing the second line, thus decreasing the cumulative dose of the interval between two lines.

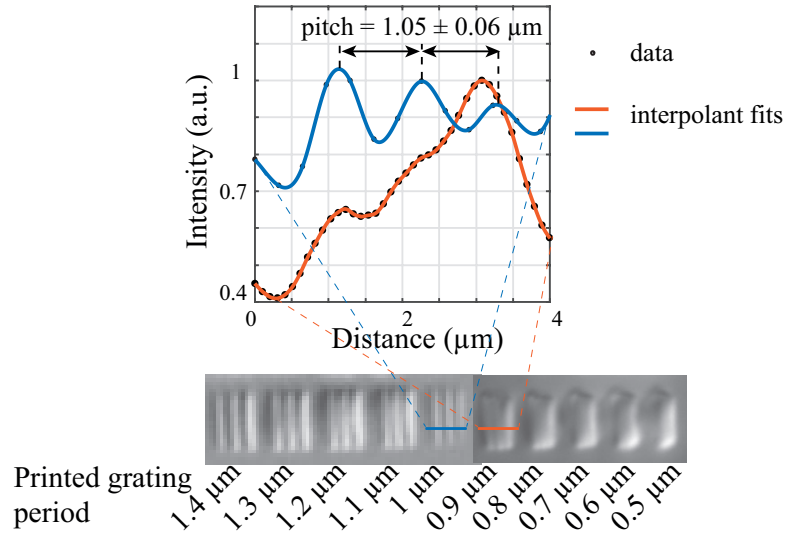


Figure 6.6 – Lateral printing resolution of our fiber-based single-photon micro-additive manufacturing device. Series of lines are printed with a decreasing pitch to determine the lateral printing resolution using Abbe's criterion.

6.3.3 Axial printing resolution

Similarly, in order to determine the axial printing resolution, the minimal axial separation between two polymer structures was measured. As shown in Fig. 6.4(f), a hollow micro-tube of $21.5\ \mu\text{m}$ inner diameter can be printed with our device, which means that two lines printed $21.5\ \mu\text{m}$ axially apart can be resolved. Furthermore, by slightly overpolymerizing the same model structure, it is possible to generate axially adjacent lines separated by only $9.3 \pm 0.7\ \mu\text{m}$ (see Fig. 6.7(a)). However, lines designed to be $7.5\ \mu\text{m}$ axially apart could not be resolved (see Fig. 6.7(b)), even though we targeted the lower end of the printing dynamic range (0.051s exposure per spot and 150nW per spot) to avoid overpolymerization. Suspended lines as thin as $3\ \mu\text{m}$ can still be printed through my ultra-thin curing probe, as shown in Fig. 6.7(c).

Improving the lateral printing resolution would either require using higher numerical aperture multimode fibers or adapt the exposure of each scanned spot to account for the crosstalk exposure induced by scanning nearby parts of the microstructure. Such proximity exposure corrections are studied in the next section.

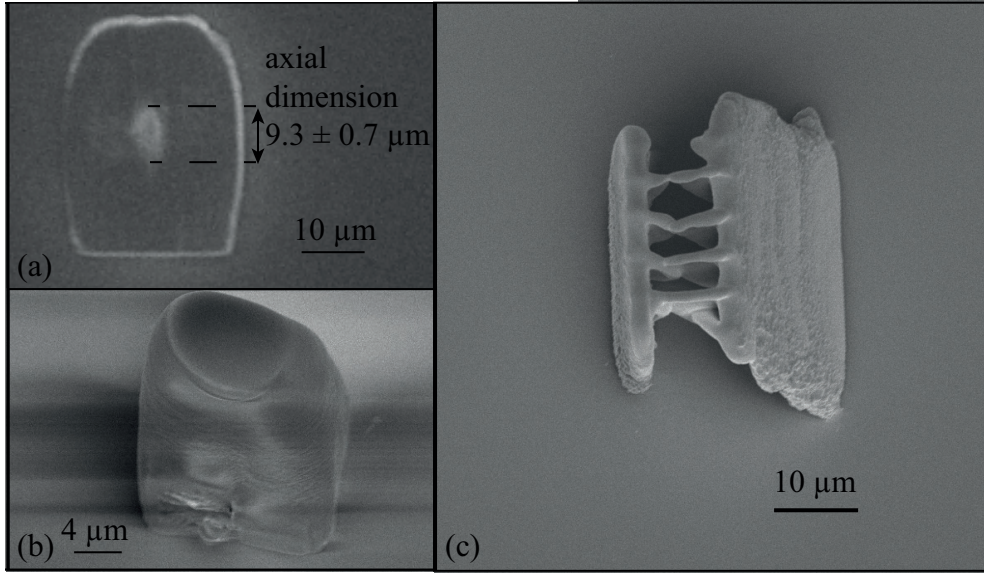


Figure 6.7 – (a) SEM top view of the smallest axial separation achieved between two solid lines. The model structure is the same as in Fig. 6.4(e) i.e. a micro-hollow tube of respectively $21.5\mu\text{m}$ and $31.5\mu\text{m}$ inner and outer diameter. (0.08s/spot , $197 \pm 2 \text{ nW/spot}$). The microtube fell aside during development. The slight overpolymerization of the structure results in a narrower hollow tube than designed. (b) SEM perspective view of an axially non-resolved hollow microtube. The model parameters are $\varnothing_{in} = 7.5\mu\text{m}$, $\varnothing_{out} = 15\mu\text{m}$, length = $10\mu\text{m}$. (0.051s/spot , $149 \pm 1 \text{ nW/spot}$) (c) Suspended lines (0.051s/spot , $204 \pm 2 \text{ nW/spot}$).

6.4 Exposure correction algorithms

6.4.1 Proximity exposure correction

During pointwise scanning of the build volume, the lateral and axial extent of the laser point spread function (PSF) leads to the exposure of nearby areas (see PSF extent in Figs. 6.4(a)-(b)). This overlap of the exposed regions is essential to my curing method (see section 6.2.3) yet the overall crosstalk accumulated dose from the exposure of the whole structure degrades the printing quality [111].

To correct for this single-photon accumulated dose, Wan and Menon [111] developed a proximity exposure correction (PEC) algorithm. Briefly, as shown in the flowchart and cross-sections of Fig. 6.8, the initial three-dimensional target model is used to create an exposure map. In other words, every voxel that we aim at polymerizing is initially assigned a unitary value of exposure in the three-dimensional exposure map (see step A in Fig. 6.8). The resulting absorbed dose is then derived through convolution of the exposure map with the PSF (see step B in Fig. 6.8). Thresholding the dose map yields the three-dimensional polymerized map, which is then subtracted to the model to yield the error map (see steps C and D in Fig. 6.8).

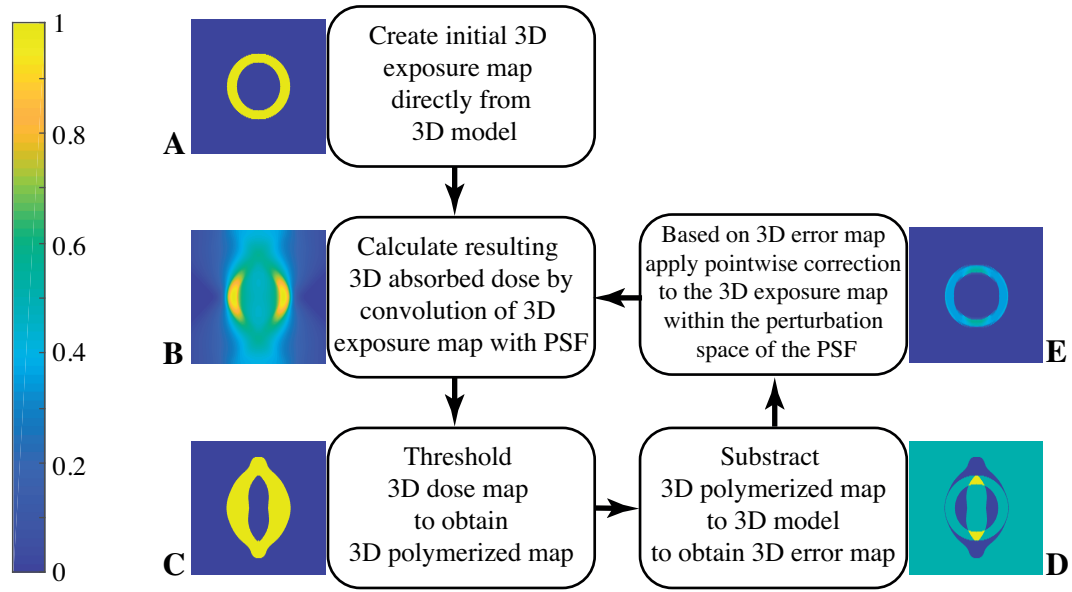


Figure 6.8 – Proximity exposure correction algorithm

Applying this algorithm to the polymerization of our microtube model (length: $30\text{ }\mu\text{m}$, $\varnothing_{in}=21.5\text{ }\mu\text{m}$, $\varnothing_{out}=31.5\text{ }\mu\text{m}$ see Fig. 6.9(a)), we observe that the exposure map is significantly modified and allows improving the fidelity of the printing structure to the model (see cross-sections and total error in Fig. 6.9(b)). It is noteworthy that this polymerization model does not take into account the non-linear photopolymerization process induced by oxygen, thus there appears a simulated "lime" shape of the cylinder, which I did not observe in the experimental photopolymerization of the microtube (see Fig. 6.4(f)). Though this PEC algorithm could potentially improve the printing resolution, I hypothesize it has better performance on structures with lower fill ratio than our microtube, such as woodpiles for example [111].

Another limitation of this proximity exposure correction method is that the algorithm tends towards negative exposure values on the structure edges, in order to sharpen them. Negative exposure and negative intensities cannot be physically produced. On the other hand, the complex amplitude of light beams can take negative values and interfere destructively to yield regions of null intensity, which is investigated in the next section.

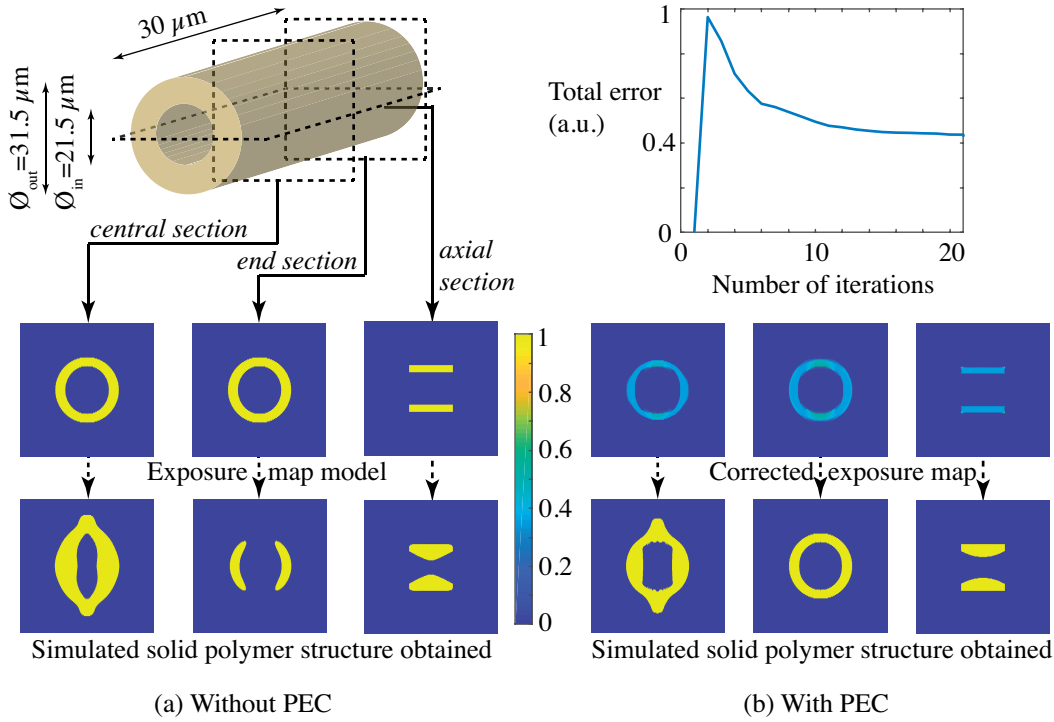


Figure 6.9 – Proximity exposure correction algorithm applied to the microtube model

6.4.2 Volumetric phase optimization

Additive manufacturing of three-dimensional microstructures is generally achieved by point-wise scanning [143] or layer-by-layer curing, such as in micro-stereolithography [144]. Such sequential printing strategies set limitations on the printing speed as well as on the complexity of printing shapes. For instance, overhanging geometries need support structures to not collapse during printing [145].

Volumetric printing, that is to say the exposure and curing of a whole volume of photosensitive material in one step, requires generating arbitrary three-dimensional exposure patterns. In this section, I study the generation of such holographic three-dimensional intensity pattern using wavefront shaping through our multimode fiber curing probe (see Fig. 6.3(a)).

As a case study, we investigate the generation of a tube of light, whose axis is orthogonal to the multimode fiber's optical axis (see Fig. 6.11(a)), similar to the microprinted tube in Fig. 6.3(b). The tube of light we intend to generate is $30 \mu\text{m}$ long but as opposed to our microprinted tube (see Fig. 6.4(f)) it has an elliptical section of outer diameter $31.5 \mu\text{m}$ by $5.2 \mu\text{m}$ respectively along the axial and lateral directions (see Fig. 6.11(a)). Computational limitations indeed prevent to define a larger lateral diameter.

To focus light, be it on a spot or on an arbitrary pattern, we need to know the complex amplitude to display at the fiber output, which is the output vector Y in Fig. 6.2(b), in order to

determine the required input vector X to display with the spatial light modulator at the fiber proximal end (see Fig. 6.2(b)). A direct way to find this wavefront Y would be to follow steps A, B and C in Fig. 6.10. The targeted three-dimensional intensity pattern would be decomposed in multiple layers corresponding to the different depth cross-sections of the pattern (see step A in Fig. 6.10), each of these slices is then numerically optically propagated [146] towards a common plane 1 in step B in Fig. 6.10. These complex amplitudes are then summed, thus defining the wavefront Y to generate at the fiber output (see step C in Fig. 6.10).

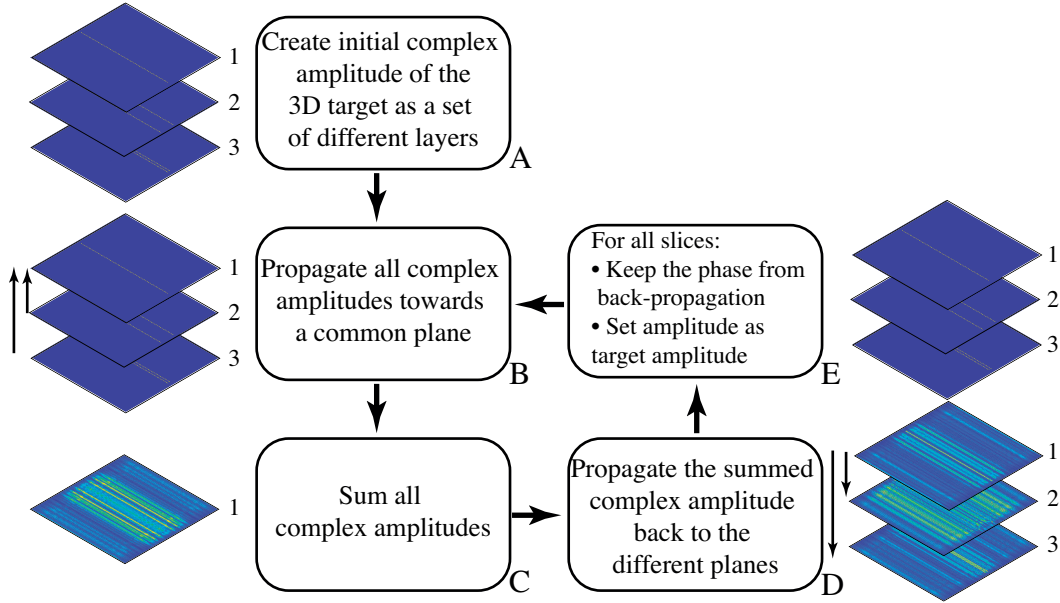


Figure 6.10 – Multi-plane Gerchberg-Saxton algorithm

However, the phases of each layer might interfere destructively when summed in this common plane, which will degrade the three-dimensional light pattern. We experimentally evidenced this degradation by generating, with the above procedure, the wavefront corresponding to the tube of light described in Fig. 6.11(a). As shown in the axial and lateral cross-sections of the tube in Fig. 6.11(b), this direct summation process results in a three-dimensional intensity pattern not true to the model.

The phase of the output vector Y should therefore be optimized prior to calculating the input wavefront X . To do so, we developed together with my colleague Dr. Damien Loterie a multi-plane phase-optimization algorithm inspired by the Gerchberg-Saxton algorithm [147, 148]. In this iterative algorithm, described in Fig. 6.10, following the definition of the stack of target layers (step A), their numerical propagation (step B) and summation (step C), the resulting sum of the complex amplitude is numerically back-propagated to each plane (see step D in Fig. 6.10). The amplitude of each layer is then reset to the one of the target layers, while the phase resulting of the back-propagation is preserved (see step E in Fig. 6.10). Steps B, C, D and E are then iterated.

In this way, the phase of the wavefront Y is quickly optimized and allows generating a three-

dimensional microtube of light through the multimode fiber as shown in Fig. 6.11(c). As the power level required to cure a single spot in the photoresist is small (see section 6.2.3), we attempted to directly photopolymerize the whole volume of the tube in one step through the multimode fiber. The size of the generated structure did not allow us to determine if the printed tube was hollow. However, applying this phase optimization algorithm to larger microstructures, such as scaffolds could open up new possibilities for direct holographic microprinting.

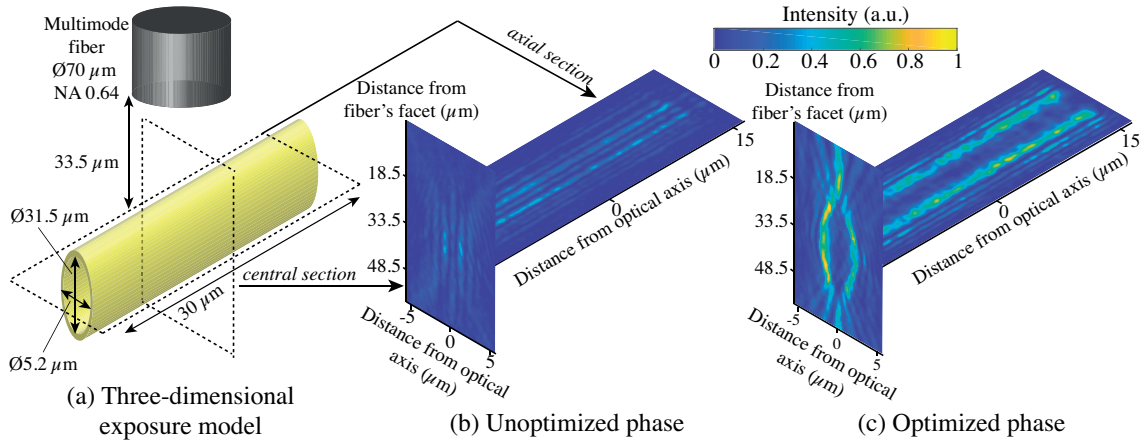


Figure 6.11 – Experimental generation of a three-dimensional intensity pattern through the multimode fiber

6.5 Conclusion

In this chapter, I demonstrated that oxygen inhibition combined with single-photon absorption can be used through a $70\text{-}\mu\text{m}$ thick multimode fiber to build three-dimensional microstructures. This is achieved without any motion of the multimode fiber, by digitally scanning a phase-controlled laser spot over the build volume. I studied exposure correction algorithms and showed that complex three-dimensional light patterns can directly be generated through the multimode fiber.

Single-photon off-focal photopolymerization is inhibited by taking advantage of the non-linearity of the photoresist, which is induced by oxygen radical scavenging. The experiments provide evidence that optimal writing of the microstructures is achieved by combining a large lateral and axial overlap of the scanning spots with an operating spot power below the photopolymerization threshold. Thus, it appears that a volume element is only polymerized if the cumulative exposure dose reaches the polymerization threshold within a writing time shorter than the termination time of free-radicals.

My curing system, made of a CW laser and an ultra-thin multimode fiber, constitutes an affordable and compact alternative to existing microfabrication setups and creates new oppor-

tunities for *in vivo* microfabrication through endoscopes. In the same way, this device could foster research towards the miniaturization of microfabrication systems and therefore for the integration of several additive manufacturing tools on a single platform.

7 Conclusion

This thesis presents new implementations of laser-actuation for direct three-dimensional embedded printing and the development of a compact toolkit for high-resolution additive manufacturing.

7.1 Summary of results

7.1.1 Laser-induced direct three-dimensional liquid delivery

In the first part of this work, laser-induced forward transfer was applied to realize direct three-dimensional liquid delivery with the aim of providing a high-resolution alternative to microextrusion-based three-dimensional embedded printing.

Laser-induced depth-controlled delivery of picoliter doses within a 300- μm gelatin soft substrate was demonstrated. The injection depth was controlled by producing 15- μm stable liquid streams over a wide range of velocity (10-80 m/s) with a conventional laser-induced forward transfer system. Increasing laser fluences result in faster liquid jets. As the jet impact velocity on the soft gelatin substrate increases, these liquid jets penetrate deeper into it, thanks to the Bingham plastic properties of gelatin. Using this process, picoliter doses could be delivered up to depth of $\sim 230\text{ }\mu\text{m}$ with a 25- μm depth repeatability and a 12- μm lateral resolution. As the achieved laser-assisted device operates over two lateral dimensions, controlling the delivery depth results in creating a direct three-dimensional liquid delivery system.

7.1.2 Compact toolkit for high-resolution additive manufacturing

In the second part of this thesis, laser-actuation was applied to realize compact drop-on-demand and direct laser writing tools for high-resolution additive manufacturing.

Inkjet printing of viscous monodisperse droplet by laser-induced flow focusing

Laser-induced drop-on-demand generation was demonstrated through a 300- μm glass microcapillary. The production of viscous micro-droplets with a smaller diameter than the microcapillary diameter was achieved by exploiting a flow focusing effect, thus demonstrating a subnozzle printing resolution. A stable satellite-free drop-generation regime was evidenced for a wide range of viscous inks (2–200 mPa s). Selectivity of this jetting regime required fine or coarse adjustments of the laser-pulse energy, respectively, for the inks of low and high viscosity. In addition, the achieved drop-on-demand system extends the range of printable liquids to a range of Ohnesorge numbers (Oh) from 0.1 to 1 for conventional inkjet printers to approximately $0.01 < Oh < \sim 1.5$.

Direct laser writing through a multimode fiber

Single-photon three-dimensional microfabrication with a 1.0- μm lateral and 21.5- μm axial printing resolution was demonstrated through a 70- μm multimode optical fiber. This was achieved without any motion of the multimode fiber, by digitally scanning a phase-controlled laser spot over the build volume. Single-photon off-focal photopolymerization was inhibited by taking advantage of oxygen radical scavenging, which induces a non-linearity of the photoresist. Optimal writing of the microstructures was achieved by combining a large lateral and axial overlap of the scanning spots with an operating spot power below the measured photopolymerization threshold. Thus, it appears that a volume element was only polymerized if the cumulative exposure dose reached the polymerization threshold within a writing time shorter than the termination time of free radicals.

7.2 Future work

Future work could address the limitations of the devices developed in the course of this thesis.

7.2.1 Laser-induced direct three-dimensional liquid delivery

High-resolution three-dimensional embedded printing would require delivering at arbitrary depths infinitesimal liquid amounts within a gel-like substrate. As evidenced in this thesis, achieving such performances with laser-induced forward transfer would demand to generate monodisperse droplets over a wide range of velocity rather than the current thin jets. Indeed, the shape of these laser-induced jets results in a column of injected liquid covered by a large volume of liquid on the substrate interface. Time-resolved imaging showed that the low-velocity components of the jets are responsible for this poor injection efficiency. A dimensionless analysis of the jetting regimes revealed that single-droplet generation could be achieved by lowering the ink's concentration in sodium alginate. Future work should therefore focus on rheological optimization of the jetted ink.

7.2.2 Compact toolkit for high-resolution additive manufacturing

Inkjet printing of viscous monodisperse droplet by laser-induced flow focusing

The current drop-on-demand device constitutes the basis of the first component of the developed compact toolkit for high-resolution additive manufacturing. The present device is actuated by focusing a nanosecond laser pulse through a microscope objective. Further miniaturization of the drop-on-demand system could be achieved in future work by implementing wavefront shaping through a multimode fiber enclosed in the microcapillary, thus providing a compact digital laser-actuation.

Direct laser writing through a multimode fiber

The performances of the compact direct laser writing device created in this work currently face two main limitations: the printing speed and the axial printing resolution. Owing to the low power budget required with the developed curing technique, a faster digital light scanning could be achieved using a digital micro-mirror device (DMD) instead of a spatial light modulator (SLM) for wavefront shaping. The axial printing resolution could be improved by further investigation of the exposure correction algorithms presented in this thesis. In the same way, the systematic study of the photopolymerization kinetics of various photoresists could help identifying chemical compounds more prone to oxygen radical scavenging, which is essential to remove single-photon off-focal photopolymerization.

7.3 End word

As shown in this thesis, laser-actuation has the potential to provide alternative technical solutions in the field of microprinting, be it for direct laser writing, drop-on-demand generation or embedded three-dimensional printing.

The laser-actuated three-dimensional liquid delivery system demonstrated in this work constitutes a proof-of-concept of injection at arbitrary depths through liquid velocity control. The precision of the achieved device could open new possibilities to replicate the complex micro-architecture of tissues. Furthermore, this approach could also offer a precise and high-throughput alternative to existing needle-free microjet injectors.

In the same way, laser-actuated drop-on-demand generation allows delivering monodisperse droplets with a wide range of viscous liquids, thus overcoming one of the main limitations of conventional inkjet printers.

Similarly, the developed direct laser writing device, made of a continuous-wave laser and an ultra-thin multimode fiber, provides an inexpensive and compact alternative to conventional direct laser writing systems, which rely on complex and bulky femtosecond lasers.

Chapter 7. Conclusion

Finally, combining these endoscopic-like drop-on-demand and direct laser writing devices would also provide an enabling toolkit for *in vivo* microprinting. The achieved 1.0- μm lateral and 21.5- μm axial printing resolution of the fiber-based direct laser writing system could indeed allow studying interactions at the cellular level by fabricating biologic scaffolds.

A Modelization of oxygen-inhibited single-photon photopolymerization

In this appendix, I derive the rate equations of photopolymerization in the case of single-photon absorption combined with oxygen free radical scavenging. Oxygen replenishment through diffusion is also taken into account. Simulations of chain growth and polymer conversion at focus of a Gaussian beam are then performed using a partial differential equation (PDE) solver in *Wolfram Mathematica*®10.

A.1 Photopolymerization model

A.1.1 Initiation and propagation

As mentioned in chapter 5, photo-induced polymer growth results from three steps: *photo-initiation*, *propagation* and *termination*. Briefly the photopolymerization mechanism is the following [105, 106]: upon absorption of a photon, a photoinitiator I is generally homolytically cleaved to generate two free radicals $R\cdot$ that then react with a first polymer precursor M_1 to create a chain-initiating radical $M_1\cdot$ (see Eq. A.1).



The polymer chain is then grown by successive additions of polymer precursors M to the existing chain radical $M_n\cdot$, thus creating a longer chain radical $M_{n+1}\cdot$. This is the propagation step (see Eq. A.2):



Appendix A. Modelization of oxygen-inhibited single-photon photopolymerization

To simplify the model, we consider that each reactive chain radical is equivalent to the first generated reactive radical $R\cdot$ [106]. Thus, the chain radical $M_n\cdot$ that reacts with a polymer precursor M to yield a longer chain radical $M_{n+1}\cdot$ is assimilated to the reaction of a radical $R\cdot$ with an unreacted double bond B of the polymer precursor M to yield a radical $R\cdot$. Equations A.1-A.2 are then rewritten as:



A.1.2 Termination

In the case of acrylates, the combination mode (first equation of Eq. A.4) dominates the disproportionation mode of termination (see second equation of Eq. A.4) [106], therefore the equations for the termination of polymerization first introduced in chapter 5:



can be simplified to:



And applying our simplified notation on the reactive radical, we obtain that equation A.5 is equivalent to:



A.1.3 Oxygen inhibition

We also take into consideration the polymerization inhibition by the oxygen dissolved within the photoresist, which is equivalent to a second mode of termination of the reactive radicals $R\cdot$:



The chemical reactions of our photopolymerization model sum up as:



where I is the photo-initiating species (for instance a photoinitiator), $R\cdot$ are radicals, B are unreacted double bonds of the photopolymer and O_2 is the dissolved oxygen in the photoresist.

A.2 Photo-initiation

A.2.1 Initiating gaussian beam

To model the kinetics of photopolymerization, one must first accurately describe the propagation and absorption of a focused light beam within the photopolymer. Due to the axisymmetry of the problem, we limit our study to a 2D model in the yz space, z being the propagation direction from the focusing optics (see Fig. A.1).



Figure A.1 – Description of the orientation of simulation

We assume a linearly polarized light. The propagating x -component E_x of the electrical field of the Gaussian initiating field focused in the photopolymer can be written as [149]:

$$E_x(y, z) = E_0 \frac{\omega_0}{\omega(z)} e^{-\frac{y^2}{\omega(z)^2}} e^{-i\left(\frac{ky^2}{2R(z)} + kz - \eta(z)\right)} \quad (\text{A.9})$$

with:

- E_0 the nominal electrical field, in V m^{-1} ,
- ω_0 the beam waist at focus, in m,
- $\omega(z)$ the beam waist at depth z in the polymer, in m,
- k , the wavenumber, in m^{-1} ,
- $R(z)$ the wavefront radius of curvature, in m,

Appendix A. Modelization of oxygen-inhibited single-photon photopolymerization

- $\eta(z)$ the Gouy phase.

In the case of a diffraction-limited focus, these parameters are defined as:

$$E_0 = \sqrt{\frac{2\Phi_0}{cn_0\epsilon_0}} \quad (\text{A.10})$$

$$\omega_0 = \frac{\lambda}{\pi n_0 NA} \quad (\text{A.11})$$

$$\omega(z) = \omega_0 \sqrt{\left(\frac{z}{z_R}\right)^2 + 1} \quad (\text{A.12})$$

$$R(z) = z \left(\left(\frac{z}{z_R}\right)^2 + 1 \right) \quad (\text{A.13})$$

$$\eta(z) = \tan^{-1} \left(\frac{z}{z_R} \right) \quad (\text{A.14})$$

with:

- Φ_0 the nominal intensity of the beam, in W m^{-2} ,
- c the speed of light, $c = 299792458 \text{ m s}^{-1}$,
- ϵ_0 the permittivity of vacuum $\epsilon_0 = 8.854187818 \cdot 10^{-12} \text{ F m}^{-1}$ that we approximate to the relative permittivity of the polymer precursor mixture,
- n_0 the refractive index of the polymer precursor, $n_0 = 1.474$ at room temperature,
- λ the laser wavelength, here $\lambda = 488 \text{ nm}$,
- NA the numerical aperture of the focusing optics, which is here the multimode fiber, then $NA = 0.64$,
- z_R the Rayleigh range, in m.

The nominal intensity and Rayleigh range of the beam can be derived from the other parameters:

$$\Phi_0 = \frac{2P_{fiber}}{\pi\omega_0^2} \quad (\text{A.15})$$

$$z_R = \frac{\pi n_0 \omega_0^2}{\lambda} \quad (\text{A.16})$$

where P_{fiber} is the input optical power, which corresponds to the optical power at the fiber distal end.

Finally, the propagated intensity Φ is derived from Eq. A.9:

$$\Phi(y, z) = \frac{1}{2} c n_0 \epsilon_0 |E_x(y, z)|^2 \quad (\text{A.17})$$

A.2.2 Light absorption

The rate of photo-consumption of the initiator I (see first equation of Eq. A.8) is proportional to the volumetric amount of absorbed photons Φ_a and the concentration $[I]$ of initiator in solution:

$$\frac{\partial [I](t, y, z)}{\partial t} = -k_d [I](t, y, z) \Phi_a(y, z) \quad (\text{A.18})$$

where the rate constant for dissociation k_d encompasses the efficiency χ of the photoinitiator species to generate a free radical for each photon absorbed [105], therefore k_d is written:

$$k_d = \frac{\lambda \chi}{c h N_A} \quad (\text{A.19})$$

with:

- $\Phi_a(y, z)$ the local volumetric light absorption in W m^{-3} , which is assumed to be locally constant as the fiber output power does not vary is assumed to be constant,
- λ the laser wavelength,
- χ the photoinitiation efficiency, ($\chi=1$ if one absorbed photon yields two radicals),
- c the speed of light,
- h the Planck constant, $h = 6.62607004 \cdot 10^{-34} \text{ m}^2 \text{ kg s}^{-1}$,
- N_A the Avogadro number, $N_A = 6.022140857 \cdot 10^{23}$,

In short, k_d converts the absorbed intensity into moles of efficient photons.

Hence, to determine the rate of photoinitiator consumption and consequently the rate of radical generation, we need to find the local volumetric light absorption of the Gaussian beam as it propagates and focuses in the photopolymer. Starting from Lambert-Beer law, the

Appendix A. Modelization of oxygen-inhibited single-photon photopolymerization

absorbed light intensity $\Phi_{slice}(z)$ after propagation through a slice thickness z of polymer is:

$$\Phi_{slice}(y, z) = \Phi(y, z)(1 - e^{-\alpha z[I](y, z)}) \quad (\text{A.20})$$

where:

- $\Phi(y, z)$ is the local incident light intensity at the outer surface of the absorbing layer,
- $[I](y, z)$ is the local molar concentration of the light-absorbing photoinitiator I in mol m^{-3} ,
- α is the absorption coefficient of I in $\text{m}^2 \text{mol}^{-1}$,

The local decrease of Φ_{slice} corresponds to the local volumetric light absorption Φ_a which we can write:

$$\Phi_a(y, z) = \frac{\partial \Phi_{slice}(y, z)}{\partial z} \quad (\text{A.21})$$

From Eq. A.21 we obtain the following expression for the local volumetric absorbed light intensity:

$$\Phi_a(y, z) = \alpha[I](y, z)\Phi(y, z)e^{-\alpha(z_0 - z)[I](y, z)} \quad (\text{A.22})$$

where z_0 is the working distance between the fiber facet and the focal spot.

As a first application of this light propagation and absorption model, I can validate the concentration of the photoinitiator species for a beam propagation and focusing $50 \mu\text{m}$ deep into a photoresist. The requirement for our system is to have a higher light absorption in the focal spot than in the optical path preceding the focal spot. Camphorquinone (CQ) is used as a photoinitiator in the photoresist, with a concentration $[CQ] = 66.2 \text{ mol m}^{-3}$. CQ absorption coefficient at the polymerizing wavelength ($\lambda = 488 \text{ nm}$) is $\alpha_{CQ} = 6.35 \text{ m}^2 \text{mol}^{-1}$.

As shown in Fig. A.2, the CQ concentration in the photoresist allows creating a zone of high intensity deep into the material whereas a photoinitiator with an absorption 500 times higher would absorb more in the first layers than in the targeted focal spot.

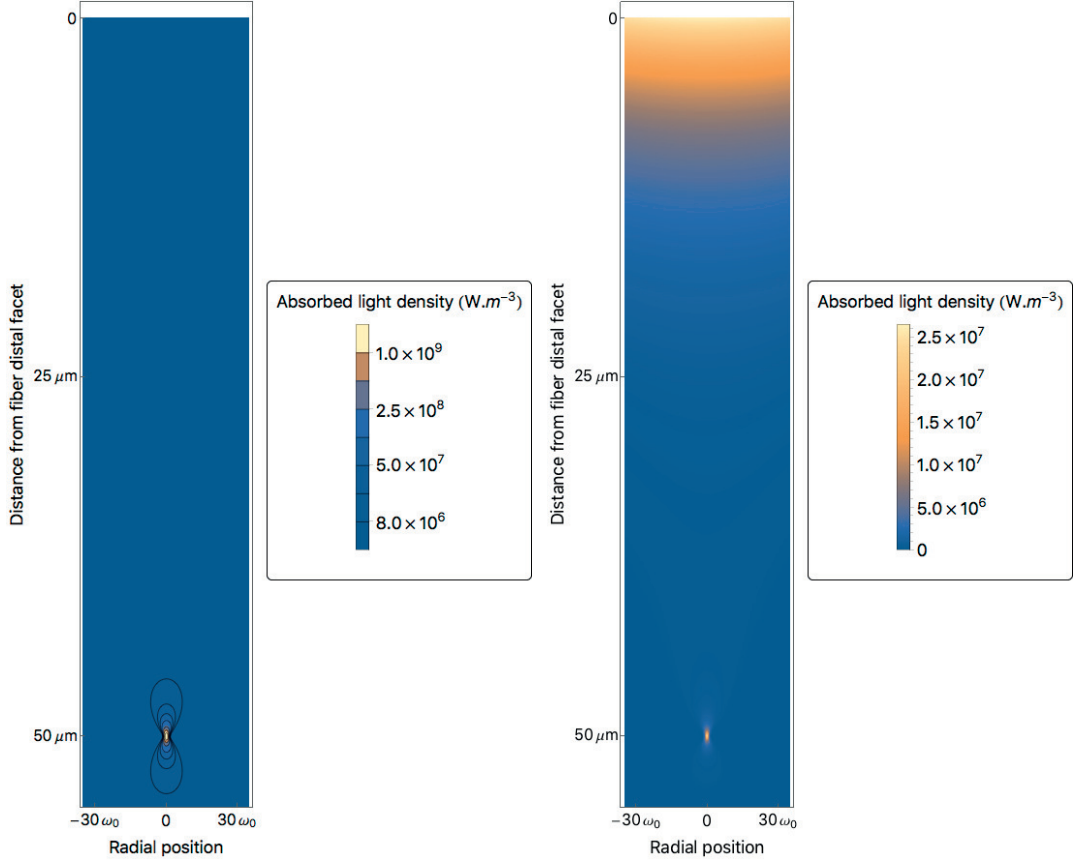


Figure A.2 – Simulation of absorbed light density for a 200-nW Gaussian beam focused 50 μm away from the multimode fiber (NA = 0.64) in our photoresist (left-hand side) and in a photoresist 500x more absorbing at $\lambda=488$ nm (right-hand side).

A.3 Photopolymerization rate equations

A.3.1 Single-photon photopolymerization without oxygen inhibition

From equations A.8, A.18 and A.22, we derive the following rate equations for photopolymerization without oxygen inhibition:

$$\frac{\partial[I](t, y, z)}{\partial t} = -k_d \alpha_{CQ} \Phi(y, z) [I](t, y, z) e^{-\alpha_{CQ}(z_0 - z) [I](t, y, z)} \quad (\text{A.23})$$

$$\frac{\partial[R\cdot](t, y, z)}{\partial t} = 2k_d \alpha_{CQ} \Phi(y, z) [I](t, y, z) e^{-\alpha_{CQ}(z_0 - z) [I](t, y, z)} - 2k_t [R\cdot]^2(t, y, z) \quad (\text{A.24})$$

$$\frac{\partial[B](t, y, z)}{\partial t} = -k_p [B](t, y, z) [R\cdot](t, y, z) \quad (\text{A.25})$$

Appendix A. Modelization of oxygen-inhibited single-photon photopolymerization

where k_d , k_t and k_p are respectively the rate constants for initiator dissociation, radical termination and polymer propagation (see Eq. A.8).

Equations A.23, A.24 and A.25 constitute a first system of non-linear differential equations that describes non-inhibited photopolymerization.

A.3.2 Oxygen-inhibited single-photon photopolymerization

In the case oxygen inhibition is further taken into account (see Eq. A.18), Eq. A.24 is modified as follows:

$$\frac{\partial[R\cdot](t, y, z)}{\partial t} = 2k_d\alpha_{CQ}\Phi(y, z)[I](t, y, z)e^{-\alpha_{CQ}(z_0-z)[I](t, y, z)} - 2k_t[R\cdot]^2(t, y, z) - k_{t,O_2}[O_2](t, y, z)[R\cdot](t, y, z) \quad (A.26)$$

where the right-hand terms of Eq. A.26 respectively correspond to the contribution of the photo-induced generation of radicals, their termination by combination and oxygen inhibition. k_{t,O_2} is therefore the rate constant for oxygen radical termination (see Eq. A.8).

Moreover, as oxygen is consumed during the inhibition reaction (see Eq. A.8), it creates a local concentration gradient. Owing to the creation of this gradient, oxygen consumption is replenished by diffusion. We can therefore derive the following equation for the concentration evolution of oxygen:

$$\frac{\partial[O_2](t, y, z)}{\partial t} = D_{O_2} \left(\frac{\partial^2[O_2](t, y, z)}{\partial y^2} + \frac{\partial^2[O_2](t, y, z)}{\partial z^2} \right) - k_{t,O_2}[O_2](t, y, z)[R\cdot](t, y, z) \quad (A.27)$$

where D_{O_2} is the diffusion coefficient of oxygen in solution which we estimate to be $D_{O_2} = 10^{-10} \text{ m}^2 \text{ s}^{-1}$ [106].

Equations A.23, A.25, A.26 and A.27 constitute the system of non-linear differential equations that describe oxygen-inhibited photopolymerization.

A.3.3 Rate constants

In most of my experiments, I used acrylic polymer precursors. For instance, one of the photoresists is made of off-the-shelf chemical components: an organic acrylate polymer precursor trimethylolpropane triacrylate (TMPTA; >70%, Aldrich, USA), 1wt% of the Norrish type II photoinitiator camphorquinone (CQ; 97%, Aldrich, USA) and 0.5wt% of the synergist Ethyl 4-(dimethylamino)benzoate (EDAB; 97%, Aldrich, USA).

The rate constant k_d for photoinitiator dissociation can be calculated knowing the efficiency χ of camphorquinone (see Eq. A.19) that was measured to be 0.07 ± 0.01 [150]. The other rate constants for propagation k_p , termination k_t and oxygen inhibition k_{t,O_2} are experimental

constants specific to each polymer precursor however typical values for acrylates can be found in the literature (see Table A.1).

Rate constant	Value	Reference
k_d ($\text{m}^3 \text{J}^{-1}$)	$2.9 \cdot 10^{-7}$	[150]
k_p ($\text{m}^3 \text{mol}^{-1} \text{s}^{-1}$)	15	[151]
k_t ($\text{m}^3 \text{mol}^{-1} \text{s}^{-1}$)	$2.5 \cdot 10^3$	[152]
k_{t,O_2} ($\text{m}^3 \text{mol}^{-1} \text{s}^{-1}$)	$5 \cdot 10^5$	[152]

Table A.1 – Rate constants for simulations of acrylate photopolymerization

A.3.4 Initial conditions

Non-inhibited photopolymerization

Based on the composition of the photoresist, the following initial conditions are set to simulate non-inhibited photopolymerization:

$$\begin{cases} [I](0, y, z) = 66.2 \text{ mol m}^{-3} \\ [R\cdot](0, y, z) = 0 \text{ mol m}^{-3} \\ [B](0, y, z) = 12.9 \cdot 10^3 \text{ mol m}^{-3} \end{cases} \quad (\text{A.28})$$

Oxygen-inhibited photopolymerization

Similarly, based on previous works [106], we set the following initial conditions to simulate oxygen-inhibited photopolymerization:

$$\begin{cases} [I](0, y, z) = 66.2 \text{ mol m}^{-3} \\ [R\cdot](0, y, z) = 0 \text{ mol m}^{-3} \\ [B](0, y, z) = 12.9 \cdot 10^3 \text{ mol m}^{-3} \\ [O_2](0, y, z) = 1.05 \text{ mol m}^{-3} \end{cases} \quad (\text{A.29})$$

A.4 Simulation results

A.4.1 Case study

The simulations are performed with *Wolfram Mathematica*®10 using the spatial PDE discretization method on the *NDSolve* PDE solver (additional options: method of lines with a tensor product grid and a minimum of 400 points).

Appendix A. Modelization of oxygen-inhibited single-photon photopolymerization

I simulate the temporal evolution of photopolymerization induced by the propagation and absorption of a Gaussian laser beam ($\lambda=488$ nm) focused $50\mu\text{m}$ deep into a photoresist (see Fig. A.3), whose absorptivity and chemical properties are described in sections A.2.2 and A.3.3 respectively. I further simulate the focusing of the laser beam by a NA 0.64 optical system, similar to the multimode fiber used in my compact high-resolution curing probe (see chapter 6).

Due to the axisymmetry of the model, the study is limited to a 2D model in the yz space, z being the propagation direction (see Fig. A.3). The simulations are then run on a two dimensional domain of $40\mu\text{m} \times 40\mu\text{m}$ centered on the focal spot, $50\mu\text{m}$ deep into the photoresist. The photopolymerization kinetics are studied on the first 0.8s of the process with a constant optical powers in the range of 100 nW.

Considering the length of the temporal domain studied, $\Delta t = 0.8\text{s}$, and the diffusion coefficient of oxygen $D_{O_2} = 10^{-10} \text{ m}^2 \text{ s}^{-1}$, I infer that the diffusion distance is $\Delta y \sim 13\mu\text{m}$ over this time. Hence, the half-width of the simulation domain being $20\mu\text{m}$, boundary conditions are applied on the limits of the simulation domain specifying that the oxygen concentration remains constant over time in order to ease the PDE solving in the case of the oxygen-inhibited simulations.

Finally, since the photoresist is a tri-acrylate, its gelation threshold is 20% (see Eq. 5.1).

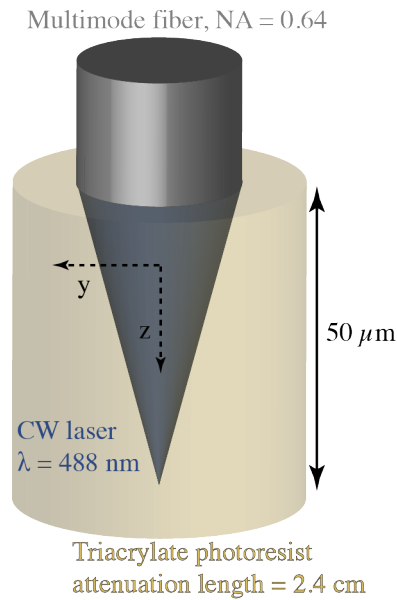


Figure A.3 – Simulation settings

A.4.2 Results

Simulation results reveal that the axial size of the photopolymerized volume increases linearly with time under non-inhibited conditions (see solid curves in Fig. A.4) whereas oxygen inhibition induces a non-linear axial growth of the voxel of polymer (see Fig. A.4). Figs. A.5, A.6 and A.7 allows comparing the extent of conversion of the polymer precursor into a polymer with and without oxygen inhibition.

Moreover, simulations showed that below a threshold power of ~ 100 nW, no photopolymerization occurs (see Fig. A.5(b)), which is consistent with the work of Maruo et al. [126]. Interestingly, the photopolymerization threshold that is theoretically determined is of the same order of magnitude as the one I experimentally measured (see section 5.2.2).

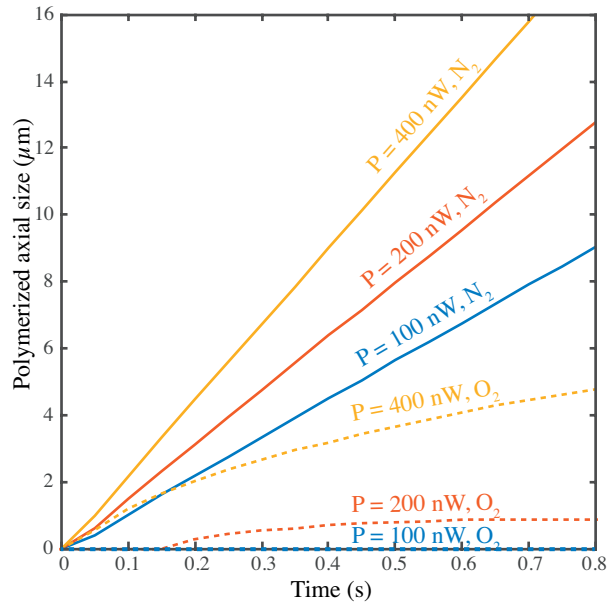
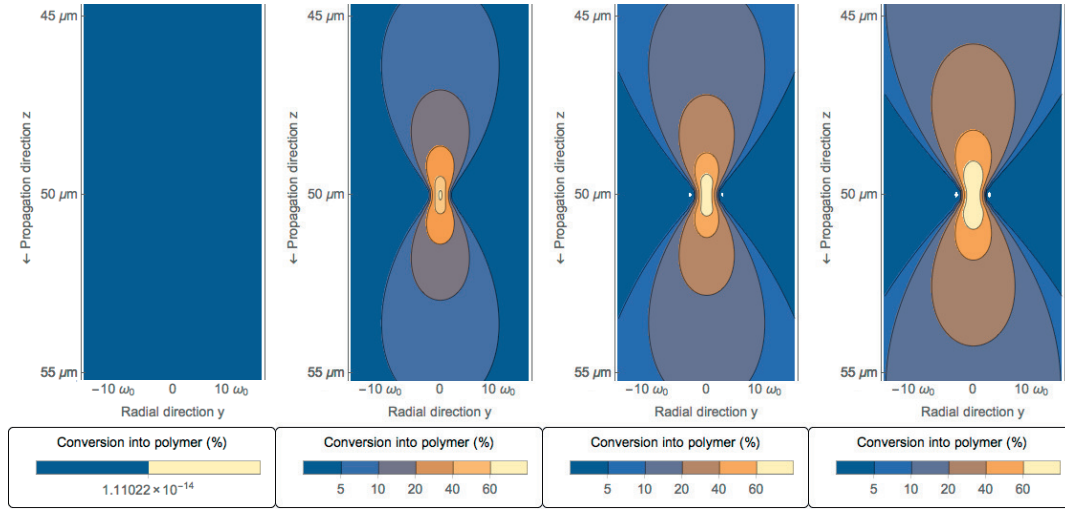
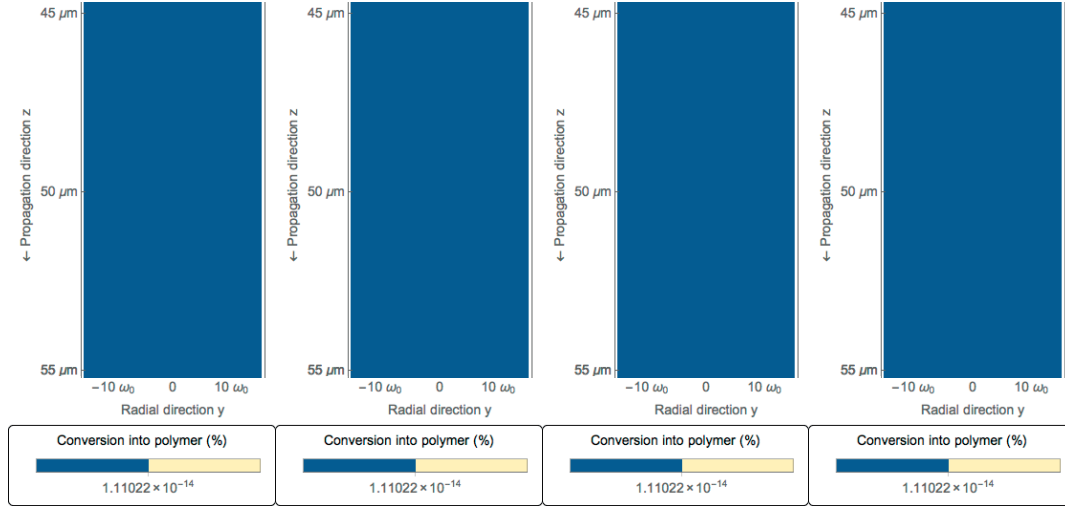


Figure A.4 – Non-linear inhibition of axial polymer growth, N_2 : simulations without oxygen inhibition, O_2 : simulations with oxygen inhibition

Appendix A. Modelization of oxygen-inhibited single-photon photopolymerization

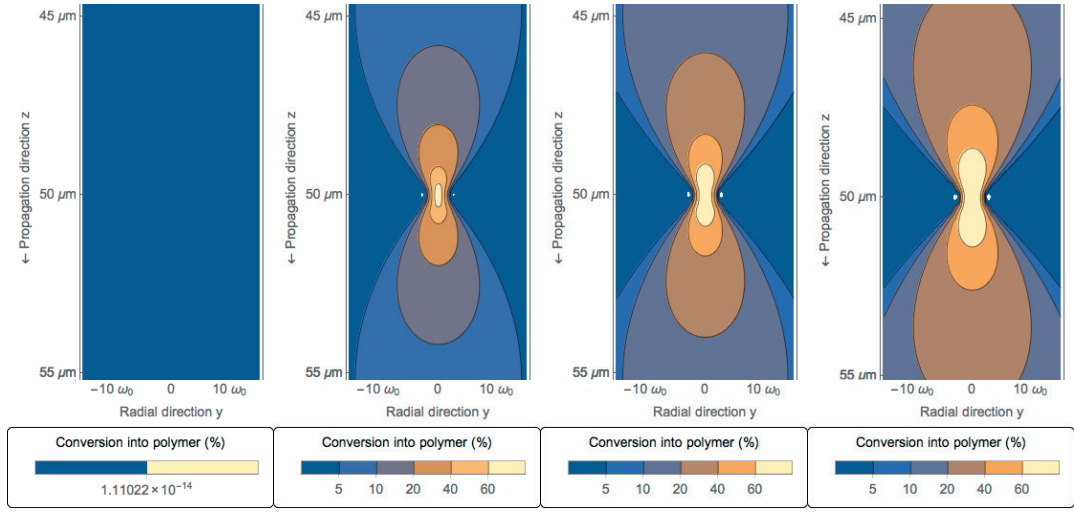


(a) Without oxygen inhibition

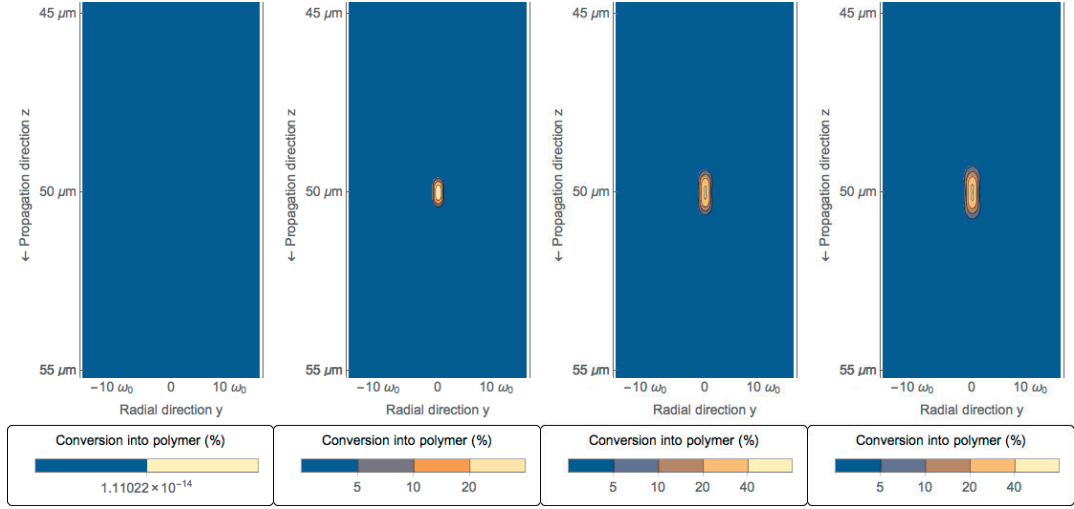


(b) With oxygen inhibition

Figure A.5 – Comparison of simulation results with and without oxygen inhibition for an optical power $P_{fiber} = 100$ nW at times $t = 0$ s, $t = 0.25$ s, $t = 0.5$ s, $t = 0.75$ s. The applied power is insufficient to overcome oxygen inhibition



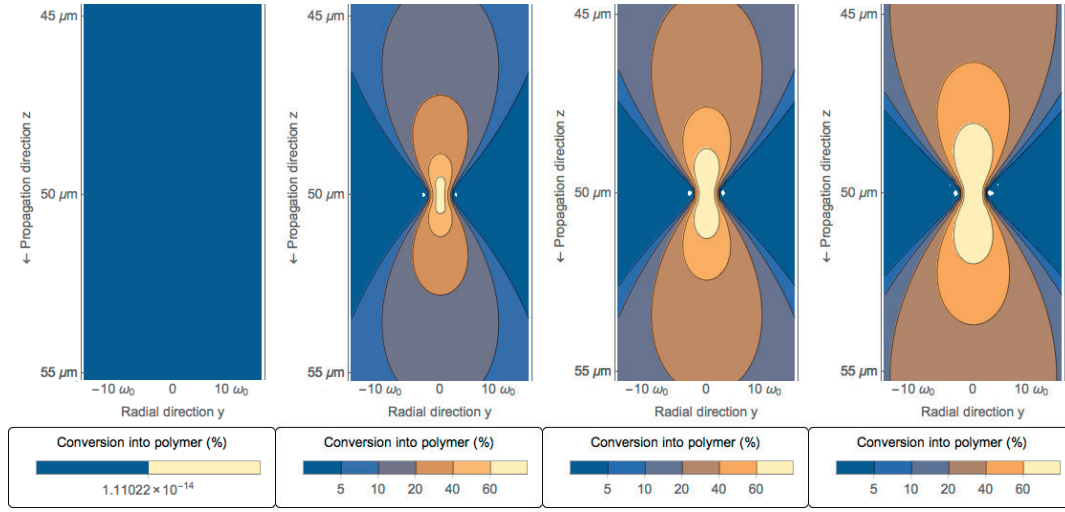
(a) Without oxygen inhibition



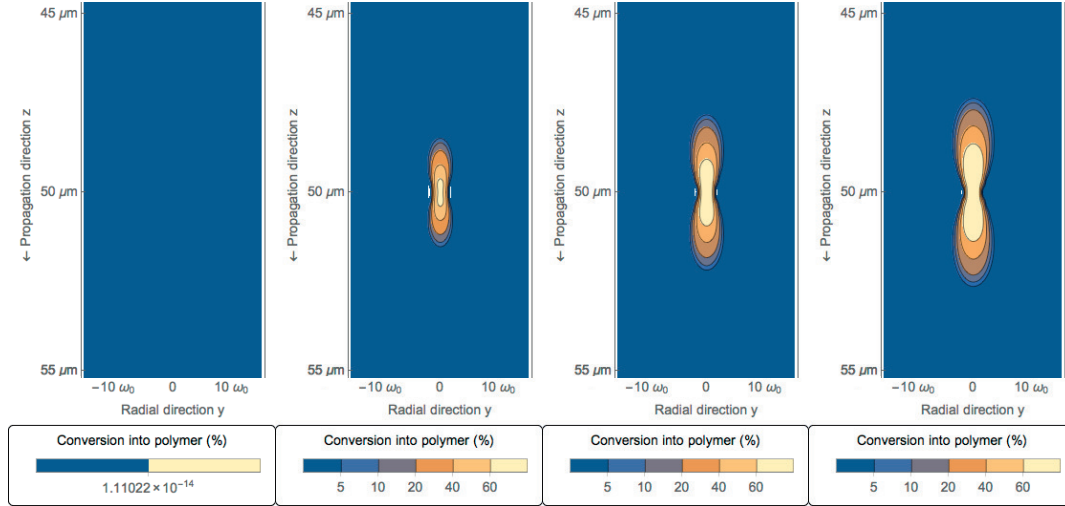
(b) With oxygen inhibition

Figure A.6 – Comparison of simulation results with and without oxygen inhibition for an optical power $P_{fiber} = 200$ nW at times $t = 0$ s, $t = 0.25$ s, $t = 0.5$ s, $t = 0.75$ s

Appendix A. Modelization of oxygen-inhibited single-photon photopolymerization



(a) Without oxygen inhibition



(b) With oxygen inhibition

Figure A.7 – Comparison of simulation results with and without oxygen inhibition for an optical power $P_{fiber} = 400 \text{ nW}$ at times $t = 0 \text{ s}$, $t = 0.25 \text{ s}$, $t = 0.5 \text{ s}$, $t = 0.75 \text{ s}$

Bibliography

- [1] F42 Committee. ISO/ASTM 52900:2015 (E) Standard terminology for Additive manufacturing - General principles - Terminology. ISO/ASTM International, 2016.
- [2] Hideo Kodama. Automatic method for fabricating a three-dimensional plastic model with photo-hardening polymer. *Review of Scientific Instruments*, 52(11):1770–1773, December 1981.
- [3] J C André, A Le Mehaute, and O De Witte. Dispositif pour réaliser un modèle de pièce industrielle. INPI, January 1986.
- [4] Charles W Hull. Apparatus for production of three-dimensional objects by stereolithography. US Patent Office, March 1986.
- [5] Ian Gibson, David Rosen, and Brent Stucker. *Additive manufacturing technologies: 3D printing, rapid prototyping, and direct digital manufacturing, second edition*. Springer New York, New York, NY, January 2015.
- [6] Terry T Wohlers and Wohlers Associates. *Wohlers Report 2014*. 3D Printing and Additive Manufacturing State of the Industry Annual Worldwide Progress Report. 2014.
- [7] Bertrand Guillotin and Fabien Guillemot. Cell patterning technologies for organotypic tissue fabrication. *Trends Biotechnol*, 29(4):183–190, March 2011.
- [8] Sean V Murphy and Anthony Atala. 3D bioprinting of tissues and organs. *Nat. Biotechnol.*, 32(8):773–785, July 2014.
- [9] F Guillemot, A Souquet, S Catros, B Guillotin, J Lopez, M Faucon, B Pippenger, R Bareille, M Rémy, S Bellance, P Chabassier, J C Fricain, and J Amédée. High-throughput laser printing of cells and biomaterials for tissue engineering. *Acta Biomater.*, 6(7):2494–2500, June 2010.
- [10] Tolga Ergin, Nicolas Stenger, Patrice Brenner, John B Pendry, and Martin Wegener. Three-dimensional invisibility cloak at optical wavelengths. *Science*, 328(5976):337–339, April 2010.
- [11] Joachim Fischer and Martin Wegener. Three-dimensional optical laser lithography beyond the diffraction limit. *Laser & Photonics Reviews*, 7(1):22–44, March 2012.

Bibliography

- [12] Timo Gissibl, Simon Thiele, Alois Herkommer, and Harald Giessen. Sub-micrometre accurate free-form optics by three-dimensional printing on single-mode fibres. *Nature Communications*, 7:11763, June 2016.
- [13] D W Hutmacher. Scaffolds in tissue engineering bone and cartilage. *Biomaterials*, 2000.
- [14] Barbara Spagnolo, Virgilio Brunetti, Godefroy Leménager, Elisa De Luca, Leonardo Sileo, Teresa Pellegrino, Pier Paolo Pompa, Massimo De Vittorio, and Ferruccio Pisanello. Three-dimensional cage-like microscaffolds for cell invasion studies. *Sci. Rep.*, 5:10531–10531, December 2014.
- [15] Willie Wu, Adam DeConinck, and Jennifer A Lewis. Omnidirectional Printing of 3D Microvascular Networks. *Adv. Mater.*, 23(24):H178–H183, March 2011.
- [16] Tapomoy Bhattacharjee, Steven M Zehnder, Kyle G Rowe, Suhani Jain, Ryan M Nixon, W Gregory Sawyer, and Thomas E Angelini. Writing in the granular gel medium. *Sci Adv*, 1(8):e1500655–e1500655, September 2015.
- [17] Thomas J Hinton, Quentin Jallerat, Rachelle N Palchesko, Joon Hyung Park, Martin S Grodzicki, Hao-Jan Shue, Mohamed H Ramadan, Andrew R Hudson, and Adam W Feinberg. Three-dimensional printing of complex biological structures by freeform reversible embedding of suspended hydrogels. *Sci Adv*, 1(9):e1500758–e1500758, September 2015.
- [18] D Helmer, A Voigt, S Wagner, N Keller, K Sachsenheimer, F Kotz, T M Nargang, and B E Rapp. Suspended Liquid Subtractive Lithography: One-step generation of 3D channel geometries in viscous curable polymer matrices. *Sci. Rep.*, 7(1):7387, December 2017.
- [19] Ryan L Truby and Jennifer A Lewis. Printing soft matter in three dimensions. *Nature*, 540(7633):371–378, December 2016.
- [20] Mohammad Vaezi, Hermann Seitz, and Shoufeng Yang. A review on 3D micro-additive manufacturing technologies. *Int. J. Adv. Manuf. Technol.*, 67(5-8):1721–1754, November 2012.
- [21] Markus Rimann, Epifania Bono, Helene Annaheim, Matthias Bleisch, and Ursula Graf-Hausner. Standardized 3D Bioprinting of Soft Tissue Models with Human Primary Cells. *Journal of Laboratory Automation*, 21(4):496–509, August 2016.
- [22] Matti Kesti, Michael Müller, Jana Becher, Matthias Schnabelrauch, Matteo D’Este, David Eglin, and Marcy Zenobi-Wong. A versatile bioink for three-dimensional printing of cellular scaffolds based on thermally and photo-triggered tandem gelation. *Acta Biomater.*, 11(1):162–172, January 2015.
- [23] Atabak Ghanizadeh Tabriz, Miguel A Hermida, Nicholas R Leslie, and Wenmiao Shu. Three-dimensional bioprinting of complex cell laden alginate hydrogel structures. *Bio-fabrication*, 7(4):045012, December 2015.

-
- [24] Ferry P W Melchels, Marco A N Domingos, Travis J Klein, Jos Malda, Paulo J Bartolo, and Dietmar W Hutmacher. Additive manufacturing of tissues and organs. *Progress in Polymer Science*, 37(8):1079–1104, August 2012.
- [25] Ian M Hutchings and Graham D Martin. *Inkjet Technology for Digital Fabrication*. John Wiley & Sons, November 2012.
- [26] Bert Huis In’T Veld, Ludger Overmeyer, Michael Schmidt, Konrad Wegener, Ajay Malshe, and Paulo Bartolo. Micro additive manufacturing using ultra short laser pulses. *CIRP Ann.*, 64(2):701–724, January 2015.
- [27] Ruitong Xiong, Zhengyi Zhang, Wenxuan Chai, Yong Huang, and Douglas B Chrisey. Freeform drop-on-demand laser printing of 3D alginate and cellular constructs. *Biofabrication*, 7(4):045011–14, December 2015.
- [28] Virginie Keriquel, Hugo Oliveira, Murielle Rémy, Sophia Ziane, Samantha Delmond, Benoit Rousseau, Sylvie Rey, Sylvain Catros, Joëlle Amédée, Fabien Guillemot, and Jean-Christophe Fricain. In situ printing of mesenchymal stromal cells, by laser-assisted bioprinting, for in vivo bone regeneration applications. *Sci. Rep.*, 7(1):1778, May 2017.
- [29] John R Tumbleston, David Shirvanyants, Nikita Ermoshkin, Rima Janusziewicz, Ashley R Johnson, David Kelly, Kai Chen, Robert Pinschmidt, Jason P Rolland, Alexander Ermoshkin, Edward T Samulski, and Joseph M DeSimone. Additive manufacturing. Continuous liquid interface production of 3D objects. *Science*, 347(6228):1349–1352, March 2015.
- [30] L M Robeson, E T Samulski, and A Ermoshkin. Continuous three dimensional fabrication from immiscible liquids. US Patent Office, 2015.
- [31] Paul Delrot, Miguel A Modestino, François Gallaire, Demetri Psaltis, and Christophe Moser. Inkjet Printing of Viscous Monodisperse Microdroplets by Laser-Induced Flow Focusing. *Phys. Rev. Applied*, 6(2):024003, August 2016.
- [32] Alvin U Chen and Osman A Basaran. A new method for significantly reducing drop radius without reducing nozzle radius in drop-on-demand drop production. *Phys. Fluids*, 14(1):L1–L4, 2002.
- [33] Brian H Cumpston, Sundaravel P Ananthavel, Stephen Barlow, Daniel L Dyer, Jeffrey E Ehrlich, Lael L Erskine, Ahmed A Heikal, Stephen M Kuebler, I Y Sandy Lee, Dianne McCord-Maughon, Jinqi Qin, Harald Ro ckel, Mariacristina Rumi, Xiang-Li Wu, Seth R Marder, and Joseph W Perry. Two-photon polymerization initiators for three-dimensional optical data storage and microfabrication. *Nature*, 398(6722):51–54, 1999.
- [34] J A Lewis. Direct Ink Writing of 3D Functional Materials. *Adv. Funct. Mater.*, 16(17):2193–2204, November 2006.

Bibliography

- [35] Nanoscribe GmbH. Photonic Professional GT. Technical report, December 2016.
- [36] Tommaso Baldacchini. *Three-Dimensional Microfabrication Using Two-Photon Polymerization*. Fundamentals, Technology, and Applications. William Andrew, September 2015.
- [37] Zhiquan Li, Jan Torgersen, Aliasghar Ajami, Severin Mühleder, Xiaohua Qin, Wolfgang Husinsky, Wolfgang Holnthoner, Aleksandr Ovsianikov, Jürgen Stampfl, and Robert Liska. Initiation efficiency and cytotoxicity of novel water-soluble two-photon photoinitiators for direct 3D microfabrication of hydrogels. *RSC Adv.*, 3(36):15939–8, 2013.
- [38] EOS. EOS P 500 specification sheet. pages 1–2, November 2017.
- [39] Formlabs. Fuse 1 - Technical specifications. pages 1–4, June 2017.
- [40] Robert van Lith, Evan Baker, Henry Ware, Jian Yang, Adam Cyrus Farsheed, Cheng Sun, and Guillermo Ameer. 3D-Printing Strong High-Resolution Antioxidant Bioresorbable Vascular Stents. *Adv. Mater. Technol.*, 1(9):1600138, October 2016.
- [41] Frederik Kotz, Karl Arnold, Werner Bauer, Dieter Schild, Nico Keller, Kai Sachsenheimer, Tobias M Nargang, Christiane Richter, Dorothea Helmer, and Bastian E Rapp. Three-dimensional printing of transparent fused silica glass. *Nature Publishing Group*, 544(7):337–339, April 2017.
- [42] Martin Schwentenwein and Johannes Homa. Additive Manufacturing of Dense Alumina Ceramics. *Int. J. Appl. Ceram. Technol.*, 12(1):1–7, September 2014.
- [43] Eric MacDonald and Ryan Wicker. Multiprocess 3D printing for increasing component functionality. *Science*, 353(6307), September 2016.
- [44] Ioannis N Papadopoulos, Salma Farahi, Christophe Moser, and Demetri Psaltis. Focusing and scanning light through a multimode optical fiber using digital phase conjugation. *Opt. Express*, 20(10):10583–10590, May 2012.
- [45] Damien Loterie, Salma Farahi, Ioannis Papadopoulos, Alexandre Goy, Demetri Psaltis, and Christophe Moser. Digital confocal microscopy through a multimode fiber. *Opt. Express*, 23(18):23845–23858, September 2015.
- [46] Yoshiyuki Tagawa, Nikolai Oudalov, Claas Willem Visser, Ivo R Peters, Devaraj van der Meer, Chao Sun, Andrea Prosperetti, and Detlef Lohse. Highly Focused Supersonic Microjets. *Phys. Rev. X*, 2(3):031002, July 2012.
- [47] Yoshiyuki Tagawa, Nikolai Oudalov, A El Ghalbzouri, Chao Sun, and Detlef Lohse. Needle-free injection into skin and soft matter with highly focused microjets. *Lab Chip*, 13(7):1357–1363, 2013.

-
- [48] M Duocastella, J M Fernández-Pradas, J L Morenza, and P Serra. Time-resolved imaging of the laser forward transfer of liquids. *J. Appl. Phys.*, 106(8):084907–084907, October 2009.
- [49] Christos Boutopoulos, Ioannis Kalpyris, Efthymis Serpetzoglou, and Ioanna Zergioti. Laser-induced forward transfer of silver nanoparticle ink: time-resolved imaging of the jetting dynamics and correlation with the printing quality. *Microfluid Nanofluid*, 16(3):493–500, August 2013.
- [50] Jason A Barron, David B Krizman, and Bradley R Ringeisen. Laser printing of single cells: Statistical analysis, cell viability, and stress. *Ann Biomed Eng*, 33(2):121–130, February 2005.
- [51] Lothar Koch, Andrea Deiwick, Sabrina Schlie, Stefanie Michael, Martin Gruene, Vincent Coger, Daniela Zychlinski, Axel Schambach, Kerstin Reimers, Peter M Vogt, and Boris Chichkov. Skin tissue generation by laser cell printing. *Biotechnol. Bioeng.*, 109(7):1855–1863, June 2012.
- [52] Sylvain Catros, Bertrand Guillotin, Markéta Bačáková, Jean-Christophe Fricain, and Fabien Guillemot. Effect of laser energy, substrate film thickness and bioink viscosity on viability of endothelial cells printed by Laser-Assisted Bioprinting. *Applied Surface Science*, 257(12):5142–5147, December 2010.
- [53] J A Barron, P Wu, H D Ladouceur, and B R Ringeisen. Biological laser printing: a novel technique for creating heterogeneous 3-dimensional cell patterns. *Biomed Microdevices*, 6(2):139–147, June 2004.
- [54] Emeline Pages, Murielle Rémy, Virginie Keriquel, Manuela Medina Correa, Bertrand Guillotin, and Fabien Guillemot. Creation of Highly Defined Mesenchymal Stem Cell Patterns in Three Dimensions by Laser-Assisted Bioprinting. *Journal of Nanotechnology in Engineering and Medicine*, 6(2):021005, May 2015.
- [55] Alexander Ya Malkin and Avraam I Isayev. *Rheology: Concepts, methods, and applications: Second edition*. Elsevier, A.V.Topchiev Institute of Petrochemical Synthesis, RAS, Moscow, Russian Federation, January 2011.
- [56] B J de Gans, P C Duineveld, and U S Schubert. Inkjet Printing of Polymers: State of the Art and Future Developments. *Adv. Mater.*, 16(3):203–213, February 2004.
- [57] Steven T J Peng and Robert F Landel. Rheological behavior of progressively shear-thickening solutions. *J. Appl. Phys.*, 52(1):5988–5993, October 1981.
- [58] Brian Derby. Inkjet Printing of Functional and Structural Materials: Fluid Property Requirements, Feature Stability, and Resolution. *Annu. Rev. Mater. Res.*, 40(1):395–414, June 2010.

Bibliography

- [59] Daehwan Jang, Dongjo Kim, and Jooho Moon. Influence of fluid physical properties on ink-jet printability. *Langmuir*, 25(5):2629–2635, March 2009.
- [60] A A Castrejón-Pita, J R Castrejón-Pita, and G D Martin. A novel method to produce small droplets from large nozzles. *Rev Sci Instrum*, 83(11):115105–115105, November 2012.
- [61] Zhengyi Zhang, Ruitong Xiong, Renwei Mei, Yong Huang, and Douglas B Chrisey. Time-Resolved Imaging Study of Jetting Dynamics during Laser Printing of Viscoelastic Alginate Solutions. *Langmuir*, 31(23):6447–6456, June 2015.
- [62] Emre Turkoz, Antonio Perazzo, Hyoungsoo Kim, Howard A Stone, and Craig B Arnold. Impulsively Induced Jets from Viscoelastic Films for High-Resolution Printing. *Phys. Rev. Lett.*, 120(7):074501, February 2018.
- [63] C Wagner, Y Amarouchene, D Bonn, and J Eggers. Droplet detachment and satellite bead formation in viscoelastic fluids. *Phys. Rev. Lett.*, 95(16):164504(4).
- [64] P Serra, M Duocastella, J M Fernández-Pradas, and J L Morenza. Liquids microprinting through laser-induced forward transfer. *Applied Surface Science*, 255(10):5342–5345, March 2009.
- [65] Craig B Arnold, Pere Serra, and Alberto Piqué. Laser Direct-Write Techniques for Printing of Complex Materials. *MRS Bulletin*, 32(01):23–32, 2007.
- [66] Bertrand Guillotin, Agnès Souquet, Sylvain Catros, Martí Duocastella, Benjamin Pippenger, Séverine Bellance, Reine Bareille, Murielle Rémy, Laurence Bordenave, Joëlle Amédée, and Fabien Guillemot. Laser assisted bioprinting of engineered tissue with high cell density and microscale organization. *Biomaterials*, 31(28):7250–7256, September 2010.
- [67] Bertrand Guillotin, Sylvain Catros, and Fabien Guillemot. Laser Assisted Bio-printing (LAB) of Cells and Bio-materials Based on Laser Induced Forward Transfer (LIFT). In *Laser Technology in Biomimetics*, pages 193–209. Springer Berlin Heidelberg, Berlin, Heidelberg, January 2014.
- [68] Raphaël Devillard, Emeline Pages, Manuela Medina Correa, Virginie Keriquel, Murielle Rémy, Jérôme Kalisky, Muhammad Ali, Bertrand Guillotin, and Fabien Guillemot. Cell patterning by laser-assisted bioprinting. In *Methods Cell Biol.*, pages 159–174. Elsevier, January 2014.
- [69] Nurazhani Abdul Raof, Nathan R Schiele, Yubing Xie, Douglas B Chrisey, and David T Corr. The maintenance of pluripotency following laser direct-write of mouse embryonic stem cells. *Biomaterials*, 32(7):1802–1808, February 2011.
- [70] Simon Young, Mark Wong, Yasuhiko Tabata, and Antonios G Mikos. Gelatin as a delivery vehicle for the controlled release of bioactive molecules. In *J Control Release*, pages 256–274. Rice University, Houston, United States, December 2005.

-
- [71] T Kato, T Arafune, T Washio, A Nakagawa, Y Ogawa, T Tominaga, I Sakuma, and E Kobayashi. Mechanics of the injected pulsejet into gelatin gel and evaluation of the effect by puncture and crack generation and growth. *J. Appl. Phys.*, 116(7), 2014.
- [72] Viren Menezes, Satyam Kumar, and Kazuyoshi Takayama. Shock wave driven liquid microjets for drug delivery. *J. Appl. Phys.*, 106(8):086102–086102–3, October 2009.
- [73] X H Wang, Y N Yan, Y Q Pan, Z Xiong, H X Liu, B Cheng, F Liu, F Lin, R D Wu, R J Zhang, and Q P Lu. Generation of three-dimensional hepatocyte/gelatin structures with rapid prototyping system. *Tissue Eng.*, 12(1):83–90, January 2006.
- [74] Chloe N Grover, Ruth E Cameron, and Serena M Best. Investigating the morphological, mechanical and degradation properties of scaffolds comprising collagen, gelatin and elastin for use in soft tissue engineering. *Journal of the Mechanical Behavior of Biomedical Materials*, 10:62–74, June 2012.
- [75] Lena Möller, Andreas Krause, Julia Dahlmann, Ina Gruh, Andreas Kirschning, and Gerald Dräger. Preparation and evaluation of hydrogel-composites from methacrylated hyaluronic acid, alginate, and gelatin for tissue engineering. *International Journal of Artificial Organs*, 34(2):93–102, February 2011.
- [76] Stephan Preibisch, Stephan Saalfeld, and Pavel Tomancak. Globally optimal stitching of tiled 3D microscopic image acquisitions. *Bioinformatics*, 25(11):1463–1465, June 2009.
- [77] V Dinca, A Patrascioiu, J M Fernández-Pradas, J L Morenza, and P Serra. Influence of solution properties in the laser forward transfer of liquids. *Applied Surface Science*, 258(23):9379–9384, September 2012.
- [78] Thomas Braschler, Ana Valero, Ludovica Colella, Kristopher Pataky, Jürgen Brugger, and Philippe Renaud. Link between alginate reaction front propagation and general reaction diffusion theory. *Anal. Chem.*, 83(6):2234–2242, March 2011.
- [79] Joy Baxter and Samir Mitragotri. Jet-induced skin puncture and its impact on needle-free jet injections: Experimental studies and a predictive model. *J Control Release*, 106(3):361–373, September 2005.
- [80] Yasunari Michinaka and Samir Mitragotri. Delivery of polymeric particles into skin using needle-free liquid jet injectors. *J Control Release*, 153(3):249–254, August 2011.
- [81] Stéphane Roger, Yan Yip Cheung Sang, Agnès Bee, Régine Perzynski, Jean Marc Di Meglio, and Alain Ponton. Structural and multi-scale rheophysical investigation of diphasic magneto-sensitive materials based on biopolymers. *Eur Phys J E Soft Matter*, 38(8):88, August 2015.
- [82] S Mitragotri. Innovation - Current status and future prospects of needle-free liquid jet injectors. *Nat Rev Drug Discov*, 5(7):543–548, July 2006.

Bibliography

- [83] Taehwa Lee, Hyoung Won Baac, Jong G Ok, Hong Seok Youn, and L Jay Guo. Nozzle-Free Liquid Microjetting via Homogeneous Bubble Nucleation. *Phys. Rev. Applied*, 3(4):044007, April 2015.
- [84] A Piqué, R Auyeung, J Fitzgerald, and D B Chrisey. Direct-write laser transfer and processing. US Patent Office, 2006.
- [85] D Munoz-Martin, C F Brasz, Y Chen, M Morales, C B Arnold, and C Molpeceres. Laser-induced forward transfer of high-viscosity silver pastes. *Appl. Surf. Sci.*, 366:389–396, March 2016.
- [86] Ivo R Peters, Yoshiyuki Tagawa, Nikolai Oudalov, Chao Sun, Andrea Prosperetti, Detlef Lohse, and Devaraj van der Meer. Highly focused supersonic microjets: numerical simulations. *J. Fluid Mech.*, 719:587–605, March 2013.
- [87] Nick R Glass, Ricky Tjeung, Peggy Chan, Leslie Y Yeo, and James R Friend. Organosilane deposition for microfluidic applications. *Biomicrofluidics*, 5(3):036501–036507, 2011.
- [88] Pierre-Gilles de Gennes, Françoise Brochard-Wyart, and David Quéré. Capillarity and Gravity. In *Capillarity and Wetting Phenomena*, pages 33–67. Springer New York, New York, NY, 2004.
- [89] Nian-Sheng Cheng. Formula for the Viscosity of a Glycerol–Water Mixture. *Ind. Eng. Chem. Res.*, 47(9):3285–3288, May 2008.
- [90] A Antkowiak, N Bremond, S Le Dizès, and E Villermaux. Short-term dynamics of a density interface following an impact. *J. Fluid Mech.*, 577:241–250, April 2007.
- [91] Raymond Bergmann, Erik de Jong, Jean-Baptiste Choimet, Devaraj van der Meer, and Detlef Lohse. The origin of the tubular jet. *J. Fluid Mech.*, 600:19–43, March 2008.
- [92] Fan-Gang Tseng, Chang-Jin Kim, and Chih-Ming Ho. A high-resolution high-frequency monolithic top-shooting microinjector free of satellite drops - part I: concept, design, and model. *J. Microelectromech. Syst.*, 11(5):427–436, October 2002.
- [93] Stephen D Hoath, Sungjune Jung, Wen-Kai Hsiao, and Ian M Hutchings. How PE-DOT:PSS solutions produce satellite-free inkjets. *Organic Electronics*, 13(12):3259–3262, December 2012.
- [94] Heather J Shore and Graham M Harrison. The effect of added polymers on the formation of drops ejected from a nozzle. *Phys. Fluids*, 17(3):033104–033104, 2005.
- [95] Martin Gruene, Claudia Unger, Lothar Koch, Andrea Deiwick, and Boris Chichkov. Dispensing pico to nanolitre of a natural hydrogel by laser-assisted bioprinting. *Biomed Eng Online*, 10:19–19, December 2010.
- [96] S D Hoath, S Jung, and I M Hutchings. A simple criterion for filament break-up in drop-on-demand inkjet printing. *Phys. Fluids*, 25(2):021701–021706, 2013.

-
- [97] Eric Lee. *Microdrop Generation*, volume 5 of *Nano- and Microscience, Engineering, Technology and Medicine*. CRC Press, December 2002.
- [98] Osman A Basaran, Haijing Gao, and Pradeep P Bhat. Nonstandard Inkjets. *Annu. Rev. Fluid Mech.*, 45(1):85–113, January 2013.
- [99] Y Amarouchene, D Bonn, J Meunier, and H Kellay. Inhibition of the Finite-Time Singularity during Droplet Fission of a Polymeric Fluid. *Phys. Rev. Lett.*, 86(16):3558–3561, April 2001.
- [100] M Duocastella, J M Fernández-Pradas, J L Morenza, D Zafra, and P Serra. Novel laser printing technique for miniaturized biosensors preparation. *Sensors and Actuators B: Chemical*, 145(1):596–600, March 2010.
- [101] Chao Sun, Edip Can, Rory Dijkink, Detlef Lohse, and Andrea Prosperetti. Growth and collapse of a vapour bubble in a microtube: The role of thermal effects. *J. Fluid Mech.*, 632:5–16, September 2009.
- [102] Xiaofeng Cui, Delphine Dean, Zaverio M Ruggeri, and Thomas Boland. Cell Damage Evaluation of Thermal Inkjet Printed Chinese Hamster Ovary Cells. *Biotechnol. Bioeng.*, 106(6):963–969, 2010.
- [103] Martin Plöschner, Tomáš Tyc, and Tomáš Čižmár. Seeing through chaos in multimode fibres. *Nature Photon*, 9(8):529–535, August 2015.
- [104] P A Quinto-Su, V Venugopalan, and C D Ohl. Generation of laser-induced cavitation bubbles with a digital hologram. *Opt. Express*, 16(23):18964–18969, November 2008.
- [105] George Odian. *Principles of Polymerization*. John Wiley & Sons, 2004.
- [106] Aparna Boddapati, Santosh B Rahane, Ryan P Slopek, Victor Breedveld, Clifford L Henderson, and Martha A Grover. Gel time prediction of multifunctional acrylates using a kinetics model. *Polymer (Guildf)*, 52(3):866–873, December 2010.
- [107] P J Flory. Constitution of Three-dimensional Polymers and the Theory of Gelation. *The Journal of Physical Chemistry*, 46(1):132–140, 1942.
- [108] Paulo Jorge Bártolo. *Stereolithography. Materials, Processes and Applications*. Springer Science & Business Media, March 2011.
- [109] M Thiel, J Fischer, G von Freymann, and M Wegener. Direct laser writing of three-dimensional submicron structures using a continuous-wave laser at 532 nm. *Appl. Phys. Lett.*, 97(22):221102, November 2010.
- [110] John T Fourkas and John S Petersen. 2-Colour photolithography. *Phys. Chem. Chem. Phys.*, 16(19):8731–8750, May 2014.

Bibliography

- [111] Xiaowen Wan and Rajesh Menon. Proximity-effect correction for 3D single-photon optical lithography. *Applied Optics*, 55(3):A1–A7, January 2016.
- [112] S Maruo, O Nakamura, and S Kawata. Three-dimensional microfabrication with two-photon-absorbed photopolymerization. *Opt. Lett.*, 22(2):132–134, 1997.
- [113] Judith K Hohmann, Michael Renner, Erik H Waller, and Georg von Freymann. Three-Dimensional μ -Printing: An Enabling Technology. *Advanced Optical Materials*, 3(11):1488–1507, November 2015.
- [114] Milosz Pawlicki, Hazel A Collins, Robert G Denning, and Harry L Anderson. Two-photon absorption and the design of two-photon dyes. *Angew. Chem. Int. Ed.*, 48(18):3244–3266, April 2009.
- [115] Guang S He, Loon-Seng Tan, Qingdong Zheng, and Paras N Prasad. Multiphoton absorbing materials: molecular designs, characterizations, and applications. *Chem. Rev.*, 108(4):1245–1330, March 2008.
- [116] Jin-Feng Xing, Mei-Ling Zheng, and Xuan-Ming Duan. Two-photon polymerization microfabrication of hydrogels: an advanced 3D printing technology for tissue engineering and drug delivery. *Chem. Soc. Rev.*, 44(15):5031–5039, August 2015.
- [117] Hong-Bo Sun and Satoshi Kawata. Two-Photon Photopolymerization and 3D Lithographic Microfabrication. In *NMR 3D Analysis Photopolymerization*, pages 169–273. Springer Berlin Heidelberg, Berlin, Heidelberg, September 2006.
- [118] Jin-Feng Xing, Xian-Zi Dong, Wei-Qiang Chen, Xuan-Ming Duan, Nobuyuki Takeyasu, Takuo Tanaka, and Satoshi Kawata. Improving spatial resolution of two-photon microfabrication by using photoinitiator with high initiating efficiency. *Appl. Phys. Lett.*, 90(13):131106, April 2007.
- [119] Timothy F Scott, Benjamin A Kowalski, Amy C Sullivan, Christopher N Bowman, and Robert R McLeod. Two-color single-photon photoinitiation and photoinhibition for subdiffraction photolithography. *Science*, 324(5929):913–917, May 2009.
- [120] Darren L Forman, Michael C Cole, and Robert R McLeod. Radical diffusion limits to photoinhibited superresolution lithography. *Phys. Chem. Chem. Phys.*, 15(36):14862–14867, September 2013.
- [121] J Arlt and M J Padgett. Generation of a beam with a dark focus surrounded by regions of higher intensity: the optical bottle beam. *Opt. Lett.*, 25(4):191–193, February 2000.
- [122] Harikrishnan Vijayamohanan, Edmund F Palermo, and Chaitanya K Ullal. Spirothiopyran-Based Reversibly Saturable Photoresist. *Chemistry of Materials*, 29(11):4754–4760, May 2017.
- [123] Patrick Mueller, Michael Thiel, and Martin Wegener. 3D direct laser writing using a 405 nm diode laser. *Opt. Lett.*, 39(24):6847–6850, December 2014.

-
- [124] Mai Trang Do, Thi Thanh Ngan Nguyen, Qinggele Li, Henri Benisty, Isabelle Ledoux-Rak, and Ngoc Diep Lai. Submicrometer 3D structures fabrication enabled by one-photon absorption direct laser writing. *Opt. Express*, 21(18):20964–20973, September 2013.
- [125] Dam Thuy Trang Nguyen, Quang Cong Tong, Isabelle Ledoux-Rak, and Ngoc Diep Lai. One-step fabrication of submicrostructures by low one-photon absorption direct laser writing technique with local thermal effect. *J. Appl. Phys.*, 119(1):013101, January 2016.
- [126] Shoji Maruo and Koji Ikuta. Three-dimensional microfabrication by use of single-photon-absorbed polymerization. *Appl. Phys. Lett.*, 76(1):2656, May 2000.
- [127] Makoto Horiyama, Hong-Bo Sun, Masafumi Miwa, Shigeki Matsuo, and Hiroaki Misawa. Three-Dimensional Microstructures Created by Laser Microfabrication Technology. *Jpn. J. Appl. Phys.*, 38(2):L212–L215, February 1999.
- [128] Quang Cong Tong, Dam Thuy Trang Nguyen, Minh Thanh Do, Mai Hoang Luong, Bernard Journet, Isabelle Ledoux-Rak, and Ngoc Diep Lai. Direct laser writing of polymeric nanostructures via optically induced local thermal effect. *Appl. Phys. Lett.*, 108(18):183104, 2016.
- [129] Joachim Fischer, Jonathan B Mueller, Johannes Kaschke, Thomas J A Wolf, Andreas-Neil Unterreiner, and Martin Wegener. Three-dimensional multi-photon direct laser writing with variable repetition rate. *Opt. Express*, 21(22):26244–26260, November 2013.
- [130] Jonathan B Mueller, Joachim Fischer, Frederik Mayer, Muamer Kadic, and Martin Wegener. Polymerization kinetics in three-dimensional direct laser writing. *Adv. Mater.*, 26(38):6566–6571, September 2014.
- [131] Mangirdas Malinauskas, Albertas Zukauskas, Gabija Bickauskaite, Roaldas Gadonas, and Saulius Juodkazis. Mechanisms of three-dimensional structuring of photo-polymers by tightly focussed femtosecond laser pulses. *Opt. Express*, 18(10):10209–10221, May 2010.
- [132] Sascha Engelhardt, Jenny Tempeler, Arnold Gillner, and Martin Wehner. The voxel onset time as a method for the evaluation of two photon lithography. *JLMN*, 8(3):230–233, December 2013.
- [133] Ulf Schnars and Werner P O Jüptner. REVIEW ARTICLE: Digital recording and numerical reconstruction of holograms. *Measurement Science and Technology*, 13(9):85–R101, September 2002.
- [134] Z Monemhaghdoost. *Broadband Digital Holographic Camera for Microscopy*. PhD thesis, Lausanne, 2015.
- [135] Tomáš Čižmár and Kishan Dholakia. Exploiting multimode waveguides for pure fibre-based imaging. *Nature Communications*, 3:1027–1027, August 2012.

Bibliography

- [136] Youngwoon Choi, Changhyeong Yoon, Moonseok Kim, Taeseok Daniel Yang, Christopher Fang-Yen, Ramachandra R Dasari, Kyoung Jin Lee, and Wonshik Choi. Scanner-free and wide-field endoscopic imaging by using a single multimode optical fiber. *Phys. Rev. Lett.*, 109(20):203901, November 2012.
- [137] Damien Loterie, Sebastianus A Goorden, Demetri Psaltis, and Christophe Moser. Confocal microscopy through a multimode fiber using optical correlation. *Opt. Lett.*, 40(24):5754–5757, December 2015.
- [138] DCM Loterie. *Microscopy and digital light shaping through optical fibers*. PhD thesis, EPFL, Lausanne, 2017.
- [139] S M Popoff, G Lerosey, M Fink, A C Boccara, and S Gigan. Controlling light through optical disordered media: transmission matrix approach. *New Journal of Physics*, 13(1):123021, December 2011.
- [140] Edgar E Morales-Delgado, Loic Urio, Donald B Conkey, Nicolino Stasio, Demetri Psaltis, and Christophe Moser. Three-dimensional microfabrication through a multimode optical fiber. *Opt. Express*, 25(6):7031, 2017.
- [141] Philip Zupancic, Philipp M Preiss, Ruichao Ma, Alexander Lukin, M Eric Tai, Matthew Rispoli, Rajibul Islam, and Markus Greiner. Ultra-precise holographic beam shaping for microscopic quantum control. *Opt. Express*, 24(13):13881–13893, June 2016.
- [142] Shoji Maruo and Koji Ikuta. Submicron stereolithography for the production of freely movable mechanisms by using single-photon polymerization. *Sensors and Actuators A: Physical*, 100(1):70–76, August 2002.
- [143] Michael Thiel and Martin Hermatschweiler. Three-dimensional laser lithography. *Optik & Photonik*, 6(4):36–39, December 2011.
- [144] A Bertsch, H Lorenz, and P Renaud. 3D microfabrication by combining microstereolithography and thick resist UV lithography. *Sensors and Actuators A: Physical*, 73(1-2):14–23, March 1999.
- [145] M P Lee, G J T Cooper, T Hinkley, G M Gibson, M J Padgett, and L Cronin. Development of a 3D printer using scanning projection stereolithography. *Sci. Rep.*, 5:9875, 2015.
- [146] Jason Daniel Schmidt. *Numerical Simulation of Optical Wave Propagation with Examples in MATLAB*. Society of Photo Optical, 2010.
- [147] T Haist, M Schonleber, and H J Tiziani. Computer-generated holograms from 3D-objects written on twisted-nematic liquid crystal displays. *Optics Communications*, 140(4-6):299–308, 1997.

- [148] G Sinclair, J Leach, P Jordan, G Gibson, E Yao, Z J Laczik, M J Padgett, and J Courtial. Interactive application in holographic optical tweezers of a multi-plane Gerchberg-Saxton algorithm for three-dimensional light shaping. *Opt. Express*, 12(8):1665–1670, 2004.
- [149] Bahaa E A Saleh and Malvin Carl Teich. *Fundamentals of Photonics*. John Wiley & Sons, February 2013.
- [150] Yin-Chu Chen, Jack L Ferracane, and Scott A Prahl. Quantum yield of conversion of the photoinitiator camphorquinone. 23(6):655–664, December 2006.
- [151] Christian Decker. Recent developments in photoinitiated radical polymerization. In *Macromolecular Symposia*, pages 45–63. Universite de Haute Alsace, Mulhouse, France, December 1999.
- [152] Dhananjay Dendukuri, Priyadarshi Panda, Ramin Haghgooie, Ju Min Kim, T Alan Hatton, and Patrick S Doyle. Modeling of Oxygen-Inhibited Free Radical Photopolymerization in a PDMS Microfluidic Device. *Macromolecules*, 41:8547–8556, November 2008.

Paul Delrot

Address EPFL STI IMT LAPD, BM4109
Station 17
CH-1015, Lausanne
Switzerland

Phone +41 79 525 58 06

Email paul.delrot@epfl.ch

Date of birth May 10, 1991

Professional experience

PhD Candidate – Laboratory of Applied Photonics Devices, EPFL Oct. 2014 - July 2018 (exp.)

Lausanne, Switzerland

Investigating new technologies for compact and high-resolution 3D printing with a focus on photopolymers and ways to deliver light through multimode optical fibers. Supervisor: Prof. Christophe Moser.

Engineer in Optics, OPTIS Northern Europe

Jan. 2014 - Sept. 2014

Warrington, United Kingdom

At the north European subsidiary of OPTIS, my missions were:

- Designing non-imaging and imaging optics, mainly for the lighting and automotive industry (Aston Martin Lagonda, Jaguar, Bentley) using the lighting simulation software SPEOS developed by OPTIS (software integrated in the CAD environment of CATIA V5, Solidworks, NX and ProEngineer),
- Analysing existing optical systems and optimizing them,
- Realizing pilot studies for the new customers.

Master's Thesis at the Vision Institute, INSERM

July 2013 - Nov. 2013

Paris, France

Designing (under Zemax and LightTools), mounting and testing an optical system for combined imaging and patterned stimulation of the rodent's eye to assess vision restoration by optogenetic therapy. Supervisor : Dr. Émilie Macé.

Internship at THALES Underwater Systems-ISEN

May 2012 - Aug. 2012

Brest, France

Investigating the potential of polarimetric imaging in underwater imaging.

Language and computer skills

Languages

English (full working proficiency), French (mother tongue), Swedish (limited working proficiency), German (beginner)

Softwares

Matlab, LightTools , Zemax, CATIA V5, NX, ProEngineer, SolidWorks, OSLO, SPEOS, MS Office, Image J,

LaTeX.

Computer Science

Solid skills in Matlab, C programming and Mathematica, good skills in C++ and Arduino programming.

Education

PhD in Photonics

Oct. 2014 - July 2018 (exp.)

École polytechnique fédérale de Lausanne (EPFL), Switzerland

Research on micro-additive manufacturing.

Engineer's degree in Optics (valedictorian on year 1 & 2)

Sept. 2010 - Dec. 2013

Institut d'Optique Graduate School (IOGS), Palaiseau, France

The Institut d'Optique has provided me with advanced skills in both Optics and Engineering as well as in numerous domains of Physics dealing with Optics such as: optical design, photometry, radiometry, optical physics, thin film principles, semiconductors, laser diodes, electronics, signal&image processing, fiber optics, interferometry, quantum mechanics.

Master of Science in Engineering Physics (Results: A+)

Aug. 2012 - Dec. 2013

Royal Institute of Technology (KTH), Stockholm, Sweden

During an international exchange, I could extend my knowledge in: X-ray Physics, detectors of radiation and medical imaging systems, physics and engineering of lasers, spectroscopy, experimental methods for biomolecular studies, biomedicine, biocellular physics, technical English.

List of publications

Peer-reviewed articles

Delrot, P., Loterie, D., Psaltis, D. & Moser, C. Single-photon three-dimensional microfabrication through a multimode optical fiber. *Opt. Express* **26**, 1766–1778 (2018).

Delrot, P., Modestino, M. A., Gallaire, F., Psaltis, D. & Moser, C. Inkjet Printing of Viscous Monodisperse Microdroplets by Laser-Induced Flow Focusing. *Phys. Rev. Applied* **6**, 024003 (2016).

Dubreuil, M., Delrot P., Leonard I., Alfalou A., Brosseau C., Dogariu A. Exploring underwater target detection by imaging polarimetry and correlation techniques. *Applied Optics* **52**, 997–1005 (2013).

Conference papers and talks

Delrot P., Loterie D., Psaltis D., and Moser C., "Single-photon micro-additive manufacturing through a multimode optical fiber", Photonics West 2018, San Francisco, USA, LASE conference, session on "Laser 3D Manufacturing V", (31/01/2018).

Delrot P., Hauser S.P., Krizek J., and Moser C. "Extending the printing capabilities of laser-induced forward transfer from two-dimensional patterning to direct three-dimensional printing", Photonics West 2018, San Francisco, USA, LASE conference, session on "Laser 3D Manufacturing V", (30/01/2018).

Delrot P., Loterie D., Psaltis D., and Moser C., "Integrated Platform for Multi-resolution Additive Manufacturing," in *Industrializing Additive Manufacturing - Proceedings of Additive Manufacturing in Products and Applications - AMPA2017*, 2nd ed. (Springer International Publishing, 2017), Vol. 32, pp. 145–151.

Delrot P., Krizek J., Modestino M.A., Psaltis D., and Moser C. "Laser direct writing of viscous liquids by flow focusing ", Photonics West 2017, San Francisco, USA, LASE conference, session on "Laser 3D Manufacturing IV", (30/01/2017).

Delrot P. and Moser C. "Single- and Two-Photon Micro-Additive Manufacturing through Multimode Optical Fibers" at WE-Heraeus-Seminar on Merging Micro- and Nano-Optics: 3D Printing for Advanced and Functional Optics, Bad Honnef, Germany, (10/01/2017)

Delrot P., Psaltis D. and Moser C. "Integrated platform for multi-process precision 3D Printing", Strategic Focus Area - Advanced Manufacturing, 1st workshop: Information Exchange and Consortia Building Dübendorf, Switzerland, (17/10/2016).

Delrot P., Modestino M.A., Psaltis D., and Moser C. "Laser-assisted inkjet printing of highly viscous fluids with sub-nozzle resolution", Photonics West 2016, San Francisco, USA, LASE conference, session on "Laser Manufacturing III", (15/02/2016).

Extracurricular activities

Part time consulting in Junior Enterprise Opto-Services

2011-2012

Palaiseau, France

Writing a scientific report for the French Astronomy non-profit organisation on glare in mesopic vision and the standards to implement for urban lighting and for astronomical amateur observatory.

Manager at the EPFL Photonics Chapter

2015-2017

Lausanne, Switzerland

Organizing Science outreach events for kids and youngsters (labtours, small experiments to show light properties...).